Max-Planck-Institut für Plasmaphysik
Garching

'Current Holes' and other Structures in Motional Stark Effect Measurements

Dissertation
von
Doris Merkl

Technische Universität München

Technische Universität München
Fakultät für Physik
Max-Planck-Institut für Plasmaphysik (IPP)

'Current Holes' and other Structures in Motional Stark Effect Measurements

Doris Merkl

Vollständiger Abdruck der von der Fakultät für Physik
der Technischen Universität München
zur Erlangung des akademischen Grades eines
Doktors der Naturwissenschaften (Dr.rer.nat.)
genehmigten Dissertation.

Vorsitzender: Univ.-Prof. Dr. A. J. Buras

Prüfer der Dissertation: 1. Hon.-Prof. Dr. R. Wilhelm

2. Univ.-Prof. Dr. P. Böni

Die Dissertation wurde am 09.03.2004 bei der
Technischen Universität München eingereicht und
durch die Fakultät für Physik am 07.05.2004 angenommen.

Abstract

In a Tokamak fusion plasma, the induced plasma current and the external magnetic field coils create an appropriate magnetic field structure for confinement and stability of the plasma. The Motional Stark Effect diagnostic (MSE) is the main tool for the determination of the toroidal current density and the magnetic field configuration inside a Tokamak fusion plasma.
Within this work, the MSE data acquisition in ASDEX Upgrade was improved towards a real-time diagnostic. This real-time MSE diagnostic shall be used for the current profile, j, control during the experiment.
During the analysis of structures in the MSE measurements, a central region in the plasma without current density and without confining poloidal magnetic field was found, a so-called 'current hole'. In 'current hole' scenarios, a strong non-inductive current off-axis (e.g. bootstrap current) forms/maintains the 'current hole'.
The optimization of the bootstrap current is part of the 'advanced tokamak' studies since the bootstrap current is one candidate to replace at least partially the toroidal current produced with the transformer.
There are considerations in the international research community to develop the 'current hole' scenarios with the strong non-inductive current further towards a steady state scenario with reduced inductive current. The study of 'current holes' is also an important issue for predicting current profile evolution in next step fusion facilities like ITER, with high current diffusion time in scenarios with strong non-inductive current.
In the present work, the equilibrium reconstruction of 'current holes' are presented along with results of the current diffusion analysis.

Contents

Chapter 1

Introduction

1.1 Fusion

The energy reserves of fossil fuels like oil, natural gas and coal will be exhausted in the near future (oil in approx. 40 years, coal in 250 years [1]). Furthermore, the greatest resources of oil and gas are partly in political instable regions. Europe is mostly dependent on imports of these fossil fuels. Their future usage for energy production will further increase the CO_2-concentration in the atmosphere. A resulting global warming and drastic change in the climate could be the result. Due to these problems and the constantly increasing world wide energy demand, new energy sources will be required. Alternative energy like photovoltaic, wind and water energy depend on weather conditions and is therefore not constantly available. During the search for long lasting energy sources, one candidate is to imitate the energy production process of the sun. The fusion of light atomic nuclei on earth for energy production is known as controlled thermonuclear fusion. In a fusion reaction, two nuclei must first overcome their mutual electrostatic repulsion by approaching each other sufficiently close so that they can fuse. This is possible through the tunnel-effect. Fusion occurs at sufficiently high temperatures of at least some keV [1]. At such temperatures, a gas of light elements is completely ionized, since the ionization potential of hydrogen is 13.6 eV, for helium 24.5 eV and 54.4 eV. The positive electrostatic charge

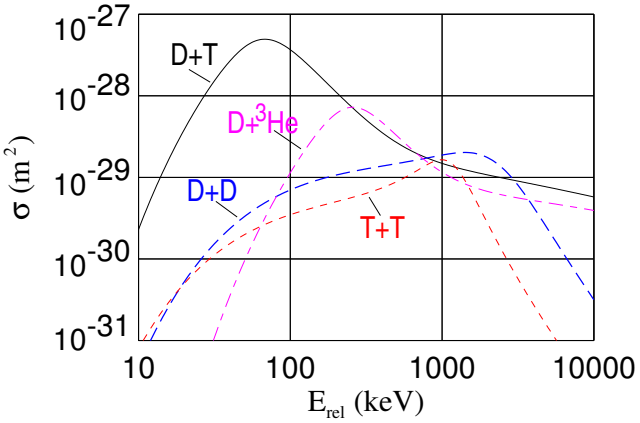

Figure 1.1: Cross section of reaction against thermal energy

[1] In plasma physics, temperatures will usually be given in energy units. The conversion is $1eV \hat{=} 11600K$ with $E_{therm} = k_B T = \frac{1}{2} m v_w^2$.

of the nuclei is balanced by the presence of an equal number of electrons. The ionized gas remains neutral above a mesoscopic length scale, the so-called Debye length, and is called a plasma which is an interesting and diversified subject for fundamental research.

The reaction of deuterium and tritium nuclei (D - T reaction) is the most favorable reaction due to the highest cross section at relatively low temperatures as seen in Fig. 1.1 and a high energy release per unit mass:

$$D + T \rightarrow {}^4He(3.5MeV) + n(14.1MeV) \tag{1.1}$$

One kilogram of this fuel would release about 10^8 kWh of energy, corresponding to tons of coal. Deuterium occurs naturally in heavy water and has a relative abundance of $n_D/n_H \approx 1.5 \cdot 10^{-4}$. The amount of deuterium in the world's oceans is estimated to suffice for the world's energy requirements at current consumption rates for in excess of 10^{10} years. Tritium does not occur naturally, but in principle the neutrons released in the reaction, shown in equation 1.1, can breed tritium from lithium. The reserves of lithium are estimated to last for $1 \cdot 10^4$ years.

The confinement of the plasma in a star is excellent due to the high gravitational force and the interstellar vacuum. On earth, one possibility is to confine the plasma contact-free with magnetic fields to obtain controlled fusion with high reaction rates and good confinement for energy production. The reaction rate R_{DT} for D - T is defined as [2]:

$$R_{DT} = n_D n_T \langle \sigma v \rangle \tag{1.2}$$

and gives the amount of fusion processes per unit volume and time where v is the relative velocity $v = v_D - v_T$, $n_{D,T}$ the particle density and the cross section σ. The thermonuclear power per unit volume for the D - T system is:

$$P_{therm} = \frac{n^2}{4} \langle \sigma v \rangle E \tag{1.3}$$

with $n = n_D + n_T$, $n_D = n_T$ and E is the energy released per reaction per unit volume. (Every power term, used in the following context, is defined as power density, i.e. power per unit volume.) From the total energy gained per fusion process of reaction (1.1) $E_{DT} = 17.6MeV$, four fifths are carried out of the plasma by the neutrons ($P_n = \frac{4}{5} P_{therm.}$), which are assumed to thermalize in the surrounding lithium blanket to extract the energy in a future reactor. The remaining one fifth is carried by the electrically charged alpha particle, confined by the magnetic field, which directly heats the plasma. The goal is ignition, this means obtaining a plasma which is maintained only with α-particle heating ($P_\alpha = \frac{1}{5} P_{therm.}$) without additional external heating. The efficiency of α-particle heating will be shown in the next generation of experiments, ITER[2]

[2]ITER is an international project of Europe, Japan, Russia, China, U.S.A., Korea.

(International Thermonuclear Experimental Reactor). ITER has a larger volume than present experiments which will improve the energy confinement further.
The ignition criterion is described by the following power balance inequality, assuming constant plasma profiles for simplicity,

$$P_{heating} \;=\; P_{\alpha} \;+\; P_{aux} \;>\; P_{loss} \tag{1.4}$$

The total power leaving the plasma is

$$P_{exit} = \underbrace{\frac{n^2}{5}\langle\sigma v\rangle E}_{P_n} \;+\; \underbrace{\underbrace{c_{Br} n^2 T^{\frac{1}{2}}}_{\approx P_{radiation}} \;+\; \underbrace{\frac{3nT}{\tau_E}}_{P_{diff}}}_{P_{loss}} \tag{1.5}$$

where P_{α} is the power of the α-particle heating, P_{aux} is the external heating power, $P_{radiation}$ is the radiation loss mainly through Bremsstrahlung (c_{Br} is the Bremsstrahlung constant) and P_{diff} is the diffusive energy loss through heat conduction and particle convection expressed in the form of the ratio of the plasma energy density [3] and the energy confinement time τ_E. Assuming that the generated power has a certain conversion efficiency and a fraction of this converted power is used for heating, then the available heating power can be expressed with a combined efficiency, η as:

$$P_{heating} = \frac{n^2}{20}\langle\sigma v\rangle E + \eta P_{exit} \tag{1.6}$$

The ignition or so-called Lawson criterion [3] can be rewritten as a function of T using equations 1.3-1.6:

$$n\tau_E \quad > \quad \frac{3T}{c(\eta)\langle\sigma v\rangle E \;-\; c_{Br} n^2 T^{\frac{1}{2}}} \tag{1.7}$$

with $c(\eta) = \frac{\eta+\frac{1}{4}}{5(1-\eta)}$. The energy confinement time can be computed in experiments with the assumption of $P_{loss} = P_{heating}$:

$$\tau_E = \underbrace{3nT}_{plasma\ energy} \quad / P_{heating} \tag{1.8}$$

The so-called triple product $nT\tau_E$ can be computed by measuring the plasma parameters density n, temperature T and the energy confinement time τ_E. Fig. 1.2 shows the ignition criterion for constant temperatures together with the reached values of the triple product in different fusion experiments. With respect to the triple product, the highest performance plasmas of present day experiments are about a factor of 5 below ignition. The so-called breakeven means the power gained by the fusion processes is equal to the power used to run the experiment. The planned experimental reactor ITER

[3] for pure hydrogen plasma with effective ion charge $Z_{eff} = 1 \rightarrow$ electron density $n_e = n = n_D + n_T$

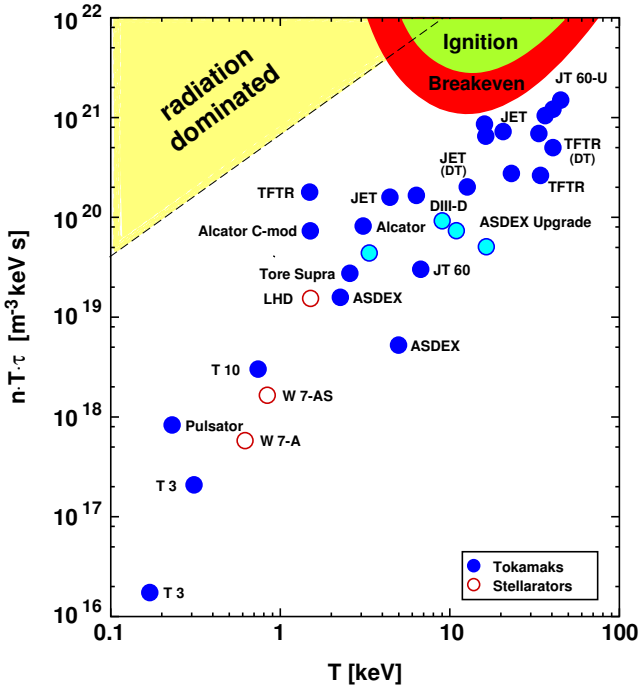

Figure 1.2: Ignition criterion and reached values of different experiments.

is designed to exceed the breakeven .

Since the plasma temperatures required for thermonuclear fusion exceed the melting point of any material by far, the hot plasma in fusion devices on earth needs to be isolated from the surrounding material structures by a magnetic field. Ionized particles gyrate around a magnetic field line while traveling in the direction of the field line in a strong magnetic field. The plasma can be confined by closing the magnetic field lines around a toroidal volume. However, particles drift out of a simple torus with magnetic field lines which are circular and toroidally closed. The toroidal field B_t varies as $1/R$ (R is the major radius, measured from the center of the torus). The gyrating particles have different gyro radii ($r_{gyr} = mv_\perp/qB$, where m is the particle mass, $v_\perp$ is the velocity perpendicular to the magnetic field, q is the charge of the particle and B the magnetic field magnitude) at opposite halves of their orbits. This results in a drift of the particles, where the electrons and ions drift to the top and bottom of the torus, respectively, the so-called ∇B drift. This produces an electrostatic field $\boldsymbol{E}$ which causes both species to drift outwards in the $\boldsymbol{E} \times \boldsymbol{B}$ direction. To avoid these losses, the magnetic field lines have to be helical. Now particles drift back into the torus. There are two different concepts to reach this helical magnetic configuration: the tokamak and the stellarator. In the stellarator, the helical field lines are created with complex 3 dimensional shaped coils. In the Tokamak an additional poloidal magnetic field is produced with a plasma current.

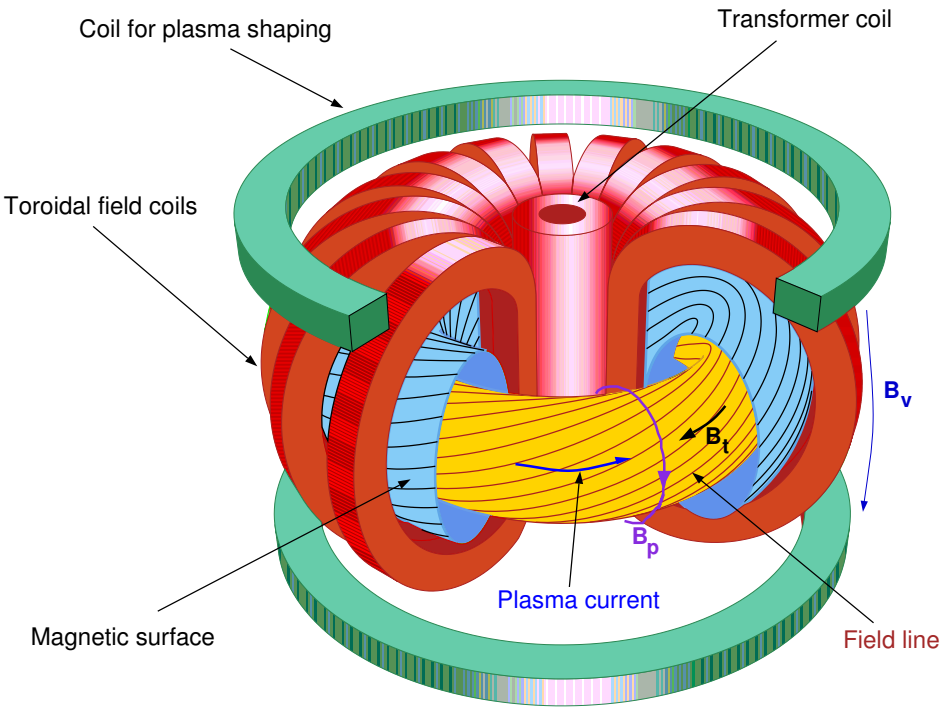

Figure 1.3: Scheme of a Tokamak

1.2 Tokamak

The tokamak [2] was proposed in the 1950s in Russia by A.Sacharov and was studied and further developed by L.A. Artsimowitsch. The tokamak configuration is shown in Fig. 1.3. The main magnetic field component B_t is in the toroidal direction, produced by external toroidal field coils. A poloidal field component B_p is mainly generated by a transformer induced toroidal current in the plasma. The induced current also produces the plasma in the startup phase with ohmic heating. The resulting field lines in the tokamak configuration are helical and lie on closed, nested magnetic field surfaces with constant magnetic flux in the form of tori. The pressure and poloidal current are assumed to be constant on these magnetic surfaces. Additional coils are used to elongate the plasma, giving a more triangular shape or changing the position of the plasma. The efficiency of confinement is represented by β, which is the ratio of plasma pressure and magnetic field pressure $B^2/2\mu_0$. For the economical viability of the fusion device, the β-value has to be maximized, since the costs for high magnetic field coils are large, especially for superconductive coils. However β is also subject to stability limitation, since gradients of the confined plasma pressure can drive instabilities.

The pitch of the magnetic field lines on each magnetic surface is characterized by the safety factor q which is very important for the stability of the plasma. In cylindric

geometry the safety factor as a function of the minor radius r has the simple form:

$$q_{cylind}(r) = \frac{r}{R}\frac{B_t}{B_p} = \frac{m}{n}. \tag{1.9}$$

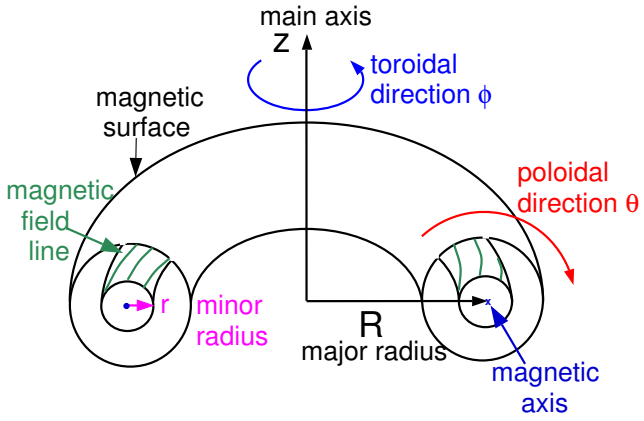

Figure 1.4: Toroidal geometry of a Tokamak

The safety factor can also be described by the ratio of the toroidal circulations m and the poloidal circulations n[4] of the magnetic field line. As an example, a magnetic field line on a $q = 2/1$ surface closes after two toroidal and one poloidal circulations. Plasma perturbations on rational q surfaces can grow more easily because they close resonantly after a few toroidal transits [5]. The stability and confinement of the plasma is limited by these Magnetohydrodynamic (MHD) instabilities.

The induced plasma current in a tokamak creates an appropriate magnetic field structure for confinement and heats the plasma. Additional heating methods like high frequency wave and neutral particle injection (NBI) are described in section 2.1. A detailed knowledge of the magnetic configuration and the related current density distribution are important for the theoretical understanding and the practical improvement of the stability and confinement.

The electrical conductivity $\sigma_\parallel$ of a fully ionized, uniform plasma along the magnetic field lines is, according to the theory of Spitzer and Härm (1953), described by

$$\sigma_\parallel = \frac{9.969 \cdot 10^3}{\ln \Lambda} T_e^{3/2} / Z_{eff}^2 \tag{1.10}$$

where Z_{eff} is the effective ion charge. The so-called Coulomb logarithm $\ln \Lambda$ is calculated from $\Lambda = 1.09 \cdot 10^{14} \frac{T_e}{Z_{eff}\sqrt{n_e}}$ where T_e is the electron temperature and n_e is the electron density. The current distribution is:

$$j_t(r) = \sigma_\parallel U_{loop} / 2\pi R. \tag{1.11}$$

The loop voltage U_{loop} can be measured at the edge of the plasma, thus the edge of the current distribution can be determined with this formula. If the magnetic configuration over the whole plasma is known, the current distribution can be computed by Ampère's

[4] m is the poloidal and n is the toroidal mode number

[5] The safety factor q is used to label these instabilities.

law. The magnetic configuration can be determined by measuring the magnetic pitch angle

$$\gamma_p = \tan^{-1}(\frac{B_p}{B_t}) \tag{1.12}$$

with the Motional Stark Effect (MSE) diagnostic. This diagnostic is the main tool in a tokamak to determine the internal magnetic configuration and the current density of the plasma with equilibrium reconstruction. It will be described in chapter 3 and is the basis of this thesis.
The toroidal magnetic field is determined by the field coils and scales with $1/R$ from the torus center. Therefore the side between the torus axis and the magnetic axis (Fig. 1.4) is called High Field Side (HFS), the side beyond the magnetic axis is called Low Field Side (LFS).

An important effect of this inhomogeneity of the magnetic field is the trapping of charged particles. Since the field lines are twisted around a magnetic surface, the particles experience different magnetic field strength during their motion along the field lines. Particles with high $v_\perp$ and low $v_\parallel$ are reflected when reaching a critical value of the magnetic field ('mirror effect'). Using the energy conservation and the adiabatic invariant magnetic moment $\mu = mv_\perp^2/2B$ [2], the trapping condition is:

$$\frac{1}{2}mv_{\parallel,0}^2 < (B_{max} - B_{min})\mu. \tag{1.13}$$

(where B_{max} and B_{min} are the maximal and minimal magnetic field seen by the passing orbit, respectively) and can be written as:

$$\frac{v_{\parallel,0}^2}{v_{\perp,0}^2} < \frac{B_{max} - B_{min}}{B_{min}} \approx \frac{2r}{R-r} = \frac{2\epsilon}{1-\epsilon} \tag{1.14}$$

with $\epsilon = r/R$ is the inverse aspect ratio. Together with the particle drift the resulting orbits of the trapped particles are so-called 'banana orbits' in poloidal projection with a finite width (Fig. 1.5).

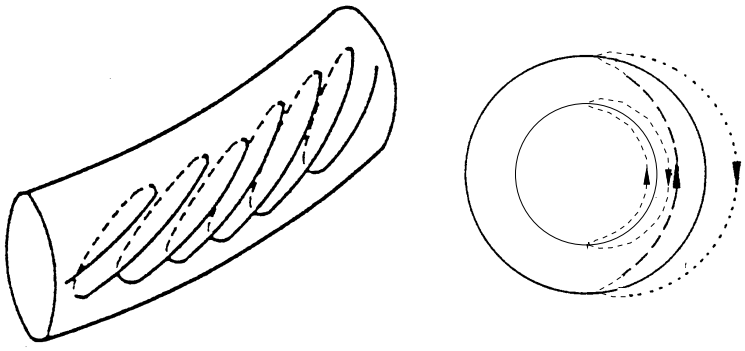

Figure 1.5: Orbit of a trapped particle (proton) and the poloidal projection of two different 'banana orbits'.

One important effect of these trapped particles is the production of an additional toroidal current due to a radial pressure gradient, the so-called bootstrap current $j_{BS} \propto \sqrt{\epsilon}\frac{\nabla p}{B_p}$. Particularly with a density gradient, a net current is produced since more trapped particles on their banana orbits at one radial position move in one direction than into the other direction (Fig. 1.5, right picture). Additionally a current of free electrons is produced by the friction between the trapped particles and the free electrons. The bootstrap current is one candidate to replace at least partially the toroidal current produced with the transformer. The optimization of the bootstrap current is part of the so-called 'advanced tokamak' studies.

The population of trapped particles is also important for plasma transport. Excursions of the guiding centers of the particles perpendicular to the magnetic surface due to scattering and drifts are related to the transport of energy and particles. Classical transport assumes that the transport is determined merely through particle collisions (Coulomb scattering) and the resulting excursions in the order of magnitude of their gyro radii. The trapped particles have a much larger radial excursion (as described before) and therefore an increased transport, known as neoclassical transport. However, the transport observed in experiments is higher than what the classical or neoclassical transport theory predicts.

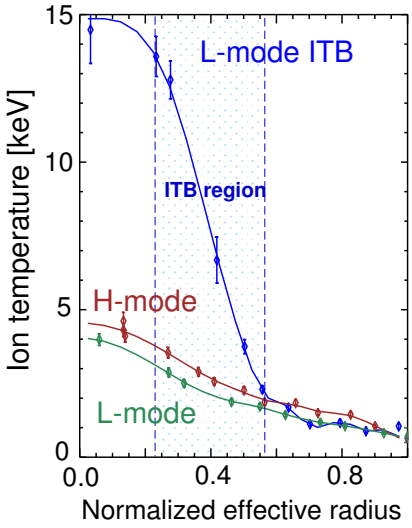

Figure 1.6: Comparison of the ion temperature in different confinement regimes

Additional anomalous transport is assumed to be caused by turbulent fluctuations (micro instabilities) in the plasma. One possible mechanism to suppress this turbulence and the related transport is to tear the turbulent eddies with shear flow. In cases with $\boldsymbol{E}\times\boldsymbol{B}$ flow shear radially different drift velocities of the plasma particles due to varying radial electric and magnetic fields occur. This flow shear is important for regimes with improved energy and particle confinement. One example is the change from the L-mode (**l**ow confinement) to the H-mode (**h**igh confinement) [4] with a higher confinement time. The H-mode has a transport barrier at the plasma edge, the formation of which can be explained with $\boldsymbol{E} \times \boldsymbol{B}$ flow shear [5]. Another experimental scenario with improved confinement and high temperature are so-called internal transport barriers (ITB) [6], [7], [8] which can also form due to sheared $\boldsymbol{E} \times \boldsymbol{B}$ flows (in L-mode plasmas, see Fig. 1.6). In an ITB regime, an inner region exists, where the radial transport is strongly reduced.

In some ITB scenarios, a so-called 'current hole' develops, an extended central region in the plasma with nearly zero current density. Although there is no confinement of the ions in this region, the global energy confinement is comparable with other advanced scenar-

ios (with high temperatures). These 'current hole' scenarios are quite stable. There are considerations in the international research community [9] to develop these 'current hole' scenarios further towards a steady state scenario with reduced inductive current. The study of 'current holes' is also an important issue for predicting current profile evolution in next step facilities like ITER with high current diffusion time and scenarios with strong non-inductive current. The analysis of a 'current hole' scenario in the ASDEX Upgrade tokamak is part of this thesis.

1.3 Goals and Outline of the Thesis

Within the scope of this thesis, different structures in Motional Stark Effect (MSE) measurements are examined which were discovered in some ITB plasmas. The structures, studied here, are related to MHD instabilities, changes in the magnetic flux surface topology and changes in the current density profile, so-called 'current holes', respectively. Also the improvements of the MSE diagnostic at the ASDEX Upgrade tokamak (see Appendix) towards a real-time diagnostic are a subject of this work.

Chapter 2 gives the background for the work presented here. First heating methods in a Tokamak like neutral beam injection (NBI) and electron cyclotron resonance will be described. The theory of the Motional Stark Effect, which is essential for this work, will also be introduced in this chapter 2. Following this, a description will be given how the magnetic field configuration can be measured with the Motional Stark Effect diagnostic. This is then followed by the basics of a equilibrium reconstruction including the measurements of the MSE diagnostic. An introduction of MHD instabilities will also be given, as their influence on MSE measurements will be discussed in chapter 3. Finally, a description of transport analysis, using the transport analysis code ASTRA, will be presented. The ASTRA code is used in chapter 4 for current diffusion simulations.

The MSE diagnostic at ASDEX Upgrade is described in detail in chapter 3. The improvements of the MSE data acquisition towards a real-time diagnostic are shown. The MSE real-time diagnostic shall be used for the current profile, j, control during the experiment. Using the new MSE system, the sensitivity of the MSE diagnostic to magnetic field perturbations will be discussed showing examples of structures in the MSE measurements and their possible explanation including the effect on the equilibrium reconstruction.

In chapter 4, the so-called 'current hole' , found through a very special structure in the MSE measurements, will be discussed in detail. This phenomenon of an experimental regime with hollow current density profiles in the center was already discovered in other tokamak experiments like JET (U.K.) and JT60-U (Japan) in ITB experiments with early heating during the current ramp-up phase. First an introduction into 'current holes' will be given. Then some experimental results of ASDEX Upgrade (AUG)

and MSE measurements in the 'current hole' scenario are shown. The equilibrium reconstruction of 'current holes' will be presented along with results of the current diffusion analysis with ASTRA. The bootstrap fraction, which is thought to be the reason for the formation of the 'current hole' in the neutral beam (NBI) heated 'current hole' scenario, was computed with ASTRA. Finally, a new experimental scenario with early ECCD (Electron Cyclotron Current Drive) instead of early NBI in the start-up phase, will be presented.

In the last chapter, the results will be summarized and discussed.

Chapter 2

Background

This chapter describes the background necessary for the following chapters. The two plasma heating systems, neutral beam injection (NBI) and electron cyclotron resonance heating (ECRH) will be described. The two heating systems are employed in the experiments at ASDEX Upgrade studied in this work. Also a short explanation of the Motional Stark Effect is given. This diagnostic is the main tool in ASDEX Upgrade to determine the internal magnetic configuration with equilibrium reconstruction. For the equilibrium reconstruction in ASDEX Upgrade, the codes CLISTE and NEMEC are used which will be described in this chapter. Also a short introduction to the ASTRA transport code [10] will be presented. This code is used in this thesis to model the current diffusion of 'current hole' experiments.

2.1 Heating

The initial heating in tokamaks comes from the ohmic heating caused by the induced toroidal current through a resistive plasma. At low temperature, ohmic heating is quite effective and produces temperatures of a few keV. However with increasing temperatures the resistivity decreases with $T_e^{-\frac{3}{2}}$ and additional heating is required. The additional main heating methods are the injection of energetic neutral beams and the resonant absorption of electromagnetic waves [2] at the electron or ion cyclotron resonance frequency (ECR/ICR).

2.1.1 Neutral Beam Heating

The injected particles of the heating beams have to be neutral because ions would be deflected by the magnetic field. First ions are produced and accelerated to the required energy by an electric field. Then they are neutralized by charge exchange in a gas target. The remaining ions are removed by using a magnetic field. The neutral particles become ionized through collisions with plasma particles and they are then confined by the magnetic field. Once ionized, the fast ions have orbits determined by their

energy, point of deposition and angle of injection. The resulting fast ions are slowed down by Coulomb collisions with electron and ions in the plasma and then become thermalized. The slowing down time, τ_s, of the fast ions due to collisions with electrons is $\tau_s = -\frac{v}{<dv/dt>} \propto \frac{T_e^{\frac{3}{2}}}{n_e}$. Energy and momentum are passed to the particles in the plasma, causing heating of electrons and ions. If the injection velocity of the neutral beam particles is much larger than the thermal ion velocity then the electron heating is initially dominant.
Particles of the neutral beam injection can be lost due to 'shine through', where neutral particles pass the plasma without being ionized and hit the inner wall. This occurs especially at low plasma density. A further loss mechanism is the orbit loss, where the fast ions hit the wall during their gyration and drift motion. Some of the fast ions can be neutralized due to charge exchange and leave the plasma without depositing their energy.

The directed flow of fast ions [11] from the neutral beam injection tends to drag the electrons with it. This tendency is opposed by the electron collisions with the background ions. In the classical transport theory (without trapping of particles), the collisional electron current cancels the ion current if $Z_b = Z_{eff}$. When trapped electron orbits (neoclassical transport) are included the electron current is reduced and a net current can be driven. The toroidal current density, j_{bd}, of circulating fast ions from the neutral beam injection is [11]

$$j_{bd} = n_b \langle v_\parallel \rangle e Z_b \{1 - Z_b/Z_{eff}[1 - G(Z_{eff}, \epsilon)]\} \tag{2.1}$$

where n_b is the beam density, $v_\parallel$ is the parallel velocity of the fast ions, Z_b is the charge of the fast ions, Z_{eff} the effective charge of the plasma, G is the trapped electron correction depending on Z_{eff} and the inverse aspect ration $\epsilon = r/R_0$. When $Z_b = 1$, like in hydrogen or deuterium beams, and $Z_{eff} > 1$ the current is mainly carried by the fast ions. In the case of $Z_b/Z_{eff} \approx 1 - 2$ the driven current is very low.

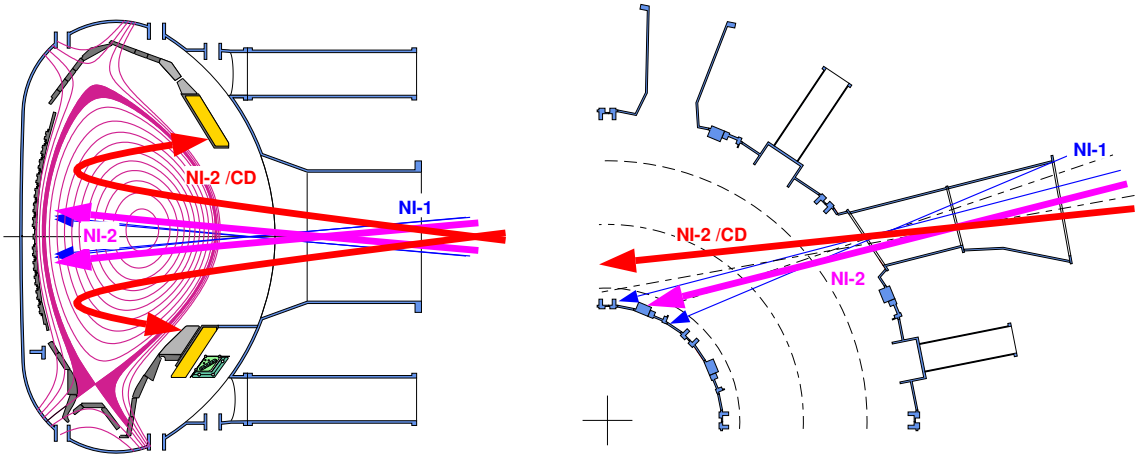

Figure 2.1: NBI geometry at ASDEX Upgrade. NI-1 refers to the beam box 1, NI-2 to box 2. CD labels the current drive sources in the new beam geometry since 2001.

The NBI in ASDEX Upgrade has a maximum power of $P_{NBI} = 20$MW. There are two beam boxes consisting of four ion sources each. Each ion source has a maximum injection power of 2.5MW. The beam line geometry can be seen in Fig. 2.1 and the classification is listed in following table before and after the change of the beam geometry of injector box 2 in the year 2000/2001:

Injector Box	Source	Classification ...-2000/2001-...
1	Q1	radial
1	Q2	tangential
1	Q3	tangential
1	Q4	radial
2	Q1 (Q5)	radial/tangential
2	Q2 (Q6)	tangential/off-axis tangential [current drive]
2	Q3 (Q7)	tangential/off-axis tangential [current drive]
2	Q4 (Q8)	radial/tangential

2.1.2 Electron Cyclotron Resonance Heating

The plasma can also be heated by resonant absorption of electromagnetic waves with frequencies of the electron or ion gyration frequencies $\omega_e = eB/m_e c$, $\omega_i = Z_i eB/m_i c$. The electron cyclotron (EC) power deposition is dependent of the magnetic field B, plasma electron density n_e, electron temperature T_e and the geometrical factors like the launching angles, launcher position and initial shape of the beam. Fulfilling the wave particle resonance condition for the X and O modes in hot plasma approximation

$$\omega - l\omega_e/\gamma = k_\parallel v_\parallel \tag{2.2}$$

electrons with the velocity v and a velocity component $v_\parallel$ parallel to B can absorb energy from the wave with the frequency ω and the wave number $k_\parallel$ parallel to B.

$\gamma = \sqrt{1 - \frac{v^2}{c^2}}$ is the relativistic factor, l is the EC wave harmonic number and ω_e is the non-relativistic electron cyclotron frequency.

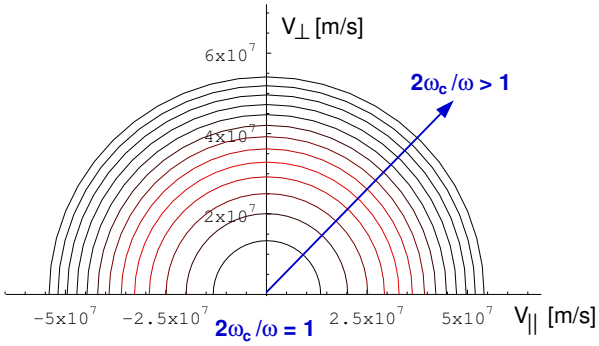

Figure 2.2: EC resonant curves in velocity space at perpendicular launching

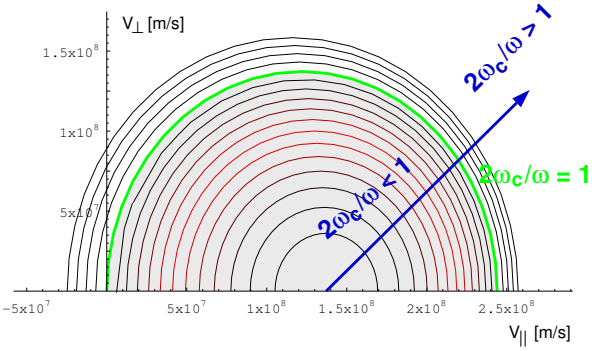

Figure 2.3: EC resonant curves in velocity space with oblique launching

The absorbed energy from the wave increases mainly the perpendicular energy component of the resonant electrons. Fig. 2.2, 2.3 shows the resonant curves which are solutions of 2.2 in the velocity space $(v_\perp, v_\parallel)$ with two examples of second harmonic X mode EC waves launched in low density plasma with $T_e \approx 5$keV from the low field side (LFS). In Fig. 2.2 the wave is launched perpendicular ($\rightarrow k_\parallel = 0$) and the resonant curves are circles, Fig. 2.3 shows the case for oblique launched EC wave where the resonant curves are elongated ellipses which are shifted in velocity space.
The electron cyclotron current drive [2], [12] relies on the generation of an asymmetric resistivity due to the selective heating of electrons moving in a particular toroidal direction. These preferentially heated electrons collide less often with the ions than those electrons circulating in the opposite toroidal direction. Therefore this net toroidal momentum results in a net electric current with the two species moving in opposite directions. With the Fokker-Planck equation, the distribution function of the electrons in the presence of applied ECCD can be described. The current drive efficiency is limited by different physical mechanisms like incomplete single-pass absorption which leads to counter-streaming currents on the opposite site of the resonance, transport losses or trapped particle effects.

Assuming a Gaussian beam profile, the power deposition density, $p_{ECRH}(\rho)$, and the current density profile, $j_{ECRH}(\rho)$, can be determined by the center of the deposition and the width of the deposition profile which can then be used as input for example in ASTRA.

TORBEAM

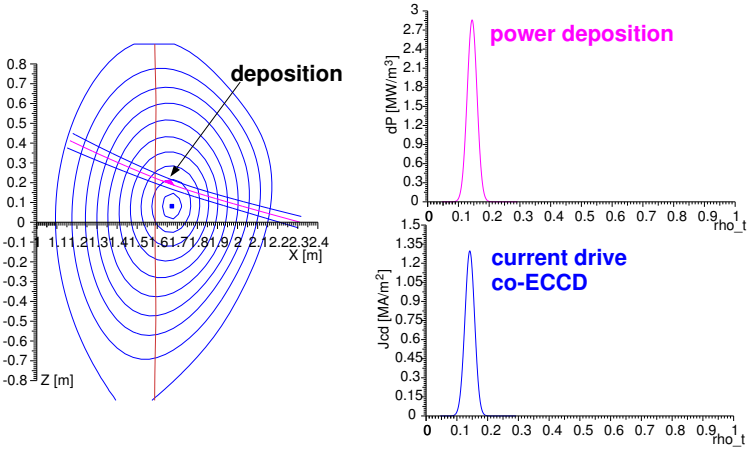

Figure 2.4: Poloidal cross section, the deposition of the co-ECCD off-axis, the power deposition and the current drive profile of 17811 at t=0.66s for 1 gyrotron.

The power deposition profile and the driven current density can be computed with the beam tracing code TORBEAM [13] which computes the propagation of the EC beam with Gaussian cross section in cold plasma approximation.
The code takes experimental data of a certain discharge like the equilibrium and kinetic profiles such electron density and electron temperature. The profiles of the power deposition and the driven current for one gyrotron in discharge #17811 with co-ECCD off-axis (at $\rho_{tor} \approx 0.15$), computed with TORBEAM, is shown in Fig. 2.4. The usually total driven current with four gyrotrons co-/counter is in the range $10 - 100$ kA.

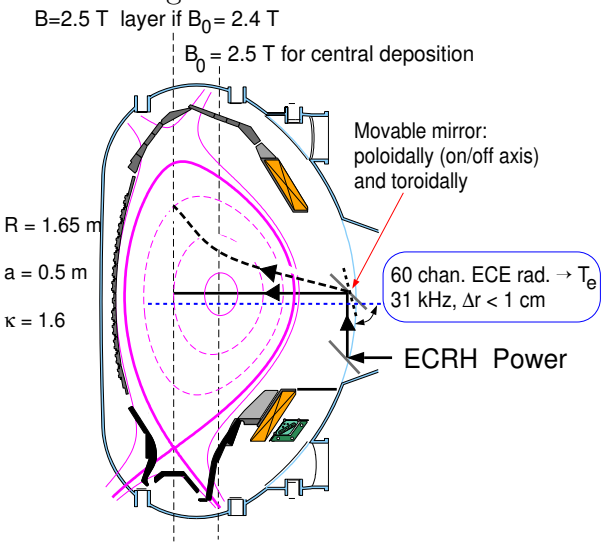

Figure 2.5: ECRH system at ASDEX Upgrade.

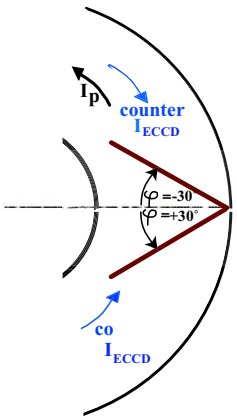

Figure 2.6: View from the top, showing the range of the toroidal angle φ for the launching beams.

The current ECRH system at ASDEX Upgrade consists of four gyrotron working at 140 GHz launched from the low field side (LFS). Each gyrotron delivers a power, P_{ECRH}, of 0.5MW for 2s, absorbed in the plasma 0.4MW from each gyrotron. A steerable mirror allows the focused beam to be launched in the desired poloidal and toroidal direction for pure heating or current drive. The focused ECRH beams have a very narrow power

deposition width of roughly 2-3 cm. This is less than 10% of the ASDEX Upgrade minor radius. The usual value of the magnetic field $|B_t| \approx 2.5$T corresponds to the second harmonic X mode of the EC (electron cyclotron) wave. The EC absorption can be displaced vertically along the resonance layer by changing the poloidal angle θ in the range of $\pm 32°$. The position of the resonance layer can be shifted radially by changing the magnetic field B_t. The EC beam can produce co-/counter ECCD (Electron Cyclotron Current Drive) by choosing the toroidal launching angle φ between $\pm 30°$.

2.2 Motional Stark Effect

Motional Stark Effect (MSE) polarimetry has become the most important method to measure the internal local poloidal field. From this measurement the current density profile in a tokamak can be determined. The theory of the Motional Stark Effect will be described here as preparation for chapter 3.

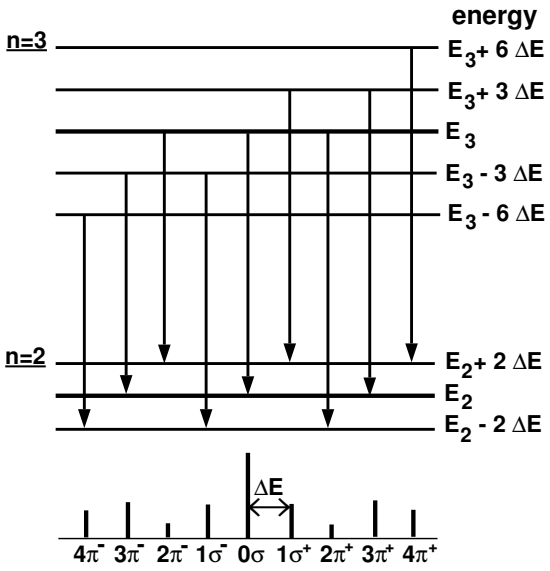

Figure 2.7: Energy term diagram for the linear Stark effect of the H_α-transition. The schematic spectrum, observed at 90° to the Lorentz field, shows the symmetry of the Stark lines.

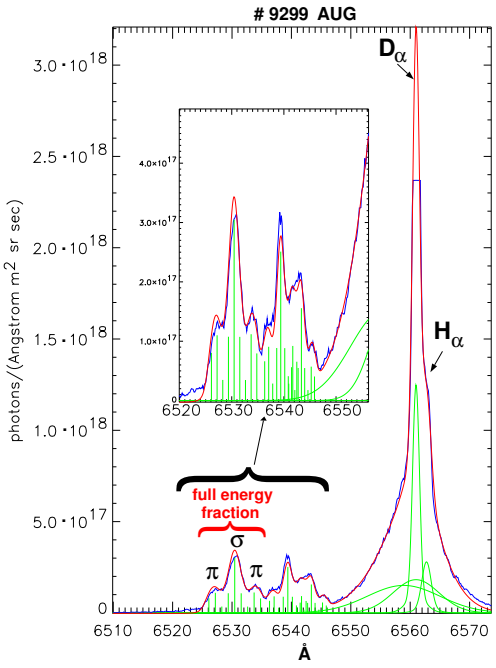

Figure 2.8: Spectrum of a AUG discharge in the neighborhood of the D_α line with one active beam, P= 2.5MW

Neutral beam injection (NBI) is mainly used as a heating source for tokamak plasmas. In addition, neutral beams can serve as diagnostic tools. One main application for beam emission spectroscopy is the determination of the internal magnetic field of a tokamak using the motional Stark effect ([14], [15], [16],[17],[18], [19], [20], [21], [22], [23]). The neutral beam particles (here deuterium D^0) are excited by collisions with

plasma ions, A^Z, and electrons, e^-, while penetrating the plasma. The beam emission is Doppler shifted if observed at an angle unequal 90° depending on the velocity of the beam particles and the viewing angle. This separates the beam emission from the edge and Charge Exchange (CX) emission in the spectrum. The three energy fractions of the neutral beam [1] corresponding to H^+, H_2^+, H_3^+ or D^+, D_2^+, D_3^+ are seen in the spectrum as three partly overlapping spectral lines. For the H_α/D_α transitions $n = 3 \rightarrow 2$ each part splits into 15 components due to the motional Stark effect, but only 9 have enough intensity [24] to be useful.

The neutral atoms moving with a constant velocity $\boldsymbol{v}_b$ in a magnetic field $\boldsymbol{B}$ experience a Lorentz electric field

$$\boldsymbol{E_L} = \boldsymbol{v}_b \times \boldsymbol{B} \tag{2.3}$$

in their own frame of reference induced by their motion. The total electric field

$$\boldsymbol{E} = \boldsymbol{v}_b \times \boldsymbol{B} + E_r \cdot \boldsymbol{e}_r \tag{2.4}$$

causes a splitting and a shift of atomic energy levels.

This effect is called motional Stark effect. The line spectrum of neutral hydrogen or its isotopes is dominated by the motional Stark effect, because hydrogen shows a strong linear Stark effect. The magnetic field, its magnitude and orientation can be determined by measuring both the line splitting and the polarization properties of the Balmer-α neutral beam emission ($H_\alpha, D_\alpha, T_\alpha, \lambda_0(H_\alpha) = 656.3$ nm transition n = 3 → 2). Fig. 2.7 shows the energy term diagram of the H_α transition with the splitting of the linear Stark effect. The schematic diagram below shows the different polarized Stark lines. The σ^+ and σ^- Stark lines are right and left hand circular polarized light respectively, which appears as linear polarized perpendicular to the electric field. The π-lines are absent in longitudinal and are at a maximum in transverse observation.

The MSE diagnostic at ASDEX Upgrade (AUG) uses a 60 keV D_α neutral beam injection (source 3 (Q3) of beam box 1) and measures the direction of polarization, the geometry-dependent polarization angle γ_m, to determine the magnetic pitch angle, the current density profile $j(r)$ and the safety factor profile $q(r)$ as descriped in chapter 3.

2.3 MagnetoHydroDynamic (MHD)

A simple useful mathematical model treating a magnetically confined plasma consists of magnetohydrodynamic (MHD) equations [25]. The plasma can be described as a conductive fluid (macroscopic electrically neutral fluid made up of charged particles) with the fluid variables mass density ρ, fluid velocity v and pressure p. Equations 2.5 - 2.7 determine the time evolution of mass, momentum and energy[2], respectively. The

[1] The positive ion source of the neutral beam produces not only atomic hydrogen/deuterium ions, but also molecular ions, $H_2^+, H_3^+/D_2^+, D_3^+$

[2] using the convective derivative $\frac{d}{dt} = \frac{\partial}{\partial t} + \boldsymbol{v}\boldsymbol{\nabla}$

adiabatic equation of state 2.7 is the energy equation assuming an adiabatic evolution characterized by a ratio of specific heats, γ. Equation 2.8, the Ohm's law, implies that the plasma is a perfect conductor[3] in the so-called 'ideal' MHD ($\eta = 0$). Equations 2.9 - 2.11 indicate that in ideal MHD the electromagnetic behavior is governed by the low-frequency Maxwell equations (neglecting the displacement current $\epsilon_0 \frac{\partial E}{\partial t}$):

$$\frac{\partial \rho}{\partial t} + \nabla(\rho \boldsymbol{v}) = 0 \qquad \text{(mass conservation)} \tag{2.5}$$

$$\rho \frac{\partial \boldsymbol{v}}{\partial t} + \rho(\boldsymbol{v} \cdot \nabla)\boldsymbol{v} + \nabla p - \boldsymbol{j} \times \boldsymbol{B} = 0 \qquad \text{(momentum equation)} \tag{2.6}$$

$$\frac{\partial p}{\partial t} + \boldsymbol{v} \cdot \nabla p + \gamma p \nabla \boldsymbol{v} = 0 \qquad \text{(adiabatic equation)} \tag{2.7}$$

$$\boldsymbol{E} + \boldsymbol{v} \times \boldsymbol{B}\ (-\eta \boldsymbol{j}) = 0 \qquad (\text{'ideal' (or resistive) Ohm's law}) \tag{2.8}$$

$$\frac{\partial \boldsymbol{B}}{\partial t} + \nabla \times \boldsymbol{E} = 0 \qquad \text{(Faraday's law)} \tag{2.9}$$

$$\mu_0 \boldsymbol{j} - \nabla \times \boldsymbol{B} = 0 \qquad \text{(Ampère's law)} \tag{2.10}$$

$$\nabla \boldsymbol{B} = 0 \qquad \text{(no magnetic charge)} \tag{2.11}$$

These equations can be solved to calculated a equilibrium and to investigate the stability of the equilibrium against perturbations [25].

2.4 Equilibrium Reconstruction

The tokamak equilibrium is generally assumed to be axisymmetric. The magnetic configuration is then independent of the toroidal coordinate ϕ (Fig.1.4). As described in the introduction, magnetic flux, pressure and poloidal current are constant on the magnetic flux surfaces [25],[2].

[3] implies that the electric field is zero in a reference frame moving with plasma.

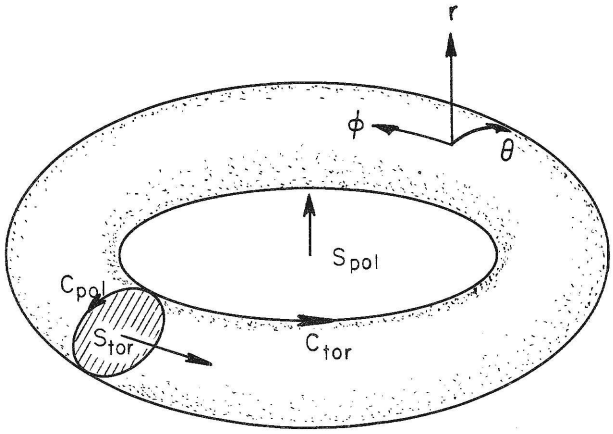

Figure 2.9: Toroidal flux surface showing cut surfaces and contours

On the torus two different topological curves, the poloidal and the toroidal circulating curves, exist. Thus the magnetic flux surfaces can be labeled either with the toroidal or poloidal fluxes. The toroidal flux is defined with any cross section of the toroid, S_{tor}:

$$\psi_{tor} = \Phi = \int_{S_{tor}} \boldsymbol{B} d\boldsymbol{S} \tag{2.12}$$

The poloidal flux is defined with any cut surface spanning the hole in the toroid, S_{pol}:

$$\psi_{pol} = \Psi = \int_{S_{pol}} \boldsymbol{B} d\boldsymbol{S} \tag{2.13}$$

Using the flux functions, a normalized poloidal flux radius, ρ_{pol}, can be defined:

$$\rho_{pol} = \sqrt{\frac{\Psi - \Psi_a}{\Psi_s - \Psi_a}} \tag{2.14}$$

where the index a refers to the magnetic axis and index s to the separatrix, the last closed flux surface. The normalized poloidal flux ρ_{pol} is zero at the magnetic axis and 1 at the separatrix. The same definition is given for the normalized toroidal flux radius ρ_{tor}

$$\rho_{tor} = \sqrt{\frac{\Phi - \Phi_a}{\Phi_s - \Phi_a}} \tag{2.15}$$

which is also defined as zero at the magnetic axis and 1 at the separatrix. However, as the toroidal flux is defined only inside the separatrix, ρ_{tor} is also defined only inside the separatrix. The force balance equation, derived from the Euler equations for fluid motion coupled with Maxwell's equations for the evolution of magnetic fields with the assumption of a slowly evolving plasma ($d\boldsymbol{v}/dt \equiv 0$), see equation 2.6, is:

$$\boldsymbol{j} \times \boldsymbol{B} = \boldsymbol{\nabla} p \tag{2.16}$$

With the only dependence of p on Ψ, the force balance equation can be written as:

$$\frac{\partial p}{\partial R} = \frac{dp}{d\Psi}\frac{\partial \Psi}{\partial R} = j_\Phi B_z - j_z B_\Phi \tag{2.17}$$

With Ampère's law (equat. 2.10), the components of $\boldsymbol{j}$ can be written as:

$$j_\Phi = \frac{1}{\mu_0}(\frac{\partial B_R}{\partial z} - \frac{\partial B_z}{\partial R}) \tag{2.18}$$

$$j_z = \frac{1}{\mu_0 R}\frac{\partial}{\partial R}(RB_\Phi) \tag{2.19}$$

$$\tag{2.20}$$

The components of the magnetic field can be related for example with the poloidal flux in the $(R,\ \Phi)$-plane:

$$\Psi(R) = 2\pi \int_0^R dR' R' B_z(R') \tag{2.21}$$

After integration, the components of the magnetic field are:

$$B_R = -\frac{1}{2\pi R}\frac{\partial \Psi}{\partial z} \tag{2.22}$$

$$B_z = \frac{1}{2\pi R}\frac{\partial \Psi}{\partial R} \tag{2.23}$$

$$\tag{2.24}$$

Then all vector components of equation 2.17 can be expressed with the poloidal flux Ψ, replacing RB_Φ with a current flux function $f(\Psi) = RB_\Phi/\mu_0$ $(= \mu_0 I_{pol}/2\pi)$. The resulting equation is then:

$$\begin{aligned} R\frac{\partial}{\partial R}(\frac{1}{R}\frac{\partial \Psi}{\partial R}) + \frac{\partial^2 \Psi}{\partial z^2} &= -\mu_0 R^2 p'(\Psi) - {\mu_0}^2 f(\Psi) f'(\Psi) \\ &= -\mu_0 R j_\Phi \end{aligned}$$

This equation is called **Grad-Shafranov** equation [26], [27]. It describes the toroidally axisymmetric equilibrium. The Grad-Shafranov equation is not linear in Ψ, since p and f depend on Ψ, and can only be solved numerically. It is determined by the choices of $p(\Psi)$, $f(\Psi)$ and the boundary conditions or externally imposed constraints on Ψ. After the determination of the poloidal and toroidal magnetic flux, the safety factor q can be calculated:

$$q = \frac{\nabla \Phi}{\nabla \Psi} \tag{2.25}$$

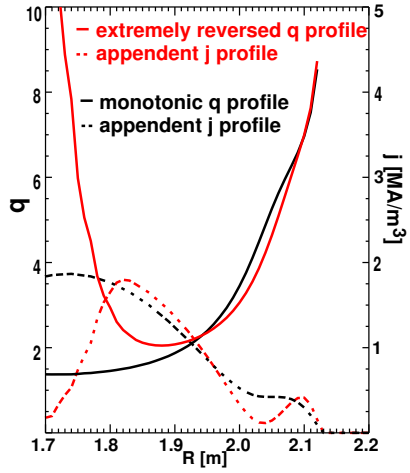

Figure 2.10: Monotonic (black) and reversed (red) q profile from equilibrium reconstruction and the appendent j profiles.

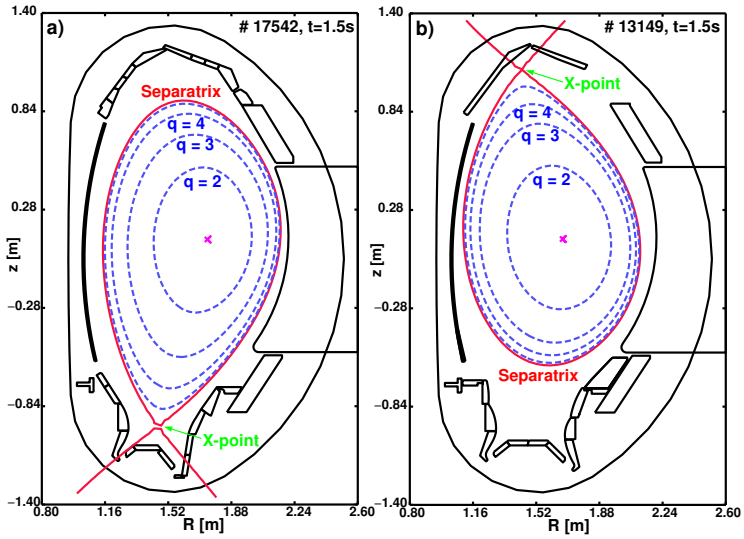

Figure 2.11: Poloidal cross section of lower single null a) and upper single null b) discharge.

Fig. 2.10 shows the difference between a reversed [4] q profile (red) with the hollow current density profile j (red) and a monotonic q profile (black) with the peaked current density profile j (black) from the equilibrium reconstruction. In Fig. 2.11 the poloidal cross section of a typical equilibrium reconstruction is shown with a lower single null configuration (X-point is below) in a) and a upper single null configuration (X-point is above) in b) , where the flux surfaces are labeled with the q values.

2.4.1 CLISTE

CLISTE [28] is an acronym for **C**omp**L**ete **I**nterpretive **S**uite for **T**okamak **E**quilibria. The CLISTE code finds a numerical solution of the Grad-Shafranov equation for a given set of poloidal field coil currents and limiter structures by varying the free parameters in the parameterization of p' and ff' profiles. They define the toroidal current density profile j_Φ to obtain a best fit to a set of experimental measurements. These measurements can include for example external magnetic data, MSE data, kinetic pressure profile and q profile information from SXR measurements. The free parameters are varied so that the penalty or cost function is minimized (i.e. the differences between the set of experimental measurements and those predicted by the equilibrium solution are minimized). Only measurements which are linear in the free parameters, contribute to the cost function. During each iteration, a linear optimization of the free parameters in $p'(\Psi)$ and $ff'(\Psi)$

[4] with hollow current density profile

profiles is done with a given parameterization of the source profiles as:

$$p'(\Psi) = \sum_{i=1}^{m_p} c_i \pi_i(\Psi) \tag{2.26}$$

$$ff'(\Psi) = \sum_{j=1}^{m_{ff}} d_j \varphi_j(\Psi) \tag{2.27}$$

$c_i,\ d_j$ are the free parameters, $\pi_i(\Psi)$ and $\varphi_j(\Psi)$ are the basis functions of the plasma current distribution, where Ψ is the full equilibrium flux function from the previous iteration cycle. Corresponding poloidal flux basis functions $\Psi_{p,i}^{new}$ and $\Psi_{ff,i}^{new}$ are generated with which the updated equilibrium flux function is generated:

$$-(\frac{\partial^2 \Psi_{p,i}^{new}}{\partial R^2} - \frac{1}{R}\frac{\partial \Psi_{p,i}^{new}}{\partial R} + \frac{\partial^2 \Psi_{p,i}^{new}}{\partial z^2}) = \mu_0 R^2 \pi_i(\Psi) \tag{2.28}$$

$$-(\frac{\partial^2 \Psi_{ff,j}^{new}}{\partial R^2} - \frac{1}{R}\frac{\partial \Psi_{ff,j}^{new}}{\partial R} + \frac{\partial^2 \Psi_{ff,j}^{new}}{\partial z^2}) = \varphi_j(\Psi) \tag{2.29}$$

The updated full equilibrium flux, with the yet undetermined coefficients $\{c_i\}$ and $\{d_j\}$, is given as [5]:

$$\Psi^{new} = \sum_{i=1}^{m_p} c_i \Psi_{p,i}^{new} + \sum_{j=1}^{m_{ff}} d_j \Psi_{ff,j}^{new} + \Psi^{ext} \tag{2.30}$$

The solution grids for $\Psi_{p,i}^{new}$ and $\Psi_{ff,i}^{new}$ are passed to a routine which calculates the predicted measurements from the flux function. In this way a matrix of $m_p + m_{ff}$ columns of 'basis values' $b_{n,k}((n = 1, ..., N_m)(k = 1, ..., m_p + m_{ff}))$ for each of N_m measurements is produced. If $\mathbf{B}$ is the data matrix and $\mathbf{y}$ is the vector of measurements then the optimization problem reduces to solve the linear regression:

$$\mathbf{y} = \mathbf{B} \cdot \boldsymbol{\alpha} \tag{2.31}$$

where $\boldsymbol{\alpha}$ is the solution vector of the optimized free parameters for the present iteration. The linear parameterization of the current profile has been implemented in form of a cubic spline representation with a flux label ($\propto \rho_{pol}$). The number and positions of knots are user-selectable, but fixed during the optimization.

For analyzing 'current hole' equilibria, see chapter 4, an improved version of CLISTE (modified by P. J. McCarthy) with stabilizing features was used. For very low central current density, ρ_{pol} is a flat function of spatial radius r (i.e. the mapping is ambiguous). This leads to convergence difficulties in CLISTE. An alternative coordinate ρ_{mid} (instead of ρ_{pol}) for the source profiles p' and ff' can be chosen in the improved version of CLISTE:

$$\rho_{mid} = \frac{\text{flux surface diameter in magnetic midplane}}{\text{plasma diameter in magnetic midplane}} \tag{2.32}$$

[5] The full equilibrium flux also includes the contribution from the external measured currents, Ψ^{ext}.

Also using an 'over-relaxation' method in the improved version, stabilizes the convergence. With an user-specified weight w, the latest solution for $\Psi(R,z)$ is replaced by a weighted sum of the latest and previous solutions:

$$\Psi[i+1] = w\Psi[i] + (1-w)\Psi[i+1] \tag{2.33}$$

and similarly for the current density:

$$j[i+1] = wj[i] + (1-w)j[i+1] \tag{2.34}$$

2.4.2 NEMEC

The new version of VMEC/NEMEC [29] is a 3-dimensional energy-minimizing fixed-/free-boundary[6] stellarator code which was modified for tokamak equilibria (by S. P. Hirshman). The code is able to handle equilibria without toroidal current like in cases with a 'current hole' [7]. The plasma energy (magnetic plus thermal), W_p, is minimized with conservation of the flux over a toroidal area, V_p:

$$W_p = \int_{V_P} (\frac{B^2}{2\mu_0} + p)dV \tag{2.35}$$

where B is the magnetic field and p is the plasma pressure. The code uses a flux coordinate system (s,θ,ζ) where s is the normalized toroidal flux, θ and ζ are the (angle-like) poloidal and toroidal coordinates. The code assumes nested flux surfaces (ideal MHD) and uses a Fourier expansion (representation) of the cylindric coordinates (R,ϕ,z), see [29]. The goal is to compute the Fourier amplitudes of R and z by solving the appropriate components of the force balance equation (2.16)

$$F \equiv \boldsymbol{j} \times \boldsymbol{B} - \boldsymbol{\nabla} p = (\boldsymbol{\nabla} \times \boldsymbol{B}) \times \boldsymbol{B} - \boldsymbol{\nabla} p = 0 \tag{2.36}$$

in each iteration using a spectral Green's function method [29]. If appropriate error criteria are not satisfied, the loop is repeated.

The VMEC/NEMEC codes uses the rotational transform $\iota = 1/q$ instead of the safety factor q. In analyzing 'current holes' this is beneficial as the central q becomes infinite. The VMEC code computes a fixed-boundary equilibrium by minimizing the total energy, W_p, when the plasma boundary (from e.g. CLISTE), the total toroidal flux (from e.g. CLISTE), the pressure profile, the rotational transform or the toroidal current density is given. A cubic spline interpolation for these profiles is used to compute the needed values from a given set of discrete values.

[6] For free boundary equilibrium: The vacuum magnetic field is decomposed as $B_v = B_0 + \nabla\Phi$ where B_0 is a field determined from plasma currents and external coils and Φ is a single valued potential necessary to satisfy the Neumann condition $B_v \cdot d\Sigma_p = 0$ when $p \neq 0$ (Σ_p is the plasma surface)

[7] and arbitrary toroidal geometry

An example of a 'current hole' equilibrium was computed with NEMEC using the MSE data as additional constraint [30]. The experimental pressure profile and a flux surface inside, but close to the separatrix of a CLISTE equilibrium can be used as input. The vacuum magnetic field produced by the external coils is computed using the currents of the toroidal and poloidal field coils. With the vacuum field, the plasma boundary, the pressure profile, the iota profile (starting with CLISTE q profile) and the total toroidal flux as input to NEMEC code, the free-boundary equilibrium can be determined. Then the corresponding magnetic field and the polarization angles from the magnetic field components at the positions of the MSE diagnostic can be calculated. The computed polarization angles, the position of the magnetic axis and the total plasma current I_p are compared with the experimental data. If necessary the poloidal coil currents, the pressure profile and especially the iota profile are slightly changed inside the error margins by hand and the next iteration can start until the equilibrium results and the experimental measurements are in agreement.

2.5 MHD Instabilities

A possible method for analyzing the stability of a system is the energy principle. The idea of the energy principle is that the equilibrium of the system is unstable if a perturbation lowers the potential energy of the equilibrium. Using the ideal MHD equations and a linear approximation, the force produced by a magnetic field perturbation with a displacement $\boldsymbol{\xi}$ can be described as:

$$\boldsymbol{F}(\boldsymbol{\xi}) = \rho\frac{\partial^2\boldsymbol{\xi}}{\partial t^2} = \boldsymbol{j_1}\times\boldsymbol{B_0} + \boldsymbol{j_0}\times\boldsymbol{B_1} - \boldsymbol{\nabla}p_1 \tag{2.37}$$

where the indices 0, 1 describe the equilibrium and the perturbed quantities respectively. The resulting energy change of the plasma is given by:

$$\delta W = -\frac{1}{2}\int \boldsymbol{\xi}\boldsymbol{F}d\boldsymbol{r} \tag{2.38}$$

The sign of δW decides on the stability of the system. The plasma is unstable if $\delta W < 0$ and stable if $\delta W > 0$ for physically allowed displacement $\boldsymbol{\xi}$. The equation 2.38 can be separated in the vacuum and the plasma energy parts:

$$\delta W = \delta W_{vac} + \delta W_{plasma} \tag{2.39}$$

$$\delta W_{vac} = \frac{1}{2}\int \frac{B_1^2}{\mu_0}dV \tag{2.40}$$

$$\delta W_{plasma} = \frac{1}{2}\int \left[\frac{B_1^2}{\mu_0} - \underline{\boldsymbol{\xi}(\boldsymbol{j_0}\times\boldsymbol{B_1})} + \gamma p_0(\boldsymbol{\nabla}\boldsymbol{\xi})^2 + \underline{(\boldsymbol{\xi}\boldsymbol{\nabla}p_0)\boldsymbol{\nabla}\boldsymbol{\xi}}\right]dV \tag{2.41}$$

The underlined terms can be negative and thus destabilizing. According to these two terms, MHD instabilities are driven by pressure gradients (pressure driven modes) like

interchange or ballooning modes or by current (current driven modes) like kink modes [25].
Resistive modes can appear when the resistivity $\eta \neq 0$ plays a role in the MHD equations. Then flux can be produced or destroyed in Ohm's law and the flux surface topology can be changed. Finite resistivity allows magnetic field lines to reconnect and to form magnetic islands. Resistive modes are called tearing modes. An example of the spatial structure of a (2,1)-tearing mode is shown in Fig. 2.12. In ITB scenarios with reversed q profile (see Fig. 2.10), so-called double tearing modes (DTM) sometimes appear, if two tearing modes with the same helicitiy (m,n) couple. In the case of a (2,1)-DTM two $q = 2$ rational surfaces exist.

The tearing modes rotate with respect to the lab frame due to the plasma rotation

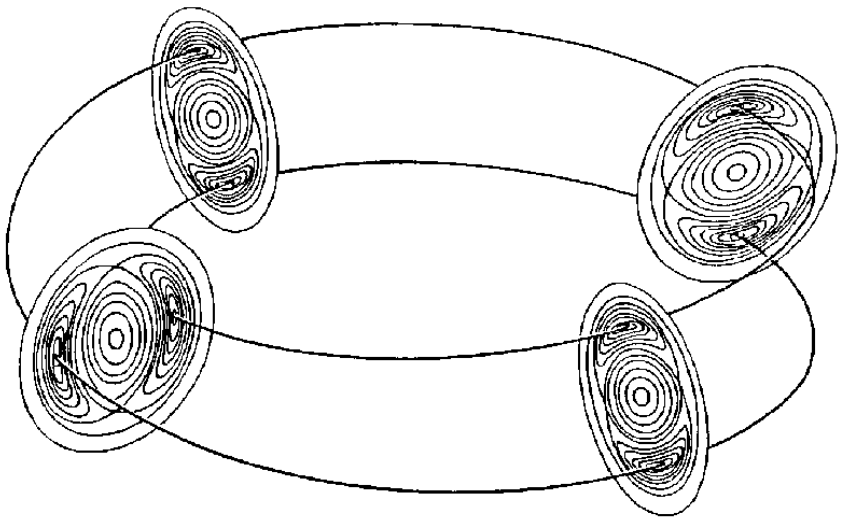

Figure 2.12: Example of a (2,1)-mode

and produces variations of the magnetic field which can be detected by magnetic probes (Mirnov coils[8]). Additionally the MHD modes can rotate within the plasma rest frame by diamagnetic effects and have a real frequency within the plasma. The MHD instabilities can also be detected by the Soft X-ray diagnostic. Analysis of both diagnostic measurements, Soft X-ray and Mirnov, allows to determine the poloidal (m) and toroidal (n) mode numbers.

2.6 Transport Analysis with ASTRA

The ASTRA [31], [10] (Automated System for TRansport Analysis in a Tokamak) transport code is the main tool in ASDEX Upgrade for transport and current diffusion studies.

[8]Array of coils in a single poloidal plane which measures the magnetic perturbations.

ASTRA is a fluid code for predictive and interpretative transport modeling. ASTRA contains a system of 2D equilibrium equations, 1D diffusion equations for densities and temperatures and a wide range of other modules describing additional heating, current drive and transport models in the plasma discharge. The NBI heating power distribution is implemented as a subroutine [32] in the code. The basic set of transport equations in the ASTRA code includes equations for the electron density n_e, electron temperature T_e, ion temperature T_i, the poloidal flux, the electron/ion fluxes Γ_e and the electron/ion heat fluxes $q_{e,i}$. ASTRA provides the possibility to retain only those terms and equations of the transport equations which are necessary for a specific problem.

In the simulations presented in this thesis (chapter 4), experimentally measured profiles of n_e, T_e and T_i (interpretative) are used instead of models (predictive). The equilibrium solver of ASTRA solves the Grad-Shafranov equation and is limited to plasma configurations without X-point [9].

The longitudinal Ohm law is assumed to be:

$$j_{\parallel} = \underbrace{\sigma_{\parallel} E_{\parallel}}_{j_{OH}} + j_{BS} + j_{CD} \tag{2.42}$$

where j_{OH} is the ohmic current density related to the electric conductivity $\sigma_{\parallel}$, j_{BS} is the bootstrap current and j_{CD} is the current density driven by external sources like ECCD or NBCD (neutral beam current drive). The initial conditions play a significant role in transient phases like the current ramp-up phase. The current density, $j_{\parallel}(\rho)$, or the rotational transform $\mu(\rho) = 1/q$ can be prescribed as an initial condition, although they are usually not known in the early phase of a tokamak discharge. However in the ASTRA simulations in this thesis (chapter 4) an initial q profile, computed with CLISTE, at an early time point, $t = 0.3$s directly after switching on the NBI source was used. The value of the experimentally measured total plasma current, I_{Pl}, can be used for the normalizations of the current density or rotational transform profiles by adjusting the profiles with

$$j_{\parallel}(\rho, t)|_{t=0} = j_0(\rho) \tag{2.43}$$

$$\int_0^{\rho_B} J^{-2} j_0 V' d\rho = 2\pi R_0 I_{Pl} \tag{2.44}$$

$$\mu(\rho, t)|_{t=0} = \frac{\bar{\mu}(\rho)}{\bar{\mu}(\rho_B)} \frac{\mu_0 I_{Pl}}{2\pi B_0 \rho_B G_2(\rho_B)} \tag{2.45}$$

where $V' = \frac{\partial V}{\partial \rho}$, $\rho = \sqrt{\Phi/\pi B_0}$, $G_2 = \frac{V'}{4\pi^2}\langle(\nabla\rho/r)^2\rangle$ and $J = \frac{I}{R_0 B_0}$. The initial condition with the plasma current distributed according to the steady state condition $\frac{\partial \psi}{\partial t} = U_{pl}(\rho) = const.$ and for $\dot{B}_0(t = 0) = 0$ using the parallel Ohm's law:

$$(j_{\parallel} - j_{BS} - j_{CD}) = \frac{2\pi\rho}{V'}\sigma_{\parallel} = C_{\sigma}\frac{\rho}{V'}\sigma_{\parallel}(\rho) \tag{2.46}$$

[9] X-point is a point where the poloidal magnetic field vanishes and two flux surfaces appear to cross in the poloidal cross section.

can be used when the direct measurement of the current density is not available, although the current relaxation time in a tokamak is long. The factor C_σ can be found from the total current I_{Pl}. The normal current penetration time is of the order of $\mu_0 a^2/\eta$ where a is the minor plasma radius and $\eta = 1/\sigma$ is the resistivity. An often used boundary condition is

$$\frac{\partial \Psi}{\partial \rho}|_{\rho=\rho_B} = \frac{\mu_0}{G_2(\rho_B)} I_{Pl}(t). \tag{2.47}$$

2.6.1 Limitations

As mentioned before, one limitation of ASTRA is that the equilibrium solver (solving the Grad-Shafranov equation) assumes only non X-point plasmas which do not correspond to the normal discharge configuration in ASDEX Upgrade. It can handle no 'current hole' equilibria, with an extended central region nearly zero poloidal magnetic field. There are also problems in ASTRA with the fitting of edge profiles with insufficient radial extension. Gradients may be mistaken. In H-mode, this has also consequences for the complete q profile and the current density inside the plasma. In the NBI routine of ASTRA the time dependent beam slowing down is not included. This can lead to a wrong assumption about the fast particle distribution function. The NBI routine uses a simplifying 'pencil' approximation instead of a Monte Carlo simulation which is more accurate. However the computations of the two methods are well adjusted and in good agreement. Near the magnetic axis the ion orbits can be 'potato' orbits instead of banana orbits which are used in the neoclassical calculations in ASTRA. The effect of potato orbits change the neoclassical electrical resistivity, the bootstrap current, radial particle and heat fluxes near the magnetic axis in reversed shear plasmas. Electrical resistivity and radial transport are enhanced over their standard neoclassical values in the case of potato orbits. Presently no module in ASTRA exists which can compute a bootstrap current driven by fast particles. This computation would be needed in chapter 4 as a possible further off-axis current source.

2.6.2 Bootstrap Current

There are different expressions for the bootstrap current which are valid in either the $\epsilon \to 0$ (high aspect ratio, inverse aspect ratio $\epsilon = r/R$) [33] or $\nu_{*e} \to 0$ (collisionless regime) [34] limit. Approximately the bootstrap current density j_{BS} is is proportional to the pressure gradient divided by B_p. A more general description of the bootstrap current, produced by gradients of the electron pressure, p'_e, ion pressure, p'_i, electron temperature, T'_e, and ion temperature, T'_i, but mainly by the gradient of the electron density, n_e, is [35]:

$$j_{BS} = f(B,\epsilon) e p_e \left[K_1 \left(\frac{p'_e}{p_e} + \frac{T_i}{Z_{eff} T_e} \left(\frac{p'_i}{p_i} - \alpha \frac{T'_i}{Ti} \right) \right) - K_2 \frac{T'_e}{T_e} \right] \tag{2.48}$$

where the definition of f, $K_{1,2}$, α depends on the respective model. f is a function of B and/or the inverse aspect ratio ϵ depending on the bootstrap model. K_1 and K_2 are either a function of the collisionality of the electrons [10] $\nu_{*e} \propto R_0 n_e / T_e^2$, of the ions [11] ν_{*i} and Z_{eff} or of the ratio of trapped to circulating particles x and Z_{eff}. α is a function of either the collisionality and the inverse aspect ratio or only of x.
However, some models have tried to combine all regimes with arbitrary shape and collisionality as described in [35], [36] and [37]. In [36] the work of [33] and [34] is extended using the exact Fokker-Planck operator. In this way the neoclassical resistivity and the coefficients for the bootstrap current can be determined for the banana regime. The effect of potato orbits near the magnetic axis is not considered. The flux surface averaged parallel current from [36] is defined as:

$$\left\langle j_{\parallel} B \right\rangle = \sigma_{neo} \left\langle E_{\parallel} B \right\rangle - I(\Psi) p_e \left[L_1 \frac{p}{p_e} \frac{\partial \ln p}{\partial \Psi} + L_2 \frac{\partial \ln T_e}{\partial \Psi} + L_3 \alpha \frac{1 - \frac{p_e}{p}}{\frac{p_e}{p}} \frac{\partial \ln T_i}{\partial \Psi} \right] \tag{2.49}$$

where the functions $L_1,\ L_2,\ L_3$ depend on the collisionality ν_{*e}, Z_{eff} and the trapped particle fraction, α depends on the ion collisionality ν_{*i}, the main ion charge Z_i, and the trapped particle fraction, $I(\Psi) = R B_\phi$. The neoclassical conductivity σ_{neo} is a function of T_e, n_e, Z_{eff}, the electron collisionality ν_{*e} and the trapped particle fraction.
All these models are implemented in ASTRA.

[10] depends on T_e, n_e , q and ϵ
[11] depends on T_i, n_i, q and ϵ

Chapter 3

MSE Diagnostic at ASDEX Upgrade (AUG)

In this chapter the MSE diagnostic at ASDEX Upgrade (AUG) and its improvements towards a real-time diagnostic will be shown. The improvements of the MSE diagnostic include hardware with ADC cards in a fast computer and software to replace hardware lock-ins necessary in the present MSE diagnostic. The improvement of the MSE diagnostic system (see Sect. 3.2) allows the study of structures in MSE measurements time correlated to MHD activity as will be described in Sect. 3.4 in more detail.

3.1 Introduction of the MSE Diagnostic at AUG

The MSE diagnostic in ASDEX Upgrade measures the polarization angle γ_m on the σ line which is perpendicular to the electric field polarized component. Fig. 2.8 shows the spectrum around the D_α with the Doppler shifted beam emission consisting of the motional Stark effect spectrum of three energy fractions (partly overlapping).
In Fig. 3.1, the horizontal arrangement of the MSE diagnostic is shown. As the used heating beam (Q3) is inclined at 4.9° to the midplane of the torus, a horizontal observation geometry could not be realized. Also the unavailability of a tangential access for the beam observation, required the use of a mirror. Therefore the observation optics consists of a dielectric mirror followed by four lenses. These lenses image the neutral beam emission onto six vertically stacked 1mm diameter optical fibers for each of the ten spatial MSE channels[38]. However the polarization properties of the mirror bring in a systematic error into the polarization angle measurements[1]. The mirror and the lenses are inside the torus. The lenses are protected inside a tube with a vacuum window and they are located in a strong magnetic field. This causes Faraday rotation of the incoming polarization by the parallel component of the toroidal magnetic field. Therefore the polarization angle γ_m is afflicted with a magnetic field dependent offset.

[1]Therefore in-vessel calibrations including the mirror are necessary during an opening of the vessel

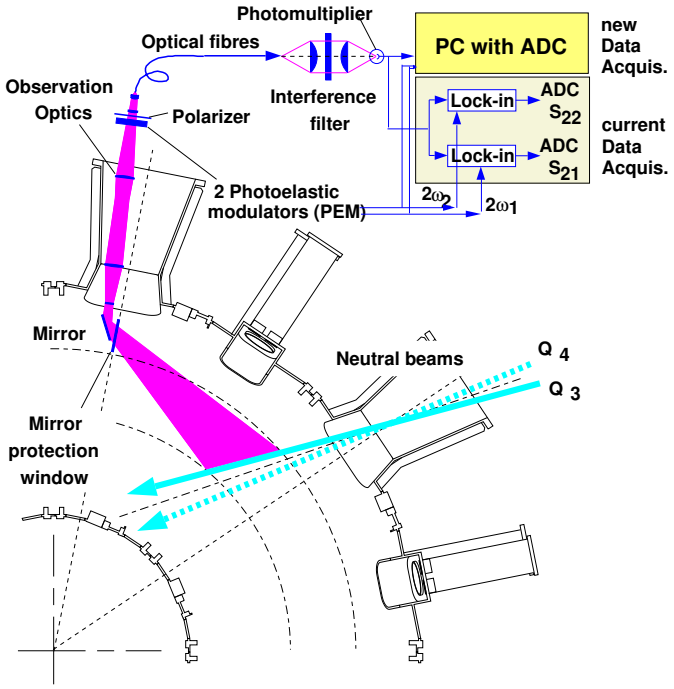

Figure 3.1: Overview of the MSE diagnostic from the top in ASDEX Upgrade

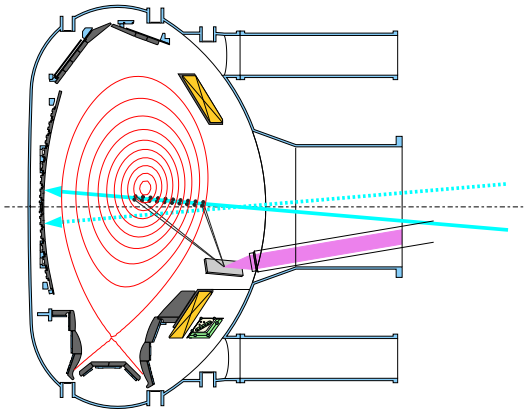

Figure 3.2: Overview of the MSE diagnostic in poloidal cross section in ASDEX Upgrade

It is necessary to calibrate the diagnostic with different magnetic fields. The measured polarization angle is then dependent of calibration parameters $p_0, p_1'(b_0), p_2'$:

$$\begin{aligned} s_2/s_1 &= p_0 \tan(2(p_2'\gamma_m + p_1')) \\ b_0 &= b_1 + b_2 B_t \end{aligned}$$

Outside the torus, in front of the optical fibers, a set of two **P**hoto**E**lastic **M**odulators (PEMs) and a linear polarizer are located for the polarization analysis. The optical fibers outside the vessel guide the signals to the interference filters into the photo-multipliers. With the current data acquisition system, the signals are analyzed with hardware lock-in amplifiers as described later.
The complex geometry of the MSE diagnostic at ASDEX Upgrade is reflected in the formula:

$$\tan\gamma_m = \frac{A_1 B_R + A_2 B_t + A_3 B_z + A_4 E_R/v_b}{A_5 B_R + A_6 B_t + A_7 B_z + A_8 E_R/v_b + A_9 E_z/v_b} \tag{3.1}$$

A_n are the geometry factors given from beam and diagnostic geometry inside the torus, B_R, B_z are the radial and vertical components of the poloidal magnetic field, E_R, E_z are the components of the radial electric field, v_b is the beam velocity. Typical measurement error of γ_m is about $0.2 - 0.3°$.
The MSE diagnostic provides a determination of the local magnetic field pitch angle $\gamma_p = \tan^{-1}(B_p/B_t)$ [2] which is proportional to the measured polarization angle γ_m

[2] B_p is the poloidal magnetic field, B_t is the toroidal magnetic field

($\gamma_p \approx \gamma_m$ for simple geometry and $E_r = 0$).
The magnetic field pitch angle is correlated to the safety factor $q(r)$ which is important for equilibrium and the stability of the plasma.
From γ_m, the current density profile $j(r)$ can be calculated. Because of the complex geometry of the MSE diagnostic at ASDEX Upgrade, the current density profile $j(r)$ and the safety factor profile $q(r)$ can mainly be determined with an equilibrium reconstruction code. The equilibrium reconstruction code CLISTE and NEMEC use the MSE measurements and magnetic probes as input data.

Representative Example for MSE Data

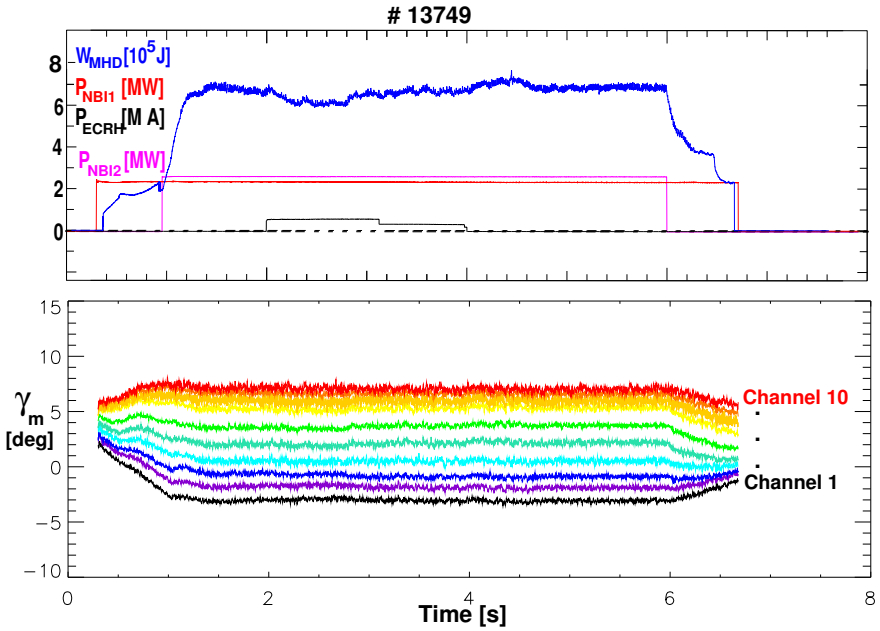

Figure 3.3: MSE measurements γ_m (below) and some plasma parameter of a discharge at ASDEX Upgrade with two neutral beams (5MW)

Fig. 3.3 shows typical MSE measurements in a discharge at ASDEX Upgrade together with plasma heating power from NBI, $P_{NBI1,2}$, and ECRH,P_{ECRH} and the plasma energy W_{MHD}). In Fig. 3.3 the 10 channels of the MSE diagnostic, channel 10 (red) is closest to the plasma center and channel 1 (black) at the Low Field Side (LFS). During the current ramp-up (increasing plasma current) between t=0-1s, the measured γ_m of each MSE channel separate as expected. Because the discharge is quite stable, the MSE channels do not show much change until the current ramp-down starting at about t=6s.

Functionality of the Polarization Analysis

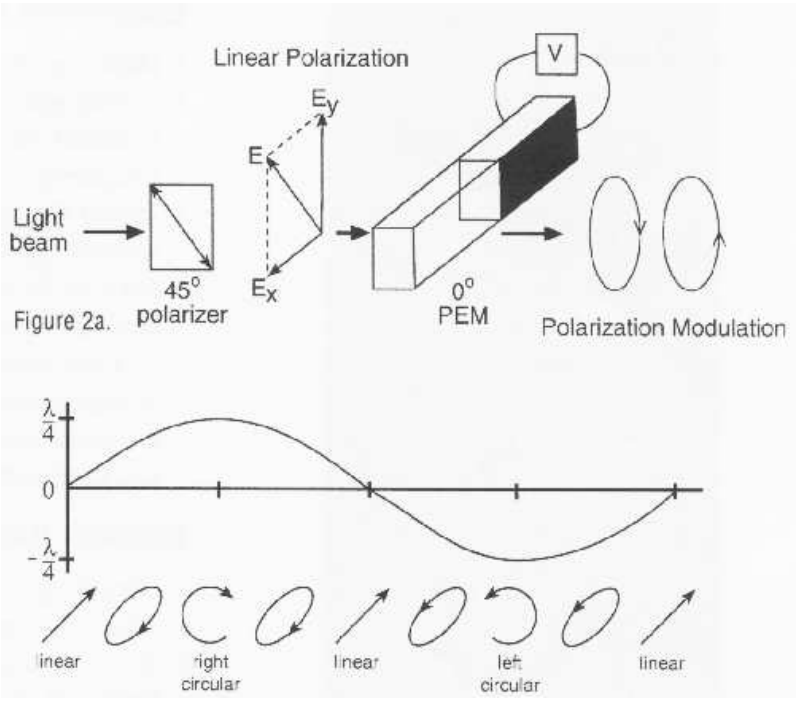

Figure 3.4: Function of the PEMs

The main component of the MSE diagnostic for analyzing the polarization are the two PEMs. The light travels through them with unchanged polarization if the optical element of the PEM is relaxed. However if the material is stressed by compression or stretching (here by a piezo element) the material becomes birefringent. This means for example that the polarization components of the light parallel or perpendicular to the modulator axis pass through the material at slightly different speeds. The phase difference between the two components oscillates as a function of time and is called the retardance or retardation.
If the maximum (peak) retardation reaches exactly $\lambda/4$, the PEM acts as an oscillating $\lambda/4$ plate. The polarization oscillates between right circular and left circular with other polarization states between (Fig. 3.4).
If the peak retardation is $\lambda/2$, the PEM behaves as an oscillating $\lambda/2$ plate. Then the polarization is modulated between two orthogonal linearly polarized states at twice the PEM's frequency (2ω). This is used in the MSE diagnostic to analyze the polarization (it's called Stokes polarimetry)[16]. Used in Stokes polarimetry, a net circular polarization component produces an electrical signal in the detector at the modulator frequency (1ω). A net linear polarization component at 45° in reference to the modulator axis produces an electrical signal in the detector at twice the modulator frequency (2ω: 40 kHz, 46 kHz at ASDEX Upgrade).

In Fig. 3.5 the setup of the PEMs at ASDEX Upgrade for measuring the polarization angle is shown.

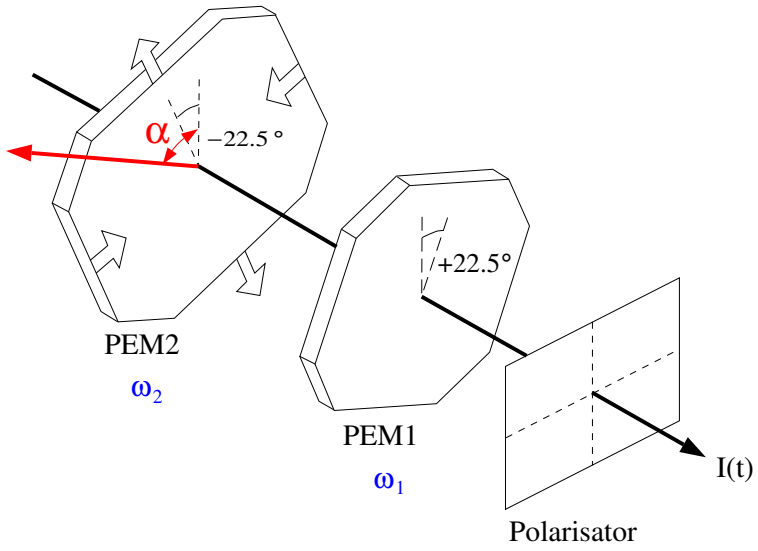

Figure 3.5: Setup of the two PEMs and the linear polarizer at ASDEX Upgrade

The polarizer in front of the two PEMs transforms the phase modulation ($\Phi = \Phi_0 cos\omega t$) in an intensity modulation:

$$\begin{aligned} 2I(\lambda) &= (I_\sigma(\lambda) + I_\pi(\lambda) + I_b) \\ &\quad +(I_\sigma(\lambda) - I_\pi(\lambda)/\sqrt{2} \cdot (-cos\delta_1 cos2\alpha + cos\delta_2 sin2\alpha - sin\delta_1 sin\delta_2 sin2\alpha) \\ \delta_{1,2} &= cos(\Phi_0 cos\omega_{1,2} t) = J_0(\Phi_0) - 2J_2(\Phi_0) cos(2\omega_{1,2} t) + ... \end{aligned}$$

$J_2(\Phi_0)$ [3] has a maximum for $\Phi_0 \approx \pi$

The modulation amplitudes at $2\omega_{1,2}$ are

$$s_1(2\omega_1) = -((I_\sigma(\lambda) - I_\pi)/\sqrt{2} J_2(\Phi_0) cos2\alpha \quad (3.2)$$

$$s_2(2\omega_2) = -((I_\sigma(\lambda) - I_\pi)/\sqrt{2} J_2(\Phi_0) sin2\alpha \quad (3.3)$$

and can be determined by Fourier transformation or lock-in technique:

$$s_2/s_1 = -\tan 2\alpha \propto \tan 2\gamma \quad (3.4)$$

[3] $J_n \hat{=}$ Bessel function of n-th order

3.2 The new MSE Data Acquisition in AUG

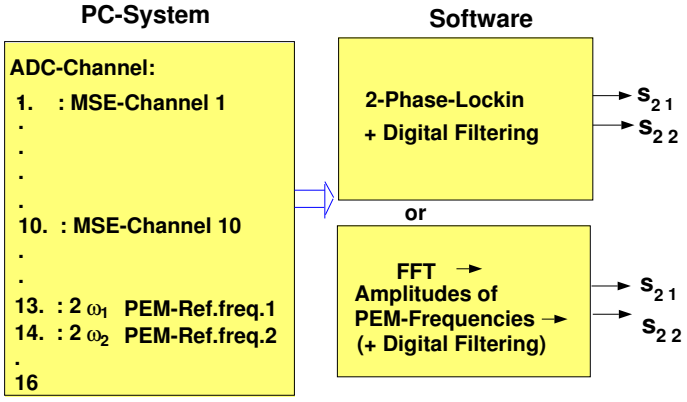

Figure 3.6: Scheme of the new data acquisition: On the left hand side, the assignment of the ADC card channels in the computer is shown, on the left hand side, a short description of the two different software solutions to deliver by signal processing an equivalent of the hardware lock-in amplifiers.

A new MSE data acquisition system with ADC card in a PC was designed to be used on-line for real-time control of the current density $j(r)$. The sampling rate of this system is 190 kHz instead of 1 kHz in the current MSE system. Without analog lock-in amplifier in the new system, it was necessary to find a software solution to obtain s_1, s_2. There are two different possibilities, namely a program with a 2-phase-lock-in process and digital filter or a program which uses the Fast Fourier Transformation (FFT) (Fig. 3.6). In the FFT method the signal of the ADC (Fig. 3.7) is transformed for each MSE channel with FFT into a frequency spectrum. The absolute amplitudes at $2\omega_1 = 46, 2\omega_2 = 40$kHz [4] in the frequency spectrum are identified as the components of the linear polarized light of the beam emission s_1, s_2. The ratio of the two amplitudes at $2\omega_{1,2}$ correspond to the ratio of s_2/s_1:

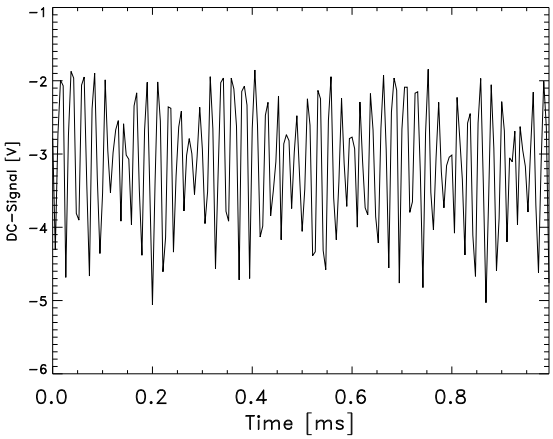

Figure 3.7: ADC signal for one MSE channel of a plasma discharge, sampled at 190kHz; time period is 1ms.

$$s_2/s_1 = \frac{\text{abs.Amplitude(40kHz)}}{\text{abs.Amplitude(46kHz)}} \tag{3.5}$$

[4] notation: ω equivalent to f; $s_1, s_2 \hat{=} s_{21}, s_{21}$,

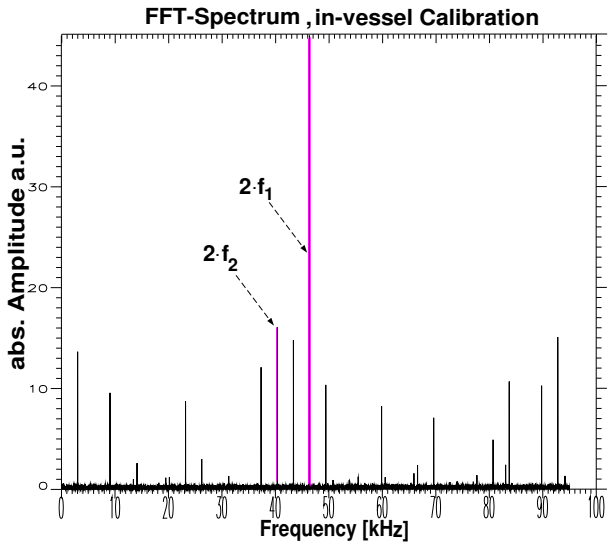

Figure 3.8: MSE FFT spectrum of in-vessel calibration in ASDEX Upgrade with the amplitudes at $2\omega_{1,2} = 46, 40$kHz in magenta

In Fig. 3.8 the FFT frequency spectrum of an in-vessel calibration [5] without plasma is shown up to the Nyquist frequency at $f_N = \frac{1}{2\Delta} = \frac{1}{2}f_s$ (Δ is the sampling rate,f_s is the sampling frequency, here 190kHz). Since there is no plasma, the frequency spectrum shows only the frequencies produced of the MSE setup, mainly of the PEM and the mirror. The peaks at 40 and 46 kHz, highlighted in magenta, are the second harmonic of the PEM frequencies. The small peaks at 20 and 23 kHz (modulation frequency of the PEMs) are related to a circular polarized component caused by the mirror of the MSE diagnostic inside the vessel. The other peaks (e.g. 3, 6, 9, 12, 60, 80 kHz etc.) are mixed-frequencies or higher harmonics of the PEM frequencies.

The FFT program uses at least 190 sample points ($\hat{=}$1ms time interval) for the FFT because of a minimum signal-to-noise-ratio ($\frac{S}{N}$) and frequency resolution (at least 1kHz). Since the program is planned to be used for the real time control of the current profile $j(r)$ in ASDEX Upgrade, the performance has to be optimal. Therefore the use of 256 sample points ($\approx$ 1.35ms time resolution) is more effective. To reduce artifacts in the FFT spectrum, the mean value (DC-offset) of the data sample of 256 points is subtracted and the sample is multiplied with a Hanning filter before the FFT. The Hanning filter is defined as:

$w(i) = 0.5 + 0.5\cos(2\pi i/W)$ for $-W/2 <= i <= W/2$ else $w(i) = 0$

($W\hat{=}$ size of the data sample). This windowing with a Hanning filter is a good tradeoff between simplicity and sideband suppression. After FFT, the program searches for the maxima around 40 and 46 kHz in the frequency spectrum and forms the absolute am-

[5] in-vessel calibration: light source inside the vessel in place of the observation volume with plasma operation during an opening of the torus

plitudes of the peaks. The absolute amplitudes are identified as s_1, s_2. The polarization angle γ_m is then computed from the ratio of s_2, s_1 as mentioned above. To reduce the noise of the computed γ_m the signals can be smoothed with digital filtering. However, for the real time control this is too time consuming and not absolutely necessary. Fig 3.9 shows an example of γ_m computed with the FFT method (upper) in comparison with the present MSE data acquisition (lower) with hardware lock-ins. The two plots are different, because the computed γ_m of the new system is not calibrated yet. Running on a system with a Pentium III 1GHz the FFT program needs 12s to compute 10s data of the 10 MSE channels. The performance has to be improved 20% to reach the needed speed for real-time operation.
The second program uses a 2-phase-lock-in process which applies the two PEM reference frequencies at $2\omega_{1,2}$. Both methods are frequency and phase independent.

ICRH (Ion Cyclotron Resonance Heating) Effects on MSE in AUG

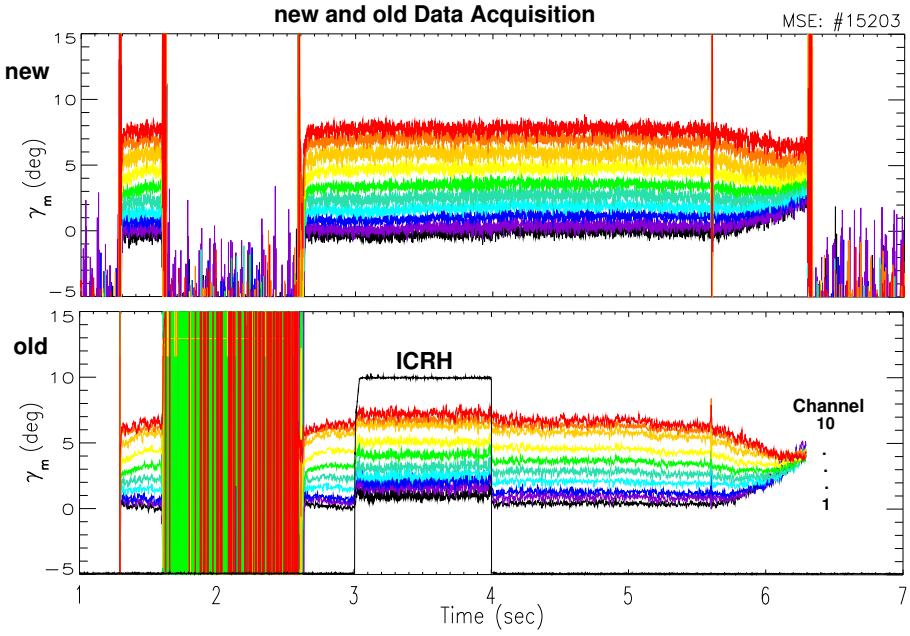

Figure 3.9: Correction of the ICRH perturbation in the MSE measurements with γ_m from FFT (upper) in comparison with γ_m from present MSE system (lower).

As seen in Fig. 3.9, the operation of the Ion Cyclotron Resonance Heating (ICRH) causes perturbations in the present ('old') MSE diagnostic possibly with launching electric signals in the cables of the MSE diagnostic which could generate phase perturbations [6]. The hardware lock-in amplifiers need phase-true signals. Because of the independence of phase of the new data acquisition, the perturbations caused by

[6]The perturbations are not yet further investigated

ICRH can be 'corrected'.

Comparison of frequency spectrum of in-vessel calibration and plasma discharge in AUG

Fig. 3.10 shows the comparison of the frequency spectrum of in-vessel calibration and

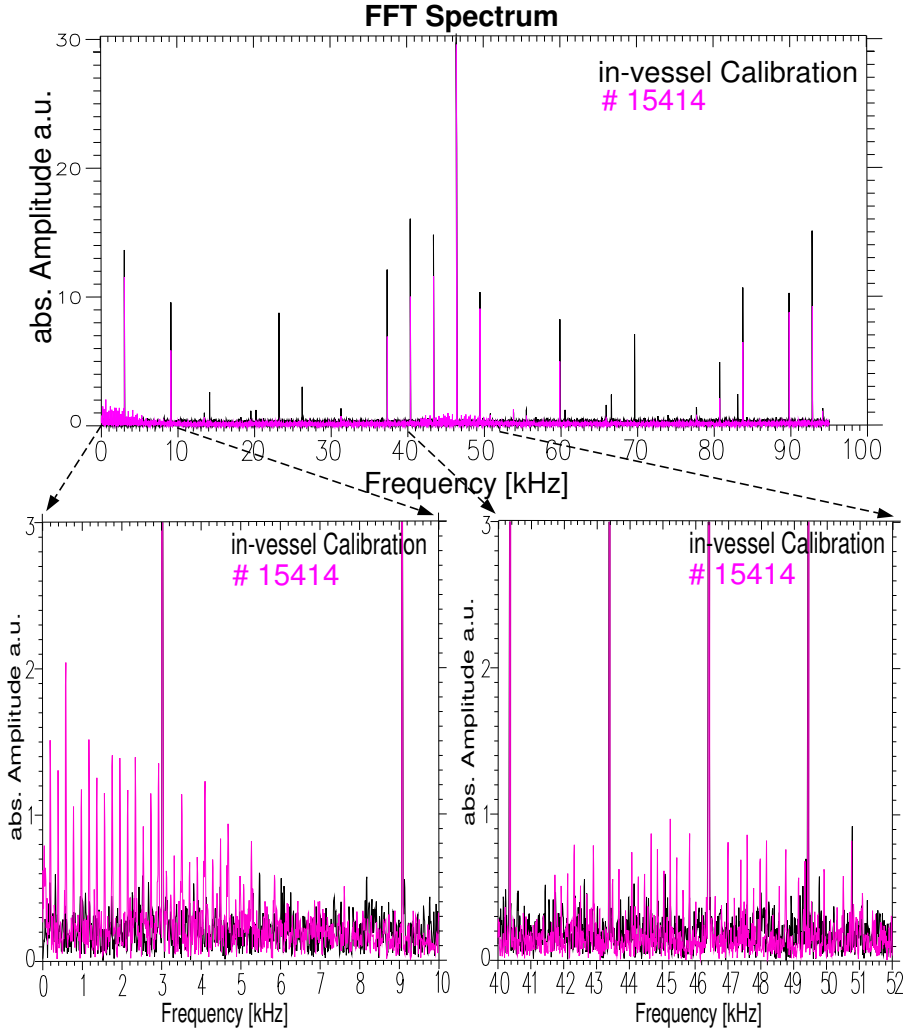

Figure 3.10: MSE FFT spectrum of plasma discharge and in-vessel calibration (black) and two frequency cut-outs

plasma discharge to distinguish between PEM and other frequencies like possible fluctuations in the beam emission. Additional frequency peaks between 0 and 6 kHz in the plasma discharge can be seen in the cut-outs of the spectrum in Fig. 3.10, which are not observable in the in-vessel calibration. This could be due to beam energy, beam density or plasma density fluctuations reflected in the beam emission light and needs more investigation. Some peaks can also be seen shifted with 40 and/or 46 kHz which could be a linearly polarized fraction (possibly field fluctuations). There is no diagnostic available

at ASDEX Upgrade which could measure the beam energy directly. The measurements of the beam energy with an oscilloscope has not enough time resolution and the FFT frequency spectrum shows only a broad peak at $0 - 2$keV.

3.3 Sensitivity of the MSE Diagnostic to magnetic Field Perturbations

With the new data acquisition and the FFT program it is possible to study the direct influence of MHD activity like NTMs on MSE measurements. The modes cause perturbations of the magnetic field, which should be seen in the frequency spectrum of the MSE if the MSE diagnostic is sensitive enough to measure the magnetic field perturbation of the mode.
In Fig. 3.11, an approximation of the variation of γ_m with a change of 5 % and 10% of the local poloidal magnetic field B_p is shown. For this approximation, the magnetic field configuration of a discharge (#13149, upper single null ITB discharge) is reconstructed with CLISTE. The magnetic field components of this CLISTE equilibrium are used in the geometric formula 3.1 for γ_m. In this example the change of γ_m is approximately $0.0 - 0.6°$ from the inner to the outer channels for the 10% change.

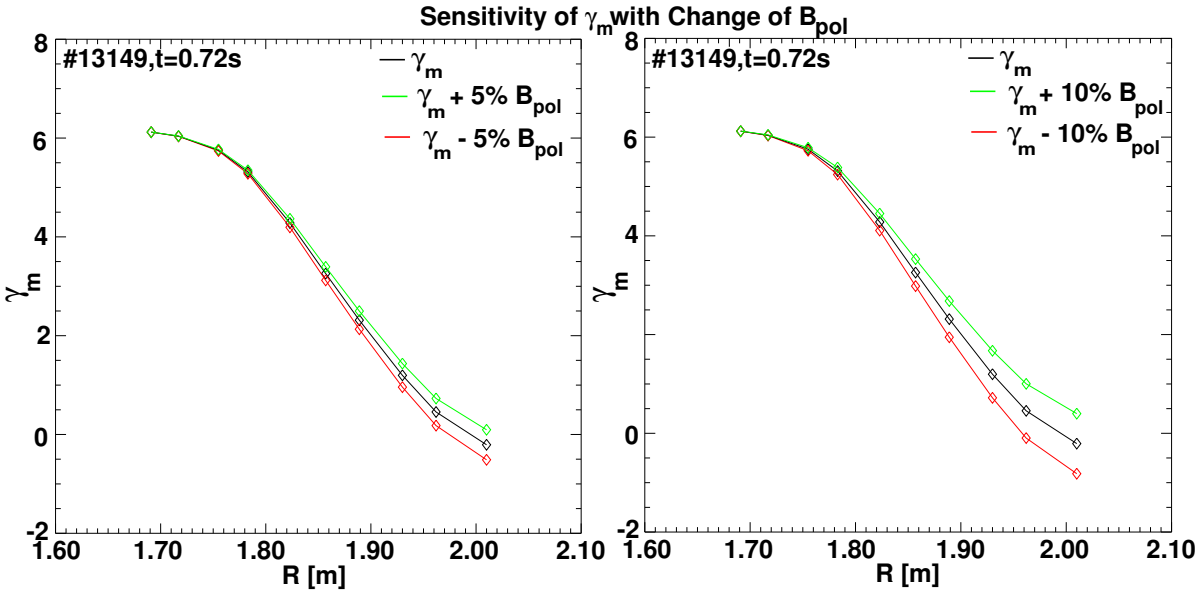

Figure 3.11: #13149, $t = 0.72s$: γ_m computed with in-/decreased $B_{pol}(\pm 5/10\%)$

Typical magnetic perturbation by a mode are only a few percent of the poloidal magnetic field. Those small perturbations could only be seen in the outer MSE channels and hardly in the inner channels. However, the magnetic perturbation of a fast rotating mode (usually higher than 5 kHz) should not be visible on the current MSE

data acquisition with 1 ms time resolution ($\hat{=}$ 1kHz). The time averaged perturbation of the mode is about zero. Possible secondary effects in the current density profile are smaller than the error bars of the MSE measurements and are not detectable so far. The question is, if the magnetic perturbation of a rotating mode can be seen with the new MSE data acquisition (sampling frequency 190kHz). For this purpose a discharge with a (3,2)-NTM was repeated. During the existence of this mode a R-scan [7] (5cm outwards t=3.2-4.0s and 5cm inwards t=4.0-4.8s) is performed and the mode changes its frequency during the scan. Fig. 3.12 shows a wavelet plot (frequency over time) of this discharge including the position of the plasma edge R_{aus}. With the FFT program and the new data acquisition for the MSE the frequency spectrum of the MSE and the frequency spectrum of the Mirnov [8] can be compared. The Mirnov FFT spectrum (Fig. 3.14) shows the magnetic field perturbation caused by the (3,2)-NTM at $\approx$ 16 kHz at, t=3.4s averaged over 100ms. Fig. 3.13 shows the FFT frequency spectrum of MSE channel 7 at the same time point. The frequency of the (3,2)-NTM (intensity fluctuation caused by the mode) can only be seen marginally above the noise level in all MSE channels. The small frequency peak of the mode can be identified due to the frequency change of the mode during the R-scan which can also be seen in the MSE frequency spectra at different time points.

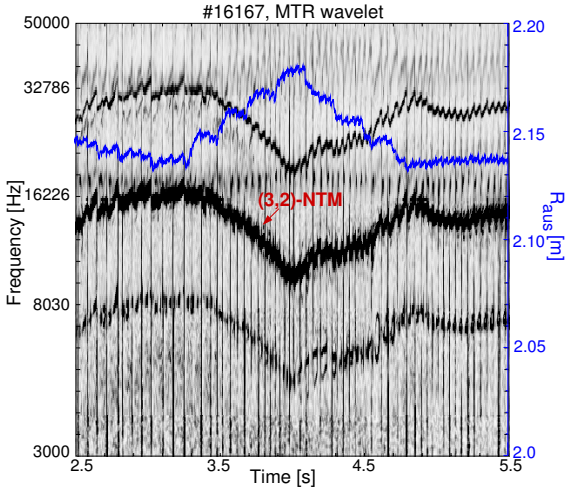

Figure 3.12: Mirnov time-frequency plot of #16167 shows the (3,2)-NTM during the R-scan

The possibly polarized fraction of this intensity fluctuation due to perturbation of the poloidal field, shifted with 40 and 46 kHz (the PEM frequencies) respectively, is not visible in the MSE frequency spectrum. The magnetic field perturbation is possibly too small and the polarized fraction lies below the noise level. This shows that the MSE diagnostic is not sensitive enough to detect magnetic field perturbation of a mode directly. The frequency of the mode due to intensity fluctuation can hardly be seen with the new data acquisition. Thus structures correlated to modes, as described in the next chapter, are not a direct net effect due to the poloidal magnetic field perturbation of the rotating mode.

[7] The plasma is shifted outwards and inwards on the radial axis R_{maj}

[8] Mirnov diagnostic measures the time derivative of the magnetic field with coils

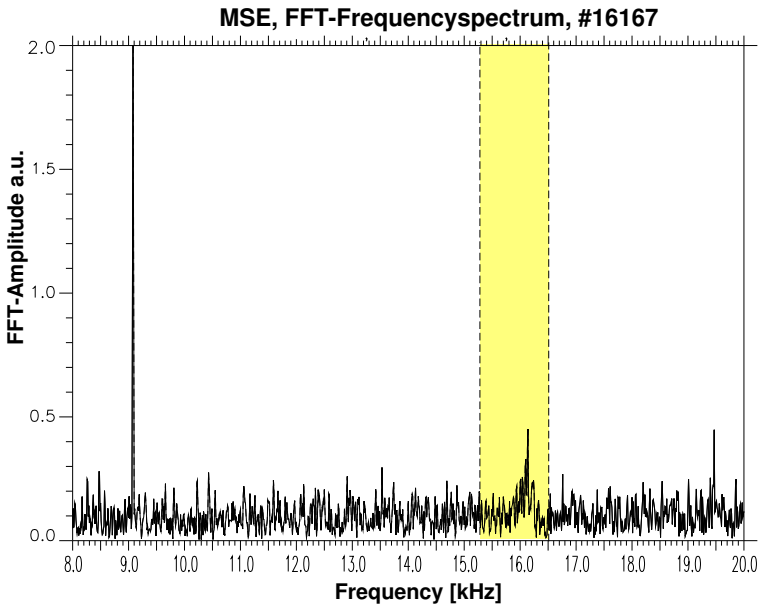

Figure 3.13: MSE FFT spectrum # 16167

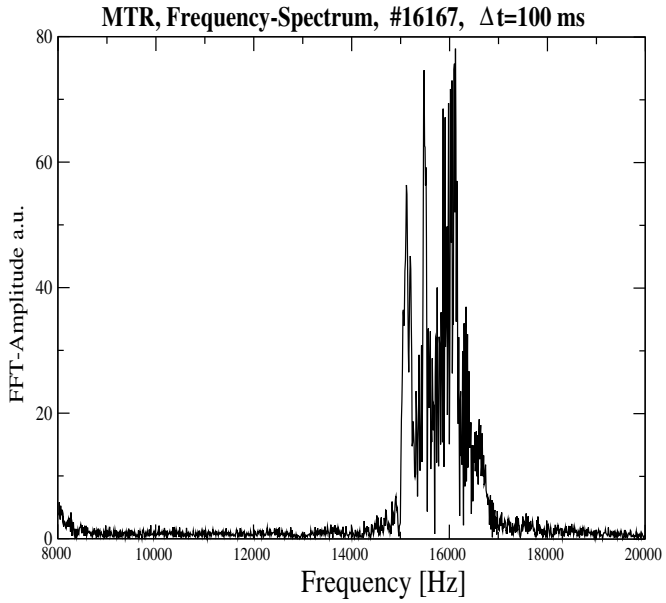

Figure 3.14: Mirnov FFT spectrum # 16167, t=3.4s, averaged over 100ms

3.4 Structures in MSE Measurements

In Fig. 3.15, the example of an ITB discharge at ASDEX Upgrade during the current ramp-up is shown. In this discharge a structure was recognized in the MSE measure-

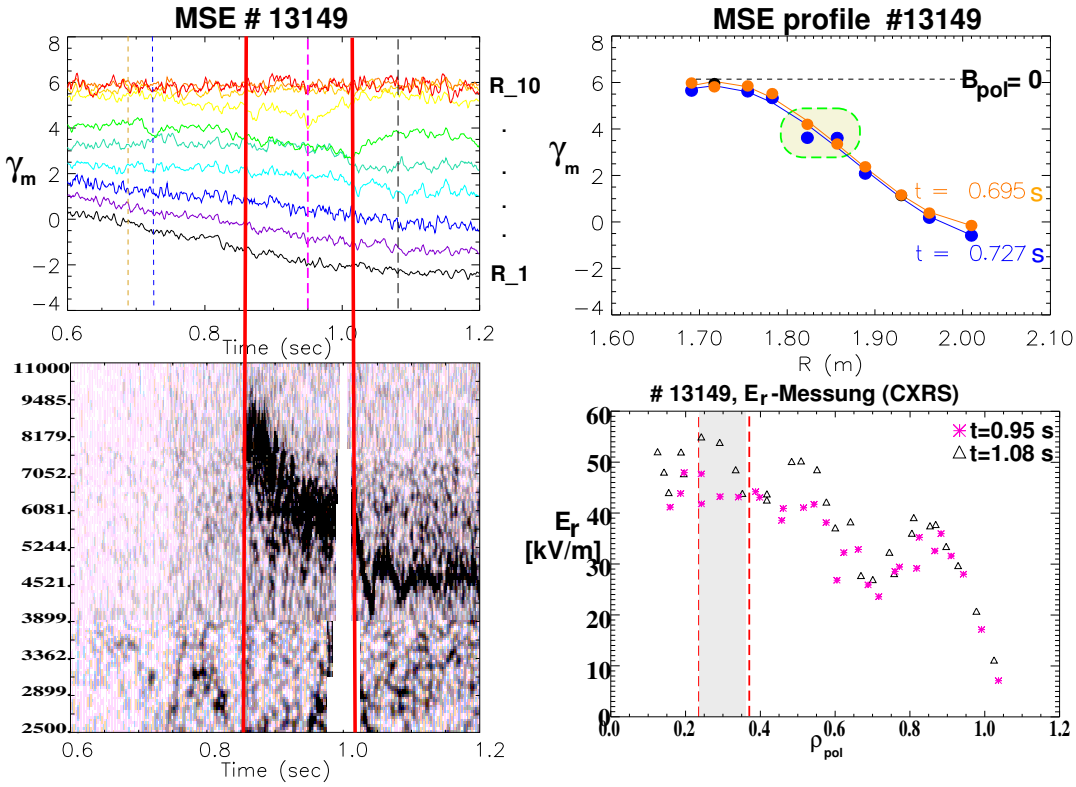

Figure 3.15: # 13149: MSE measurements, the Mirnov wavelet plot with the (2,1)-DTM, E_r measurements from CXRS from two different time points

ments for the first time which shows an interesting correlation with MHD instabilities. This discharge includes two type of structures. The first structure described here appears during a (2,1)-Double Tearing Mode (DTM) between t=0.7 – 1.0s. In the first plot, the MSE channels show a change of three channels in this time period. Two channels (here the two green channels R_5,R_6) first converge and then diverge after the DTM. Generally during a modification of the current density profile, the MSE channels show a uniform change of the gradient over a wide range (like in the current ramp-up phase). These two channels indicate a very localized modification of the profile as the upper right plot of Fig. 3.15 shows. This discharge has an strong ion ITB. During the ITB a strong radial electric field (a few 100kV/m) can appear. The measurements of the radial electric field E_r with CXRS show only a difference of a few 10kV/m. This is not enough to cause this change in γ_m. For a change of $\approx 1°$ in γ_m like here, a change of the radial electric field of about 100kV/m would be needed. Correlated in time to this structure in the MSE measurements is the (2,1)-DTM which is also located approximately at the position of the two channels. As shown before, the change in the profile can not be a direct effect of the magnetic field perturbation of the DTM. An explanation of this structure is a change in the equilibrium caused by the DTM. The structure in the MSE measurement could reflect the region with constant q in the

profile between the two $q = 2$ surfaces coupled by the (2,1)-DTM.
The second structure in this discharge is the 'current hole'. This feature will be described in more detail in the following chapter 4. The inner three channels lie together approximately at the value of $B_p = 0$ ($B_R, B_z = 0$), which is computed from the geometry formula 3.1. This means there is an extended central region with almost no current density. This is called a 'current hole'.

Effect of a Structure in MSE-Data in Equilibrium
Here the effect of a structure in the MSE measurements on the equilibrium reconstruction is shown. Because of the two simultaneous structures in the studied discharge #13149, an equilibrium reconstruction including both structures is not yet possible. To show the possible effect of a MHD instability, another example of a structure in the MSE measurement is used. Fig. 3.16 shows the effect of two MSE channels close to each other. A flat region in the q profile can be seen at this position.

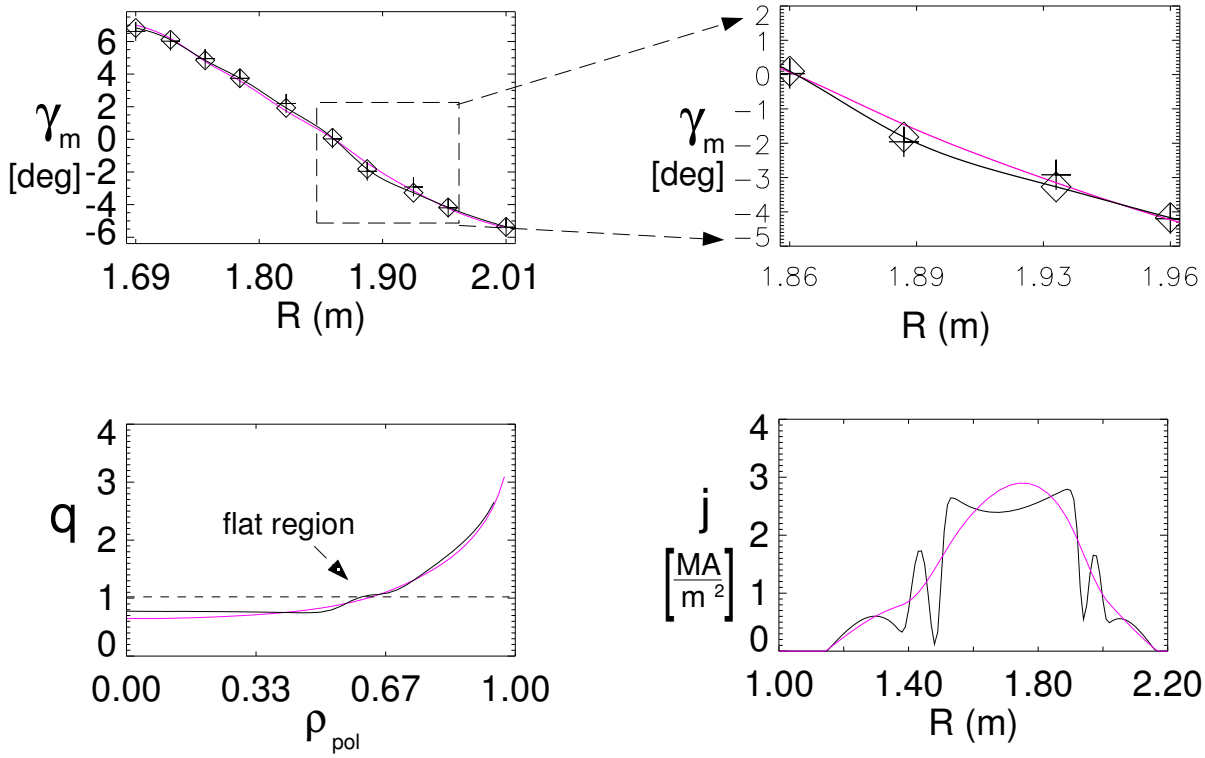

Figure 3.16: CLISTE results with/without structure

3.5 Summary and Discussion

A new MSE (Motional Stark Effect) data acquisition system was designed towards a real-time diagnostic to provide on-line measurement for the real-time control of the current

density $j(r)$. The sampling rate of the new system is 190 kHz instead of 1 kHz in the current MSE system. Without analog lock-in amplifier in this system, a software solution was necessary to replace the lock-in process. Two different approach for the software solution are possible. The first method uses a Fast Fourier Transformation (FFT) which identifies the ratio of the absolute amplitudes at the second harmonic of the PEM frequency in the frequency spectrum as the ratio of the components of the linear polarized light of the beam emission. The second approach uses a 2-phase-lock-in process. However, this method needs digital filtering which is time consuming and therefore not suited for the real-time process.
Owing to the discovery of certain structures in the MSE measurements time correlated with MHD-activity, the sensitivity of the MSE diagnostic to magnetic perturbations (caused by MHD activity) was tested. The study of the variation of the calculated γ_m with a change of the local poloidal magnetic field (in a realistic dimension of a magnetic perturbation) has shown, that this change could hardly be seen in the MSE measurements. The time resolution of the present ('old') MSE system is not high enough to follow the magnetic field perturbation of a rotating MHD mode. The new data acquisition system (high sampling frequency) with the FFT software program was used to test if a magnetic perturbation caused by an MHD mode could be seen directly in the frequency spectrum (from FFT program) of the MSE data. For this test, a discharge was repeated which has a NTM (neoclassical tearing mode) with a certain frequency. The frequency of the MHD mode in this discharge was only seen marginally above the noise level in the FFT spectrum of the MSE.
A possibly strong radial electric field during an ITB in the discharge with to the structure time correlated MHD mode was excluded as reason for the MSE structure. Therefore, this structure in the MSE measurements (time correlated with MHD mode, DTM in this special case) can only be an effect of a change in the equilibrium caused by the mode. The structure in the MSE measurement reflects the region with constant q in the profile between the two $q = 2$ surfaces coupled by the (2,1)-DTM. Another feature was found in this studied discharge, a so-called 'current hole', an extended central region with almost no current density. The inner MSE channel in this discharge lie in a region with constant poloidal magnetic field B_p, which can only be $B_p = 0$. This is described in the next chapter.

Chapter 4

'Current Holes'

In this chapter, the 'current hole' scenarios in ASDEX Upgrade and other experiments like JET[1] and JT-60U[2] will be described. The study of 'current holes' is important for predicting current profile evolution in next step facilities (like ITER) with high current diffusion time in advanced scenarios with strong non-inductive current (such as bootstrap current). First, an introduction of the phenomenon 'current hole' will be given. Then the experimental results of a 'current hole' scenario at ASDEX Upgrade will be shown. The equilibrium reconstruction with the new version of CLISTE and NEMEC, presented in chapter 2.4, is used for the 'current hole' equilibrium reconstruction. The current diffusion simulations, computed with the transport code ASTRA, of one discharge will also be shown in this chapter. A new experimental scenario for 'current holes' with ECCD pre-heating at ASDEX Upgrade, which was developed in the experimental campaign 2003, will be presented. Finally, the results will be summarized and discussed in the last section.

4.1 Introduction

Internal transport barriers (ITB) [6], [7], [8] in tokamak plasmas are explored because they improve confinement and stability beyond conventional scenarios. They offer a possible scenario for ITER, with a higher bootstrap current fraction as an essential part of the non-inductive current drive to partially replace the toroidal current produced by the transformer. An ITB can form more easily in the presence of low or negative magnetic shear $s = (r/q)(dq/dr)$ ($\hat{=}$ reversed q profile) in the core of the plasma. Low or negative magnetic shear can experimentally be produced by the injection of neutral beam or radio frequency heating into the current ramp-up phase of the discharge. The heating decreases the plasma resistivity and delays the penetration of the current from the edge to the core (increasing current diffusion time). This leads to a hollow current density profile due to the accumulation of the current in the outer region. In scenarios

[1] Tokamak experiment in Culham, U.K.
[2] Tokamak experiment in Naka, Japan

with extremely reversed shear (named as the 'current hole' scenario in JT-60U), the power threshold for the ITB formation is lower [39].

'Current hole' plasmas are characterized by a core region with a very small or zero current density as determined from Motional Stark Effect (MSE) diagnostic measurements (zero poloidal field B_p within the error bars of the MSE diagnostic corresponding to very high central q, $q_0 \rightarrow \infty$)[3]. The 'current hole' can develop if an off-axis peaked non-inductive current density exceeds the total current density (i.e. the off-axis non-inductive current drive is strong enough relative to the ohmic current). The toroidal electric field E_{tor} (or loop voltage) becomes negative there. The decrease of the loop voltage diffuses towards the center and reduces the central current density. This diffusion can cause zero or even negative toroidal current density in the center, as shown in Fig. 4.1. The off-axis non-inductive current in the 'current hole' discharges with only NBI is thought to be the bootstrap current. In JET discharges, the off-axis non-inductive current is produced with lower hybrid current drive (LHCD).

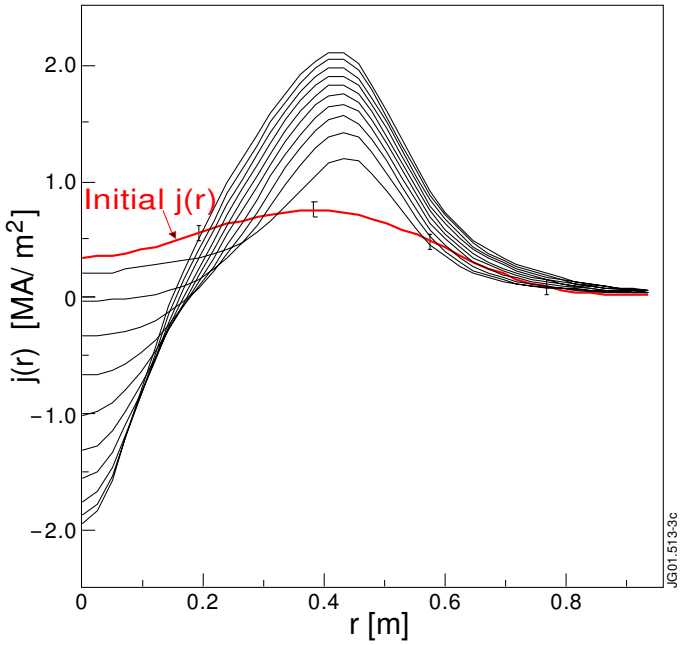

Figure 4.1: Modeling the response to off-axis current (LHCD) [40]

Since the confinement of particles in toroidal systems depends on the poloidal magnetic field, there is poor confinement inside the 'current hole'. The high temperature plasma can only be sustained by the ITB. Fig. 4.2 [30] shows the guiding center orbits of protons varying with the pitch angle of the velocity, the particle energy and the starting point, traced for t= 0.01s. The orbits are plotted together with surfaces of constant toroidal magnetic flux of a NEMEC equilibrium reconstruction of a 'current hole'

[3]A high value of q corresponds to a low poloidal magnetic field and low plasma current inside the flux surface

discharge #13149 in ASDEX Upgrade. The region of the 'current hole' is highlighted by the shaded area. Inside the current hole with $q > 1000$ the particles move straight up or downwards. The computations [30] show that the guiding center orbits become straight for $q \geq 100$. Outside the flux surface with $q = 10$, the particles follow ordinary orbits. Consequently, the profiles of temperature and density should be flat inside the 'current hole' region.

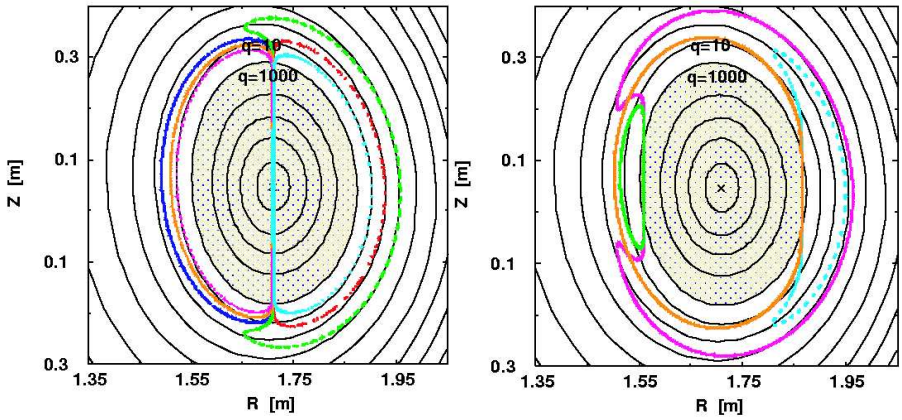

Figure 4.2: Poloidal cross section with toroidal flux surfaces of an reconstruction (NEMEC) of a 'current hole' (marked by the shaded area) equilibrium of #13149 at t= 0.65s [30] in ASDEX Upgrade and the orbits of the protons, traced for t= 0.01s.

The 'current holes' have already been observed in JET ITB experiments with LHCD [39] and in JT-60U ITB experiments with NBI during current ramp-up (with quite low density compared to corresponding experiments in ASDEX Upgrade) [41]. Measurements and calculations for a 'current hole' discharge in JT-60U are shown in figures Fig. 4.3 - 4.6 [41] as an introduction. JT-60U uses early balanced co- and counter-NBI (to minimize the beam driven current) during current ramp-up phase. The toroidal magnetic field B_t is 3.7T, the plasma current is 1.35MA. The current diffusion time in JT-60U is much larger than in ASDEX Upgrade due to the larger plasma radius (factor 2). Consequently, the 'current holes' can persist for several seconds. Fig. 4.4 shows the the poloidal cross section of a equilibrium reconstruction with 'current hole' (emphasized by the shaded area). The radius of the 'current hole' extends up to 40% of the plasma minor radius r. Fig. 4.3 shows B_z/B_t ($\approx B_p/B_t$) directly computed from MSE measurements of the three JT-60U MSE systems on the co- and counter NBI sources compared with the equilibrium reconstruction. Fig. 4.5 shows the radial profiles of ion and electron temperature, current density, safety factor q, electron density n_e and the toroidal velocity. In the profiles of the temperatures and the density, the flat regions inside the 'current holes' can be clearly seen. The current density inside the 'current hole' is nearly zero and has strong gradient at the edge of the 'current hole'. Until now, no negative central current density was reported in the different experiments, even though simulation shows the possible development of negative current density $j(0)$

through a negative toroidal electric field $E_{tor}(r = 0)$ as shown in Fig. 4.1. However, it seems that a mechanism exists to prevent the plasma current from becoming negative. At least one MHD mechanism has been identified which could cause the 'clamping' of the central current density at zero [42],[43].
In a NBI heated plasma, the bootstrap current is thought to be the off-axis non-inductive current which generates the negative E_{tor}. In Fig. 4.6 the different current density fractions, computed with a transport code, total current density j_{tot}, beam driven current density j_{BD} and bootstrap current density j_{BS}, are shown. The driven beam current is small due to the balanced co- and counter NBI. The bootstrap current density is comparable to the total current density. Since the bootstrap current j_{BS} is proportional to the pressure gradient divided by B_p, even with a small pressure gradient j_{BS} can be large near the 'current hole' with small to zero B_p.

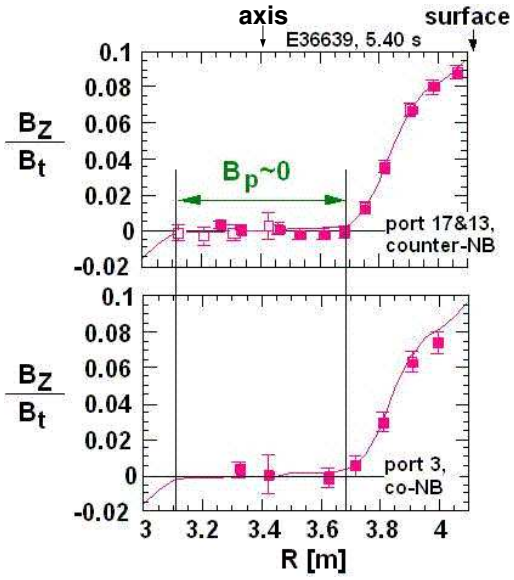

Figure 4.3: B_p/B_t as function of major radius R. The solid line shows the calculated values from equilibrium reconstruction, the squares denote the measured values from the three MSE diagnostics [41].

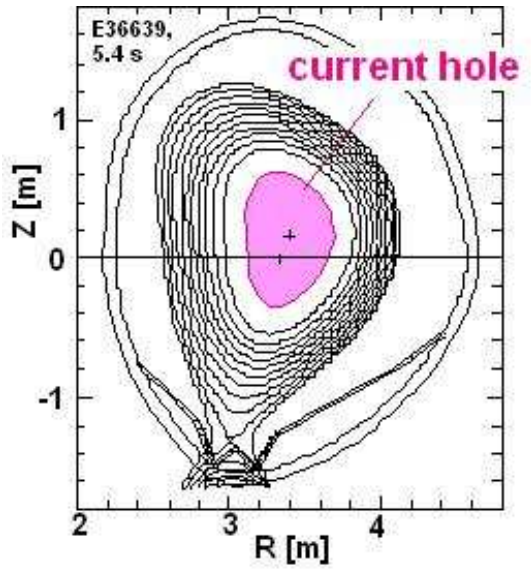

Figure 4.4: Poloidal cross section of plasma and MSE points in JT-60U. The 'current hole' is shown by the shaded area [41].

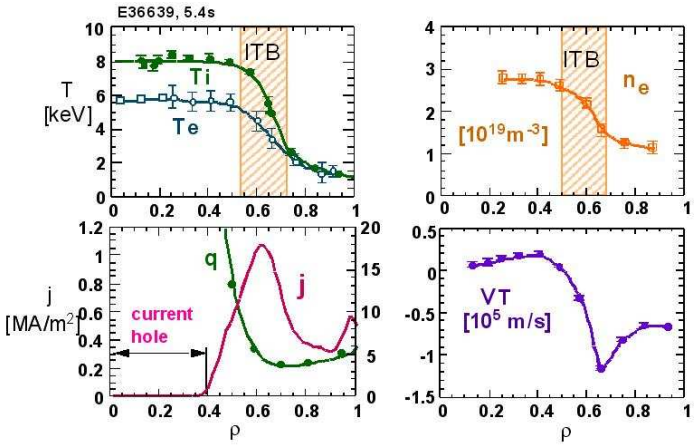

Figure 4.5: Radial profiles of ion and electron temperature, current density, safety factor q, electron density n_e and the toroidal velocity [41].

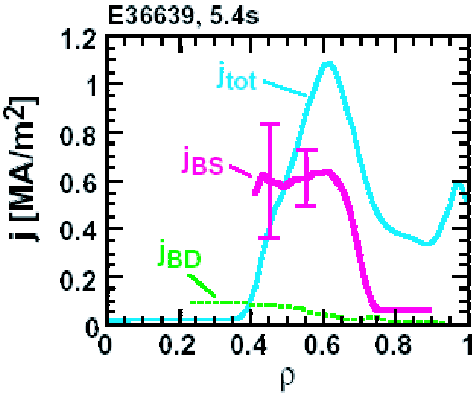

Figure 4.6: Radial profiles of j_{tot} reconstructed using MSE data, calculated j_{BD}, and the calculated j_{BS} [41].

In experiments in ASDEX Upgrade for the formation of ion Internal Transport Barriers (ion ITB's), simultaneous current ramping and Neutral Beam Injection (NBI) have also produced extremely reversed q profiles. The resulting 'current holes' can be stable for about one second. As shown in the next section, the temperature profiles of these discharges show the presence of an internal transport barrier.

4.2 'Current Holes' in NBI heated ITB Experiments at ASDEX Upgrade

4.2.1 Experimental Results

An example of a 'current hole' discharge, #13149, is described in the following section. In this upper single null discharge, #13149, the neutral beam injection starts already very early in the current ramp up phase at t = 0.3s with one NBI source, $P_{NBI,Q3} = 2.5$MW. Later two more NBI sources are used with then a total power of $P_{NBI} = 7.5$MW. In Fig. 4.7, the time traces of the NBI power, P_{NBI} (in b), blue), the plasma current with the ramp-up phase (in a), black) are shown. This plot shows also H_{98} (in a), red), the confinement enhancement factor as given by the ITER scaling law [44], the Greenwald fraction n/n_{GW} (in a), blue) [4] and the electron temperature measurements c). This early NBI heating into the current ramp-up phase produces an ion ITB which starts at t $\approx$ 0.5s ($T_{i,max} \approx$ 10keV), and develops further at t $\approx$ 0.95s ($T_{i,max} \approx$ 15keV). This can be seen in 4.7 d) which shows the time traces of the ion temperature measurements (different colors signal different radial position of the measurement). The degradation of

[4] Greenwald density limit $\bar{n}[10^{20}/m^3] < n_{GW}[10^{20}/m^3] = I_{Pl}[MA]/\pi a^2[m]$

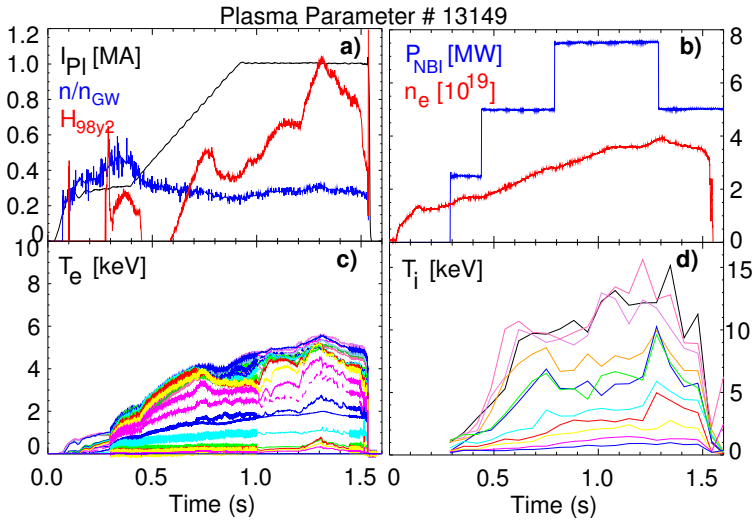

Figure 4.7: Overview of plasma parameters. Plasma current I_{Pl}, the Greenwald fraction n/n_{GW}, the confinement factor H_{98} in a); neutral beam power P_{NBI}, averaged electron density $\bar{n}_e$ in b); time traces of T_e (from ECE) in c) and of T_i (from CXRS) in d).

the ITB, starts at about t $\approx$ 1.4s. The discharge ends at t $\approx$ 1.6s with a disruption, a sudden loss of thermal energy due to MHD instabilities which terminates the discharge.

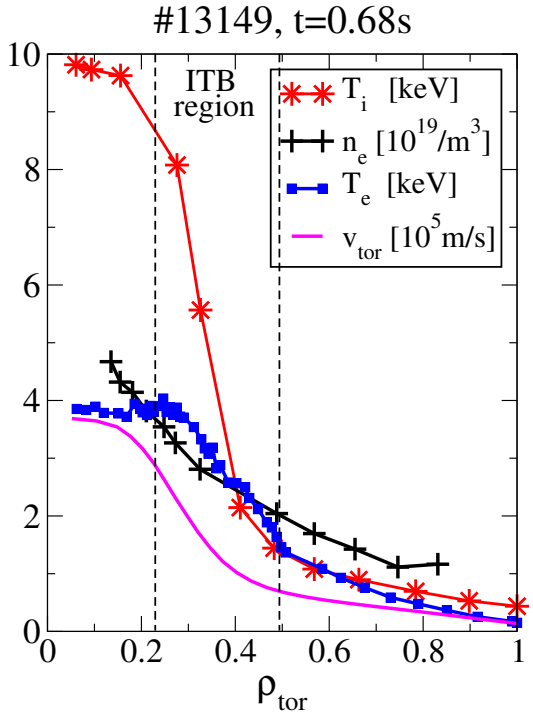

Figure 4.8: Profiles of T_i (CXRS), T_e (ECE) and n_e (Thomson Scattering) of #13149 at t=0.68s during the first ITB phase.

In Fig. 4.8 the profiles (plotted against the normalized toroidal flux coordinate, ρ_{tor}) of the ion temperature, T_i from CXRS diagnostic (red), the electron temperature, T_e (blue) from Electron Cyclotron Emission (ECE) diagnostic, the electron density, n_e (black) from Thomson scattering diagnostic, and the toroidal velocity, v_{tor} (magenta) from CXRS, at $t = 0.68$s during the first ITB phase are shown. The region of the ion ITB (region with the strongest gradient) is denoted by the dashed lines. Towards the center, the profiles of the temperatures are flat whereas the electron density is peaked. Unfortunately, the central region is not covered by measurements of the electron density (measured with Thomson scattering diagnostic) in this discharge and the gradient of the profile within the inner region of the ITB depends on the equilibrium reconstruction. The Thomson scattering diagnostic measures the electron density from the top of the vessel[5] and the signals are measurements at different z-position at a certain R-position. A mapping of the measured signals to the magnetic flux surfaces is needed to compare them with other measurements. If the elongation of the magnetic flux surfaces from the used equilibrium reconstruction is wrong, then the gradient of the electron density could shift outwards and might be more consistent with a flat density profile inside the 'current hole' region. These peaked density profiles inside the 'current hole' region can be one problem in the current diffusion simulations with ASTRA as described later. It can produce high bootstrap current inside the 'current hole' and can fill up the 'current hole'. Then the 'current hole' would not be maintained in the simulation.

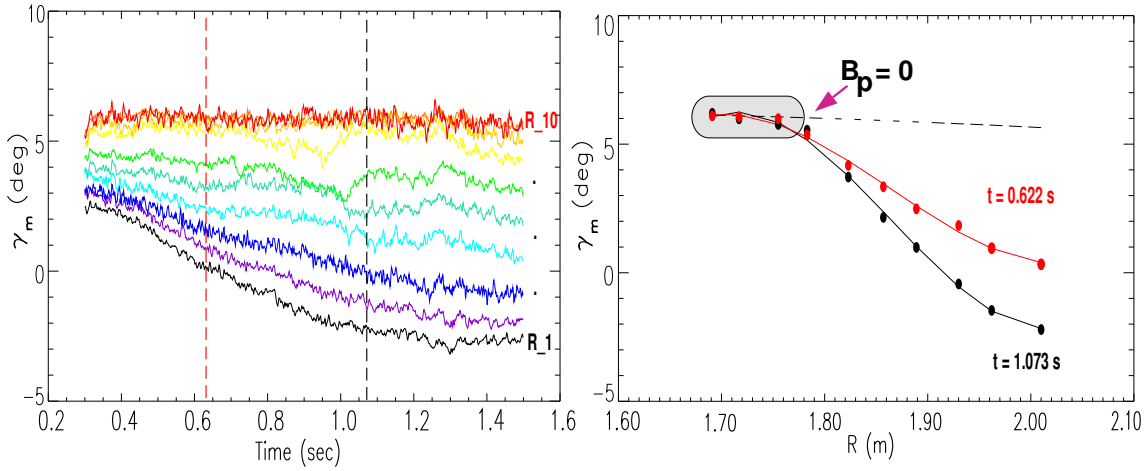

Figure 4.9: Time traces and profiles of γ_m for #13149. Channel 1 (black) outermost, channel 10 (red) innermost (near plasma center).

Fig. 4.9 shows the time traces of the ten channels of the MSE diagnostic. The innermost MSE channel (R_10) near the plasma center is shown in red, the outermost channel (R_1) is shown in black. Three to four of the central MSE channels (R_7,R_8-R_10) stay together at the value of $B_p = 0$ during $t = 0.3 - 1.3$s. This value of γ_m for $B_p = 0$

[5]The line of sight is only in z-direction

is directly computed from MSE geometry formula 3.1. This indicates an extended core region of at least 8-10 cm ($\approx 15\%$ of the minor radius) with nearly zero poloidal magnetic field, B_p and consequently nearly zero current density. During a (2,1)-DTM (Double Tearing Mode) at t= $0.72 - 1.0$s the value γ_m for channel R_7 (shown in yellow in Fig. 4.9) of the MSE diagnostic is seen to slowly decrease. This channel leaves the 'current hole' region due to the change in plasma energy and Shafranov shift caused by the DTM. After the DTM, γ_m of channel R_7 increases again towards the value $\gamma_m(B_p = 0)$, because the measurement position of this channel moves back into the 'current hole' region. The channel R_7 lies directly at the 'current hole' edge, as shown in Fig. 4.14 . Any small change of the plasma position moves this channel outside the 'current hole'. The diameter of the observation area per channel is about 2cm, the signal of each channel is averaged over this region. As seen in Fig. 4.10, the MSE channel R_7 follows the shift of the magnetic axis R_{mag}, after a previous shift of $\Delta R \approx 0.5$cm. The radially averaged signal is one possible explanation for the slowly changing signal of channel R_7, instead of a sudden change at a sharp 'current hole' edge (the sharp 'current hole' edge is shown from the equilibrium reconstruction at ASDEX Upgrade with NEMEC and at other experiments as JET and JT-60U). The time trace of H_{98} in Fig. 4.10 below, shows the confinement degradation caused by the (2,1)-DTM. Even though the magnetic axis is shifted inwards ($\approx$ 2cm), the innermost three channels are constant. This indicates that these inner channels lie in an extended region of a constant poloidal magnetic field $B_p = 0$ which cannot be explained by a calibration error. The calibration error of the inner MSE channels is systematically about $0.1° - 0.3°$ (i.e. the inner MSE values are systematically $0.1° - 0.3°$ to low. Also the noise (up to $0.4°$) of the inner channels is relatively high. This arises because of the low intensity of the inner MSE signals due to the neutral beam attenuation in the plasma.

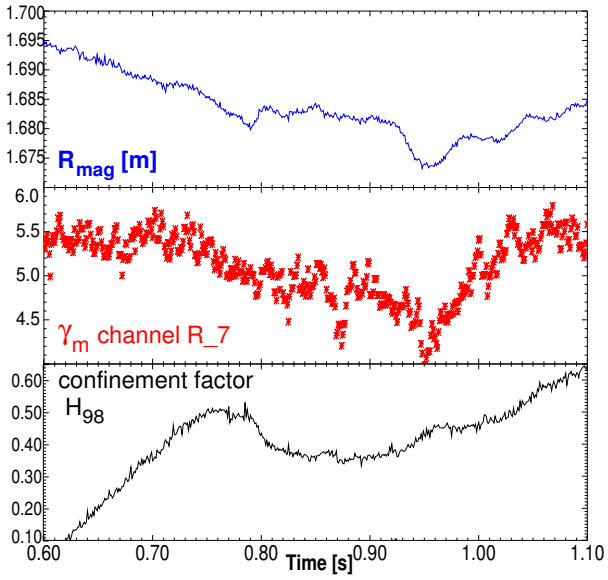

Figure 4.10: Time traces of the magnetic axis R_{mag}, the measured polarization angle γ_m of MSE channel R_7 and the normalized confinement factor H_{98}.

Later in the discharge, the 'current hole' degrades. First the MSE channel R_7 leaves the 'current hole' (at t≈ 1.29s), partially due to the shift of the plasma in R and z. At about t= 1.35s MSE channel R_8 also shows a decrease of the polarization angle. The degradation of the 'current hole' starts approximately at the same time, when one of the three NBI sources is switched off (at about t= 1.285s). This correlation with the degradation is not fully understood yet. It is possibly a combination of two effects. On the one hand, the plasma is shifted in R and z. With only two NBI sources P_{NBI} = 5MW instead of three NBI sources P_{NBI} = 7.5MW, the Shafranov shift is changed and the plasma is moved inwards. On the other hand, the width of the 'current hole' is reduced due to current diffusion towards the plasma center. This current diffusion could be amplified by a decreasing bootstrap current. The switching off of one NBI source possibly reduces the bootstrap current at the edge of the 'current hole', which is thought to be the mechanism maintaining the 'current hole'. In Fig. 4.11-4.13 the evolution of the temperature and density profiles between t= 1.1 − 1.4s is shown. The steepest gradients of the profiles moves outwards with time. Consequently the peak of the bootstrap current density moves also outwards. This could cause a drop of the bootstrap current, if the region of the gradients leave the 'current hole' edge region with low poloidal magnetic field.

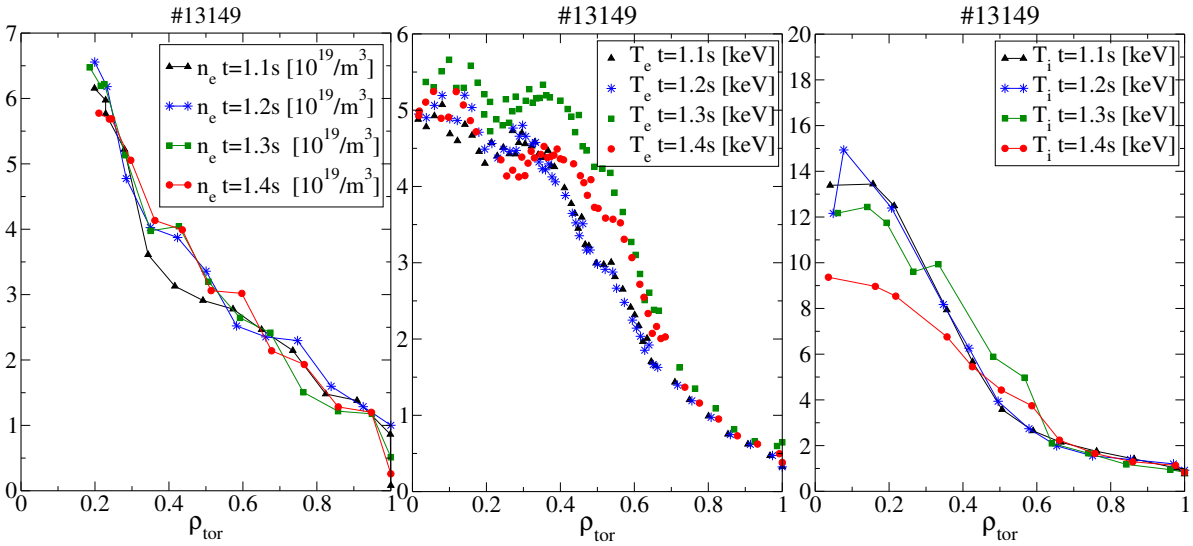

Figure 4.11: Profiles of n_e. Figure 4.12: Profiles of T_e. Figure 4.13: Profiles of T_i.

In the experimental campaign of 2003 at ASDEX Upgrade, it was attempted to re-establish the 'current hole' scenario of #13149 from experimental campaign of 2000. However in the meantime, with further changes in and outside the vessel also the start-up phase of the discharge has been changed. These changes in the start-up phase of the plasma, e.g. transformer current, gas pressure, coil currents, has meant that the 'current hole' scenario of #13149 could not be reproduced. It seems that the development of the 'current hole' depends strongly on this early phase of the plasma production. This will be studied in further detail in the experimental campaign of 2004.

4.2.2 Equilibrium Reconstruction

Using the new version of CLISTE [28] with the alternative coordinate ρ_{mid} and the weighted sum of the latest and previous solutions, it is possible to analyze the equilibrium of discharge #13149 with nearly zero current density in the center (high q_0). In this equilibrium reconstruction, the MSE measurements are included with high weight because this is the only information about the magnetic configuration in the central region of the plasma. However, the occurrence of a 'current hole' in the CLISTE equilibria is very sensitive to the position of the knots and the curvature penalty at the knot positions of the spline fitting functions.

Fig. 4.15 shows the direct comparison of B_p/B_t from CLISTE equilibrium reconstruction and the simplified computation of B_p/B_t from the measured polarization angle γ_m at two different time points using the MSE geometry formula 3.1 (A_n are the geometry factors):

$$\frac{B_p}{B_t} \approx \frac{\tan\gamma_m \cdot A_6 - A_2}{A_3 - \tan\gamma_m \cdot A_7} \tag{4.1}$$

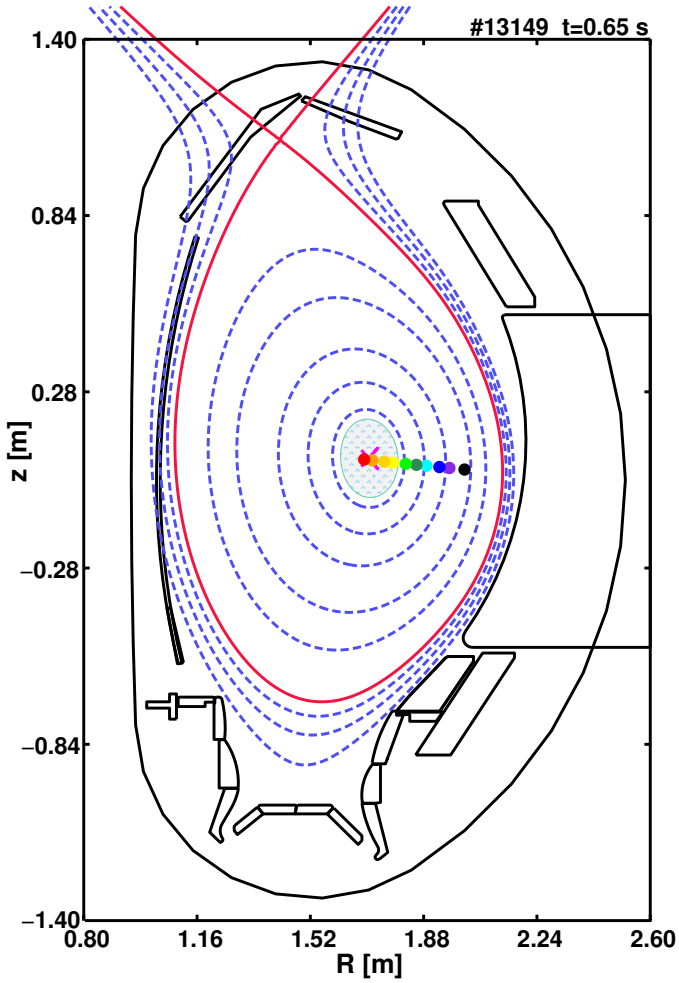

Figure 4.14: Position of the observations points of the MSE diagnostic in case of the current hole equilibrium of CLISTE.

For the computation of B_p/B_t directly from MSE measurements, $\boldsymbol{E_r}$ was neglected and it was assumed that $B_p \approx B_z$ at the MSE positions because the MSE measurement positions lie approximately in the magnetic midplane in this discharge at t= $0.65s$ as seen in Fig. 4.14 and only slightly below at t= $1.27s$. For this computation, the magnetic configuration (B_z, B_t) of the CLISTE equilibrium reconstruction at the measurement positions of the MSE was used.

Within the error bars ($0.2° - 0.3°$) of γ_m (using only the measurement errors), there is good agreement between CLISTE and MSE values. But the inner 3-4 channels show the systematically calibration offset of $\delta\gamma_m = 0.1° - 0.3°$ and a scattering of up to $\delta\gamma_m = 0.4°$ (comparing the B_p/B_t calculations at t= $0.65s$ and t= $1.27s$ in 4.15). The inner 3-4 channels should show a flat region with a constant B_p. As described before, during the time evolution of the discharge with the plasma shift, the inner 3-4 channels stay in a constant B_p region, this can only be $B_p = 0$. The computed B_p/B_t from MSE

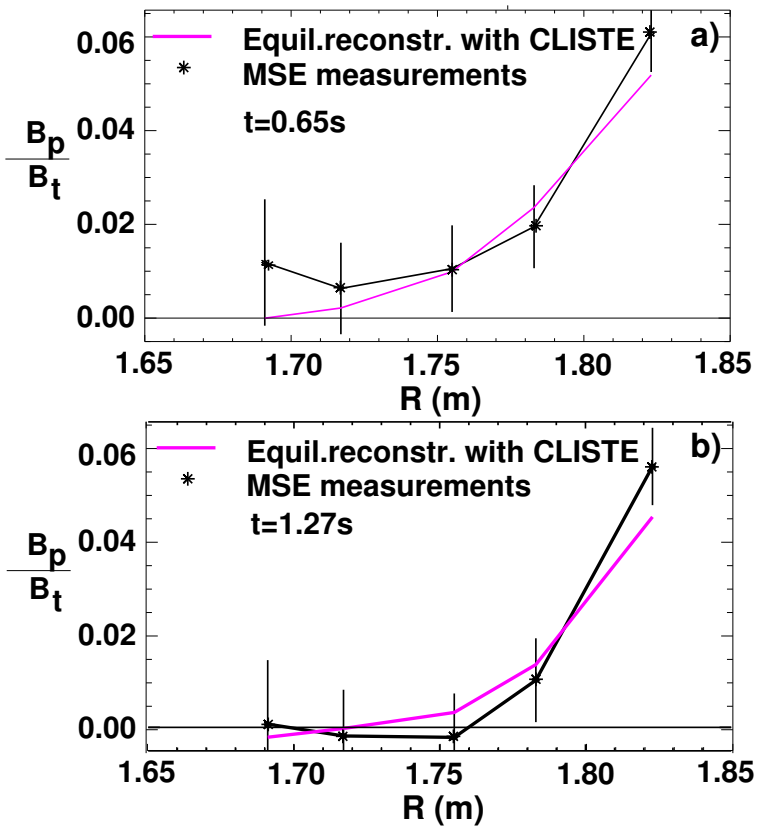

Figure 4.15: B_p/B_t from CLISTE compared with B_p/B_t computed from γ_m at a) t= 0.65s, b) t= 1.27s; (assumptions $B_p \approx B_z$, E_r negligible), error bars by error propagation with γ_m measurement errors.

channel R_10, the innermost one, shows a slightly larger disagreement, due to a larger calibration error and the large noise of this channel.

For a more exact calculation of error bars in q using the experimental MSE measurements, a different Ansatz is taken. An 'experimental' q value is obtained by scaling the poloidal magnetic field B_p, resulting from CLISTE, with a scaling factor f_{sc}. The scaling factor f_{sc} is chosen as such that the $\tan\gamma$ computed with the geometry formula 3.1 (using the vector components B_R, B_z of B_p from CLISTE) agrees with the measured $\tan\gamma_m$. This Ansatz assumes that the topology of the flux surfaces is not affected by the change in the poloidal magnetic field (not valid for the inner MSE channels) and the toroidal magnetic flux Φ is conserved. The equation for q is then:

$$q = \frac{\nabla\Phi}{RB_p} \tag{4.2}$$

This Ansatz results in a simple scaling $q \propto 1/B_p$. An 'experimental' q_{exp} (from MSE

measurements) is then computed using the scaling factor f_{sc}:

$$q_{exp} = q_{CLISTE}/f_{sc} \tag{4.3}$$

where q_{CLISTE} is the q value at the MSE position from the CLISTE equilibrium reconstruction. This method is also applied to compute a maximum and minimum q_{exp} (as the error bars of q_{exp}) using the MSE errors and scaling of the poloidal magnetic field between $\tan\gamma$ and $\tan(\gamma_m \pm \delta\gamma_m)$. The computed q_{exp} and the error bars for the inner channels are a rough estimate, because the Ansatz is not valid.

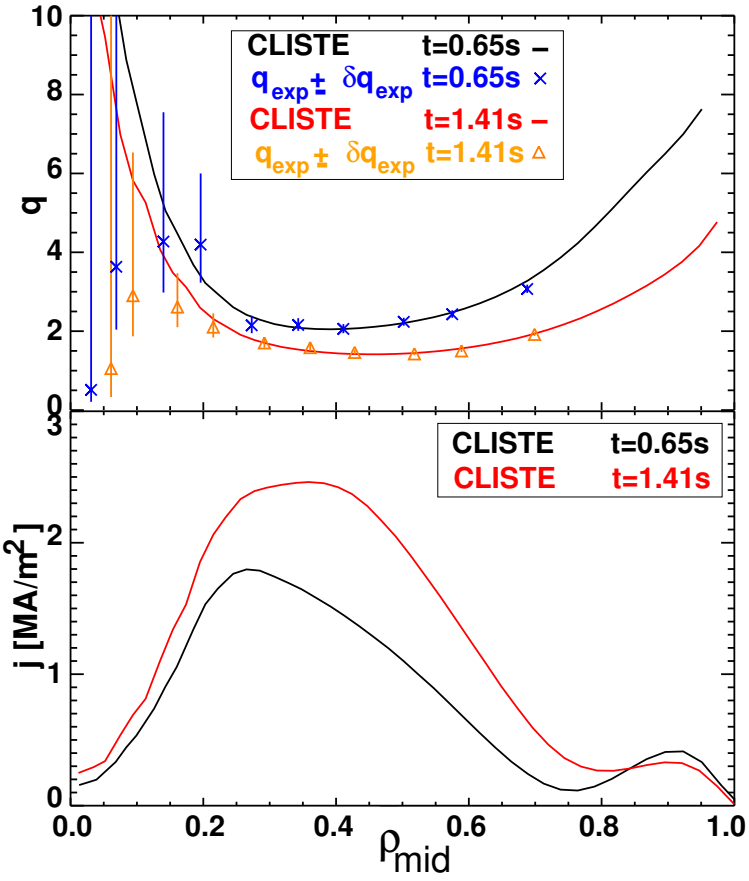

Figure 4.16: q profile and current density from CLISTE at t= 0.65s (black) and t= 1.41s (red) with the 'experimental' q values.

Fig. 4.16 shows the q profiles of the CLISTE equilibrium reconstruction and the 'experimental' q values at two different time points during the discharge #13149. The error bars of the inner channels are even larger in reality due to the large dependence of the inner channels on the flux surface topology. However, at the MSE locations more towards the edge, the flux surface topology is more robust and the 'experimental' q and their error bars are more reliable. Nevertheless, most 'experimental' q values at the MSE positions

agree with CLISTE q profile within the error bars.
Fig. 4.16 also illustrates the degradation of the 'current hole' at the later time point (t= 1.41s). The 'current hole' at this later time point is slightly narrower compared to t= 0.65s.

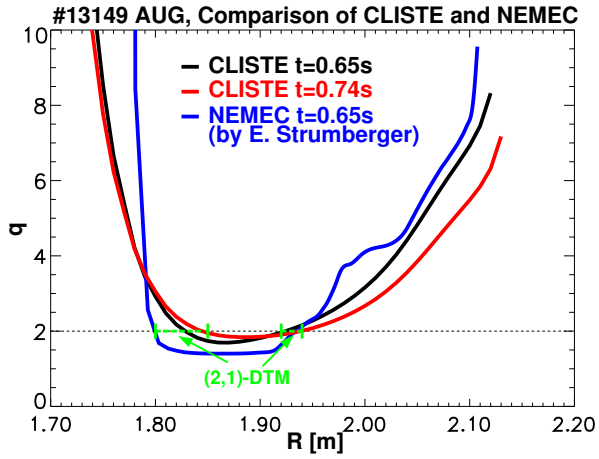

Figure 4.17: Comparison of q profiles from CLISTE and NEMEC together with the position of the (2,1)-DTM (green) at t= 0.72s from Soft X-ray and ECE diagnostic.

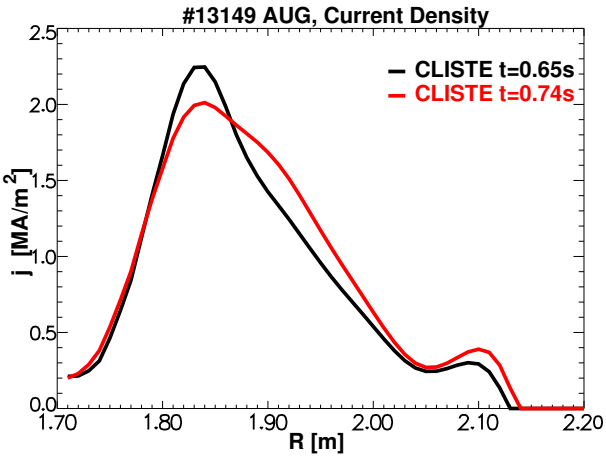

Figure 4.18: Current density from CLISTE.

Knowing the difficulties of reconstructing a 'current hole' equilibrium, the axisymmetric version of the three-dimensional NEMEC code [29] was also used for this ASDEX Upgrade discharge #13149 [30]. As described in chapter 2.4, the code uses the toroidal magnetic flux coordinate instead of the poloidal magnetic flux coordinate as the main flux coordinate and the rotational transform $\iota = 1/q$ instead of the safety factor q. In analyzing 'current holes' this is beneficial as the poloidal flux inside the 'current hole' region becomes zero and the central q becomes infinite. The adjustments during the iterations of NEMEC have to be done manually. The equilibrium reconstruction with NEMEC was done only for one time point (t= 0.65s) of discharge #13149 [30] to compare it with the CLISTE equilibrium reconstruction results due to the non-automated iteration process. Fig. 4.17 shows the comparison of CLISTE and NEMEC q profiles plotted against major radius R. In this equilibrium reconstructions with NEMEC and CLISTE, the experimental pressure was used as additional constraint. In this case, the magnetic axis determined with NEMEC and CLISTE is in better agreement with the magnetic axis given by Soft X-ray diagnostic. The positions of the $q = 2$ of CLISTE and NEMEC are consistent with both the inner and the outer position of the (2,1)-DTM (from diagnostic) within the error bars even though the reconstructed equilibrium from NEMEC is 70ms before the occurrence of (2,1)-DTM. As seen from the equilibrium reconstruction with CLISTE at the later time point t= 0.74s in Fig. 4.17, the positions of the two $q = 2$ surfaces are not changed much. The positions of the two $q = 2$ of the (2,1)-DTM were determined from the Soft X-ray and the ECE (Electron Cyclotron Emission)

diagnostic [45]. The Soft X-ray diagnostic has only a radial resolution of about 3cm. The accuracy for the inner $q = 2$ surface of the DTM is about 5cm and about 2cm for the outer $q = 2$ surface of the DTM. Owing to the limited number of knots and a minimal possible penalty (for convergence) of the spline fitting functions, the edge of the 'current hole' computed with CLISTE is not as sharp as the NEMEC equilibrium reconstruction, Fig. 4.17. The equilibrium reconstruction with the actual CLISTE version can reach central q_0 values up to 20-50. As the NEMEC code does not need poloidal magnetic flux in the center, the central q_0 can reach high values ($q_0 > 1000$). In Fig. 4.18, the current density profiles of the equilibrium reconstructions with CLISTE are shown.

The computation of the current density profile with NEMEC code has not yet been implemented.

4.2.3 Current Diffusion Simulations

For the ASTRA simulation of the evolution of the flux surface averaged toroidal current density $\langle j \rangle$, the measured values of electron temperature T_e, ion temperature T_i, electron density n_e, plasma current and magnetic field were given as input. Neoclassical resistivity and the Sauter model for the bootstrap current [36] were used. Z_{eff} was assumed to be constant = 2.5 across the radial profile, which is a rough estimate. However, no Z_{eff} profile is available for the studied discharge #13149 and the line averaged Z_{eff} measurement gives values in the range $2.5 - 3.5$. An initial 'current hole' $1/q$ profile was taken as input for ASTRA from CLISTE calculations constrained by magnetic and MSE measurements at $t = 0.33$s. However, the equilibrium solver of ASTRA (solving the Grad-Shafranov equation) cannot handle the equilibrium of the discharge #13149 without problems. If the q_0 increase to values higher than 30, the equilibrium solver of ASTRA cannot solve the Grad-Shafranov equation any more. To extend the simulation over the possible development of a 'current hole', a maximum q_0 was allowed. Similar to a reconnection process, the q in the central region is reduced to an arbitrary value, (a $q = 20$ value inside this region was chosen), if the central q exceeds 30. This holds the central current density above a certain value. Fig. 4.19, 4.20, 4.21 show the evolution of the averaged current density $\langle j \rangle$ together with the evolution of the bootstrap current density j_{BS} of different ASTRA simulations. Also, the time development of the ohmic current density j_{OH} and the non-inductive current density fraction j_{NI}, consisting of the bootstrap current density and the NBI driven current density j_{NBI} ($j_{NI} = j_{BS} + j_{NBI}$), is shown. Fig. 4.25, 4.26 show the evolution of the central q_0 and the minimum q_{min} of the different ASTRA current diffusion simulations with $Z_{eff} = 2.5$. The large scattering of the q_0 values over 20 is the result of the procedure in ASTRA which reduces the $q > 30$ values to $q = 20$ to prevent the crash of the equilibrium solver.

The ASTRA simulation ($Z_{eff} = 2.5$) with the calculated NBI current density and the calculated bootstrap current density j_{BS} (from the Sauter model) shows no maintenance of the 'current hole'. The time evolution (t= $0.30 - 1.30$s) of the different current density contributions is shown in Fig. 4.19 in different colors. The central current

density develops towards zero only after t= 1.2s as seen in Fig. 4.19.

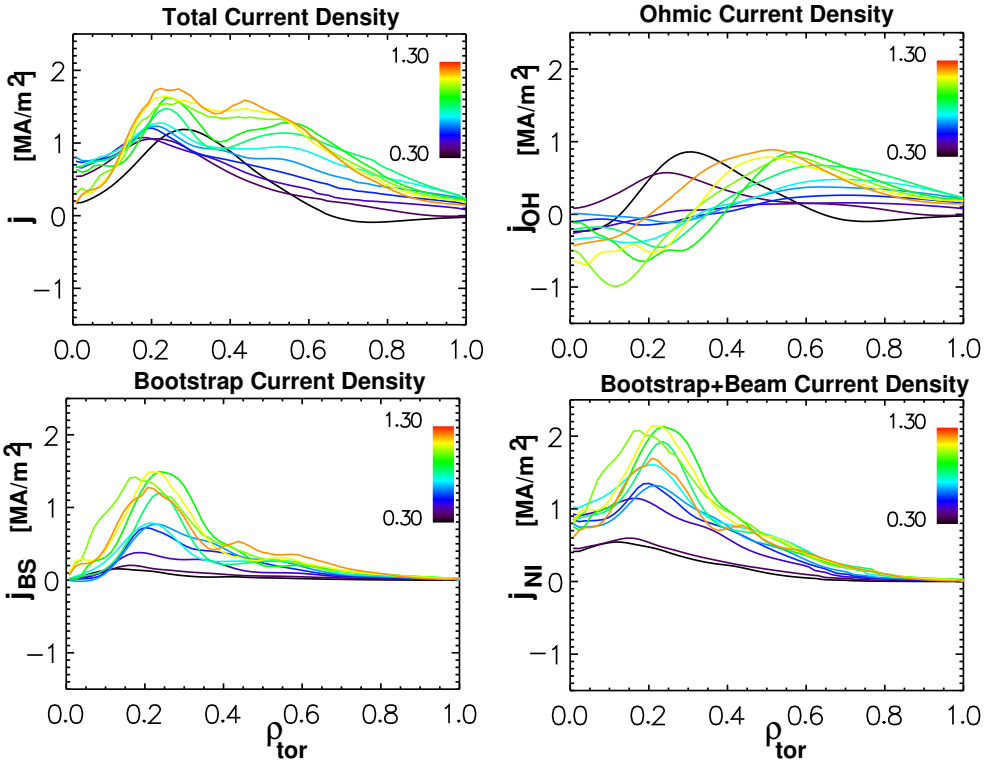

Figure 4.19: Evolution of the current densities $\langle j(\rho_{tor})\rangle$, j_{OH}, j_{BS} and $j_{NI} = j_{BS} + j_{NBI}$, different colors indicate different time points (t= 0.3 − 1.3s) of the ASTRA simulation with $Z_{eff} = 2.5$.

Since the ASTRA calculations using the experimental measurements and the theoretical models show no agreement with the experimental development of the current density, in the following sections different approaches are discussed to find the reason for the disagreement:

ASTRA simulation with $Z_{eff} = 1$, $j_{NI} = j_{BS} + j_{NBI}$

For the study of the Z_{eff} effect on resistivity and the different current fractions, the lowest limit for Z_{eff} was used. In this simulation, a constant $Z_{eff} = 1$ was used (which is not realistic) to compare it with the simulations with $Z_{eff} = 2.5$. In this simulation the 'current hole' was maintained. Only with $Z_{eff} = 1$, the off-axis bootstrap current density together with the off-axis peaked NBI current density is high enough to maintain the initial 'current hole' equilibrium (with $Z_{eff} = 1$ the NBI current density on-axis is very low). Furthermore in this simulation, the current diffusion time is about two times

longer (resistivity η is about one half, the current penetration time $\tau \propto 1/\eta \propto T_e^{\frac{3}{2}}$) than in the simulations with $Z_{eff} = 2.5$. However, the $Z_{eff} = 1$ simulation is not realistic and ASTRA calculations with $Z_{eff} = 1.5$ show again no agreement with the experimental current density development.

ASTRA simulation with $Z_{eff} = 2.5$, $j_{NI} = 2 \times j_{BS} + j_{NBI}$

Another possible explanation for the disagreement is that the calculated boostrap current is too small. In order to further investigate how much off-axis bootstrap current density is missing for the maintenance/development of the 'current hole', the bootstrap current density was artificially increased by a factor 2. The simulation is shown in Fig. 4.20. However even with twice the bootstrap current density, the 'current hole' cannot be maintained in the beginning. At about $t = 0.76s$, the non-inductive current density $j_{BS} + j_{NBI}$ exceeds the total current density in this simulation and the central current density decreases to zero. In this situation q_0 exceeds 30 and is reduced to 20. A narrow 'current hole' develops after t> 0.8s. The time trace of the central q_0 in this simulation is shown in Fig. 4.25 in green.

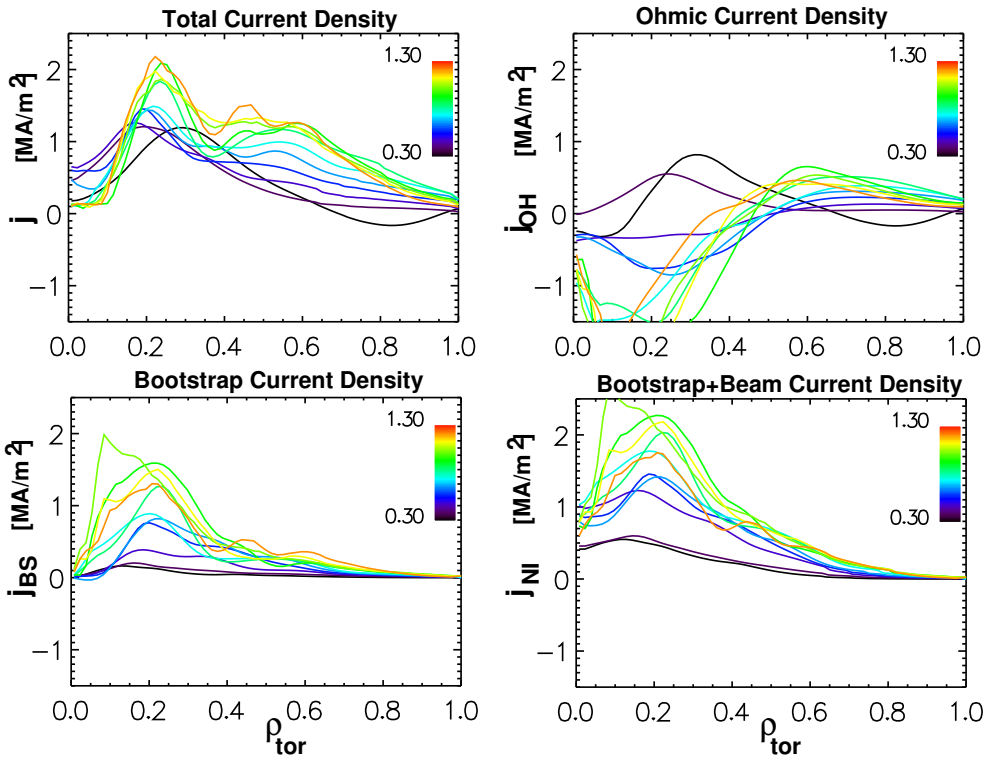

Figure 4.20: Evolution of $j(\rho_{tor})\rangle$, j_{OH}, j_{BS} and $j_{NI} = j_{BS} + j_{NBI}$, with twice bootstrap current density, $Z_{eff} = 2.5$.

ASTRA simulation with $Z_{eff} = 2.5$, $j_{NI} = 2 \times j_{BS}$

The NBI driven current density in the ASTRA simulations ($Z_{eff} = 2.5$) is high in the central region similar to the NBI power deposition profile shown in Fig. 4.22. This could fill up an existing 'current hole' region. However, comparing the different ASTRA simulations ($Z_{eff} = 2.5$) with and without driven current from NBI, the NBI driven current has little influence on the evolution of a 'current hole' in this discharge with the model used. Fig. 4.21 shows the time evolution of the current density fractions of an ASTRA simulation with twice the bootstrap current and without the NBI current density. The evolution of the 'current hole' is very similar to the evolution in Fig. 4.20 due to the effect that the decreased NBI current increases the ohmic part. Only a narrow 'current hole' region develops later in the simulation. The time trace of the q_0 value of this simulation is shown in orange in Fig. 4.25.

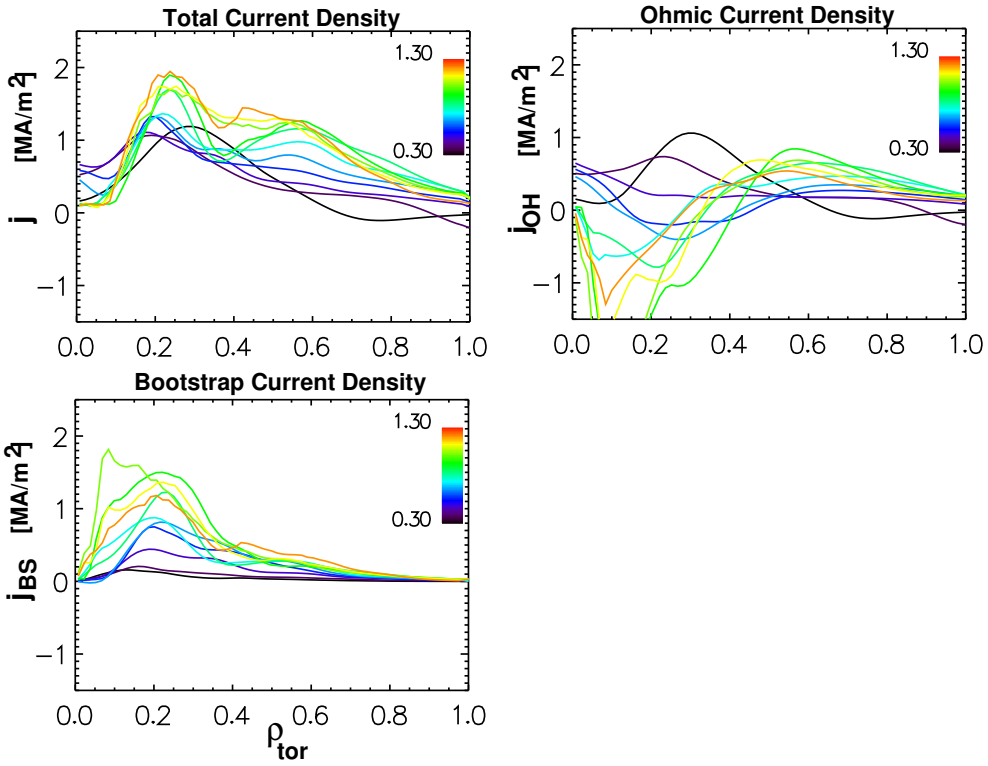

Figure 4.21: Evolution of $\langle j(\rho_{tor})\rangle$, j_{OH}, j_{BS}, with twice bootstrap current density and no NBI driven current.

ASTRA simulation with $Z_{eff} = 2.5$, $j_{NI} = 1 - 1.5 \times j_{BS} +$ off $-$ axis j_{NBI}

In a further simulation, it was attempted to produce more off-axis NBI current density to simulate an off-axis redistribution of the NBI current. For simplicity, the new geometry of the tangential NBI sources of the second beam box was used. The deposition of these

sources is more off-axis. For this simulation, the total NBI driven current was adjusted to the values of the previous ASTRA calculations with the real geometry of the NBI sources. The changed NBI current density profile in this simulation has a similar profile as the NBI power deposition shown in Fig 4.22. An off-axis NBI current density could be produced in the case of a 'current hole' equilibrium due to the zero poloidal magnetic field region. Therefore, the NBI particles have no confinement inside this 'current hole' region and different orbits, (see Fig. 4.2).
However, this simulation with the more off-axis NBI current density, shows also no maintenance of the 'current hole' and a 'current hole' develops later in the discharge (t> 0.76s) only with a factor 1.5 of the bootstrap current density. The time evolution of q_0 is shown in yellow in 4.25.

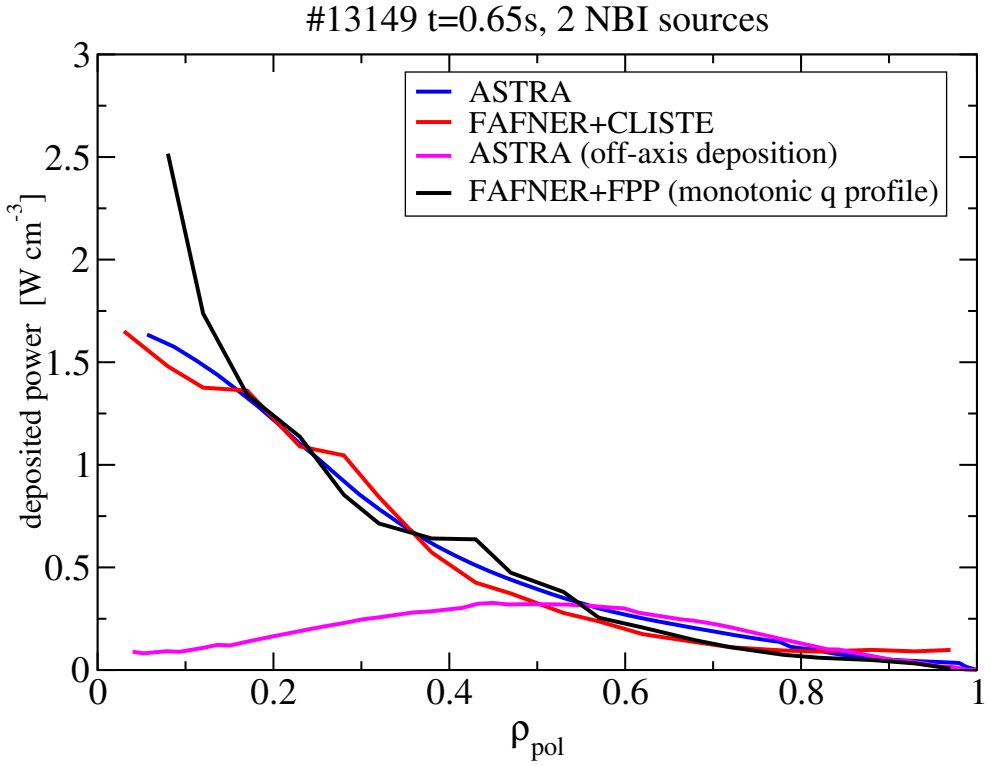

Figure 4.22: NBI power deposition profile computed with FAFNER using different equilibrium reconstructions compared with the ASTRA deposition profile at t= 0.65s

For the independent calculation of the NBI deposition, the FAFNER code [46], a fully 3D neutral beam injection using Monte Carlo method was used. As mentioned before, owing to a very small to zero poloidal magnetic field in the central region, the ions of the NBI could have different orbits than in conventional scenarios. But this assumption of a redistribution of the NBI particles is not proven by the orbit following Monte Carlo calculation of FAFNER [46] using the approximately 'current hole' equilibrium of CLISTE. The FAFNER code follows 15000 test particles in this

Monte Carlo calculations using the CLISTE magnetic configuration. However, the used CLISTE equilibrium has not a real extended zero B_p region and the calculations of FAFNER are only a approximation with a low central B_p region. The FAFNER calculations results in a power deposition profile which is very similar to the ASTRA calculated power deposition for two NBI sources at t= 0.65s 4.22 and for three NBI sources at t= 0.85s 4.23 of #13149.

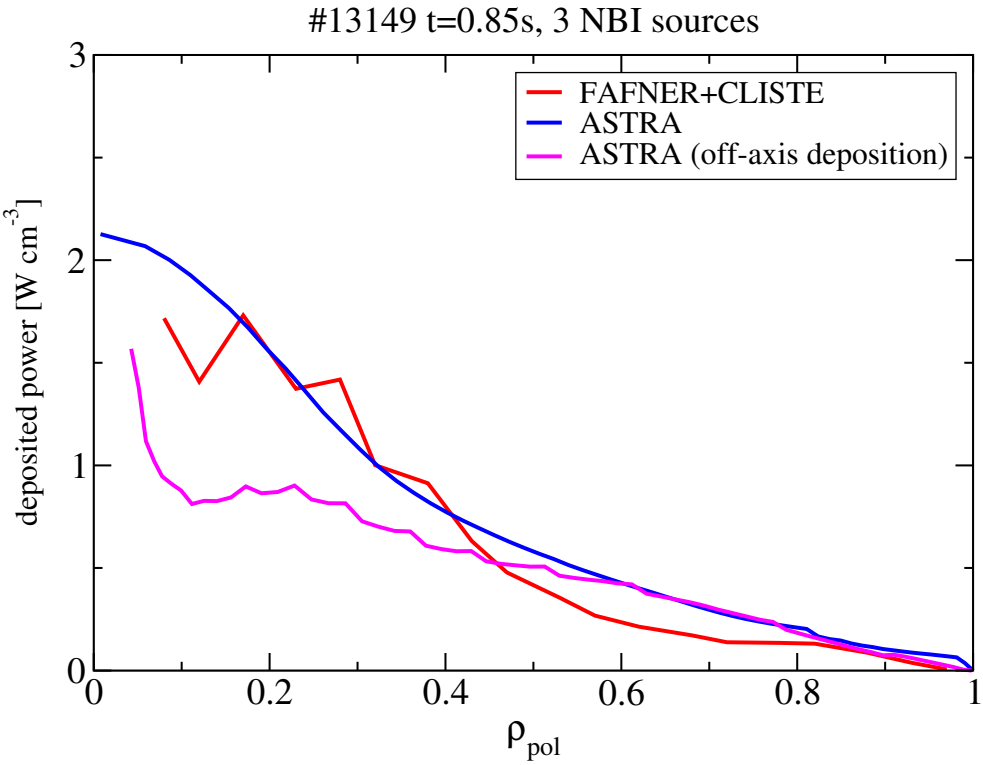

Figure 4.23: NBI power deposition profile computed with FAFNER using different equilibrium reconstructions compared with the ASTRA deposition profile at t= 0.85s

ASTRA simulation with $Z_{eff} = 2.5$, $j_{NI} = j_{BS} + j_{NBI} + j_{artificial}$

Another uncertainty is the large fast particle content which develops in this discharge. Up to one third of the thermal pressure is added by the fast particles. A possible additional non-inductive off-axis current could be produced by a fast particle bootstrap current. In the model used in these ASTRA simulations, the fast particles are not yet included in the calculation of the bootstrap current. For the calculation of a possible fast particle bootstrap current density, the distribution of the fast particles has to be calculated. Adding an artifical off-axis current density in the ASTRA simulation ($Z_{eff} = 2.5$), with the single bootstrap current and the normal NBI driven current, has shown that the initial 'current hole' equilibrium can be maintained. This could be a estimate how much off-axis fast particle bootstrap current would be necessary to maintain the 'current hole'.

In this simulation, a total artificial current of $I_{art} = 58kA$ per NBI source was chosen in form of a Gaussian profile off-axis at about $\rho_{tor} = 0.2$. The different current density fractions at a certain time point (t= 0.7s) are shown in Fig. 4.24. The assumption of the increasing artificial current with additional NBI power was used to simulate increasing fast particle content with each additional NBI source. This simulation with the artificial off-axis current shows a similar time evolution of q_{min} as the CLISTE q_{min} (purple in 4.26) and a high q_0 (purple in 4.25) for the first time.

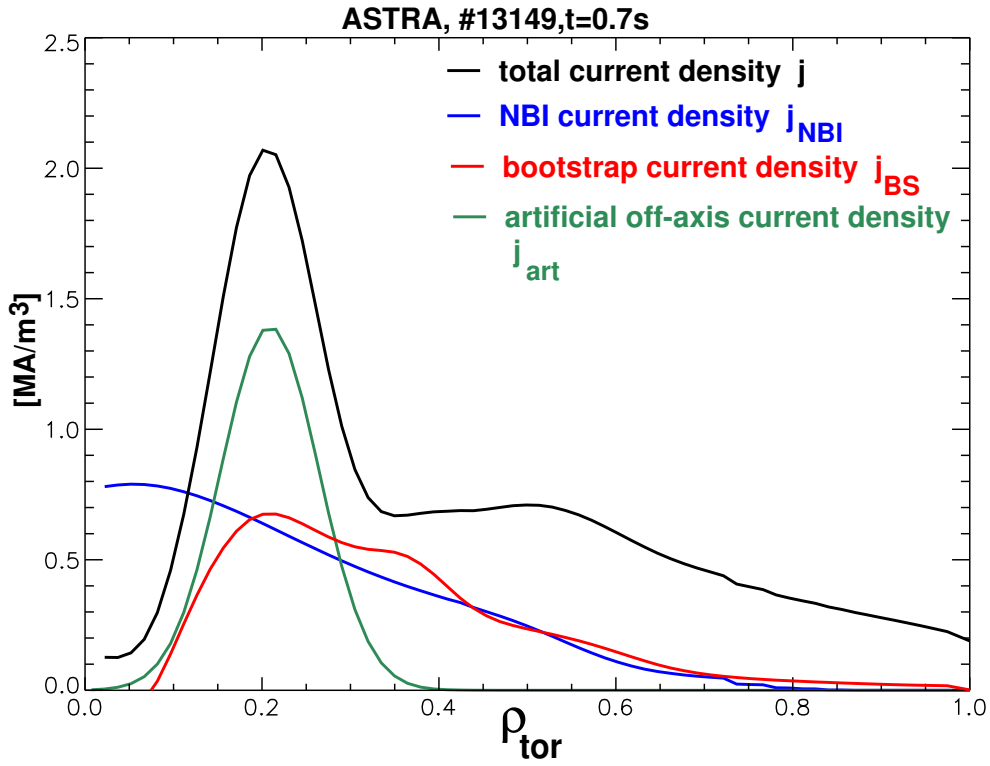

Figure 4.24: Current density fractions $\langle j(\rho_{tor})\rangle$, j_{BS}, j_{art} ($I_{art} = 117kA$) in #13149 at t= 0.7s with two NBI sources.

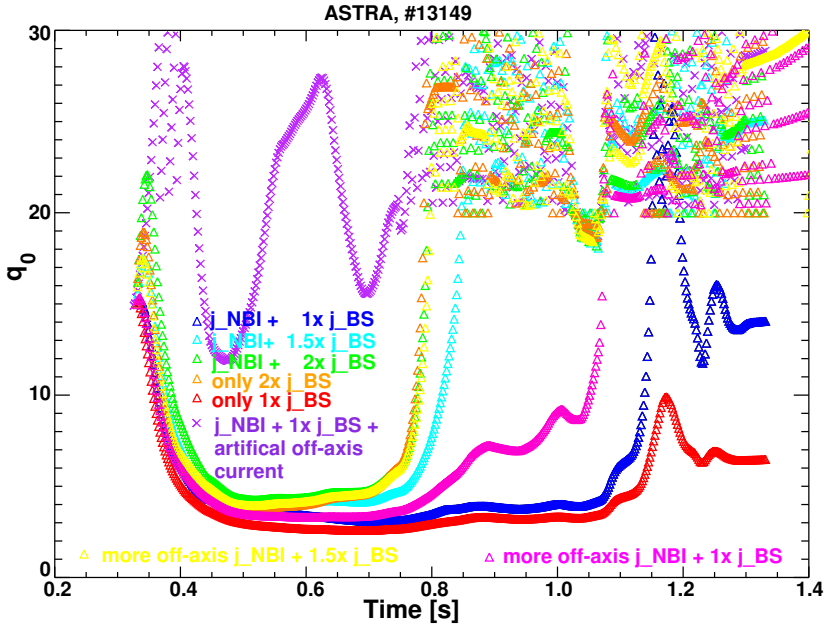

Figure 4.25: Time evolution of the q_0 value of the different ASTRA simulations with, without, more off-axis NBI driven current density and different factors of bootstrap current density.

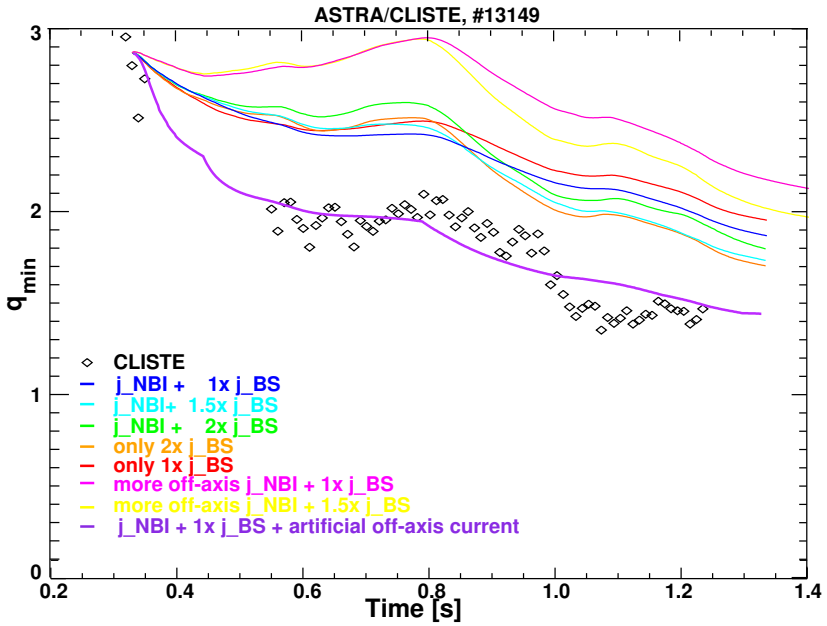

Figure 4.26: Time evolution of the q_{min} value of the different ASTRA simulations with, without, more off-axis NBI driven current density and $1-2\times$ bootstrap current density compared with the CLISTE $q_{min,CLISTE}$ values,(2,1)-DTM during t= $0.72-1.0$s .

Conclusions

In all the different ASTRA simulations with $Z_{eff} = 2.5$, starting at t= 0.33s (except the simulation with the artificial current), the initial 'current hole' equilibrium from CLISTE vanishes after about 70ms. In these simulations, not enough non-inductive off-axis current density from only the bootstrap current exists to maintain the 'current hole' in the simulation. This gives the suggestion that there is a non-inductive off-axis current missing (or less probably the mechanism for maintaining the 'current hole' in this phase is a different one). As described before, the uncertainty of the gradients of the profiles can be one reason for the insufficient bootstrap current to maintain the 'current hole' in the simulations with $Z_{eff} = 2.5$. The bootstrap current fraction in the beginning of the ASTRA simulation (at t$\approx$ 0.4s) is only about $15 - 20\%$ of the total plasma current. The initial $1/q$ profile of CLISTE is also only an approximation compared to the $1/q$ profile of a real 'current hole' with an extended region of $1/q \approx 0$ ($B_p \approx 0$) like in NEMEC. The equilibrium solver of ASTRA cannot handle such initial $1/q$ profile. However, for the calculation of the bootstrap current ($j_{BS} \propto \nabla p/B_p$) an extended region with $B_p \approx 0$ can change the results. The position of the pressure gradient slightly inside such an extended region with low poloidal magnetic field like the 'current hole' edge, can increase the local bootstrap current density by some factors. In the beginning of the $Z_{eff} = 2.5$ ASTRA simulations, the current diffusion is fast due to the low temperature ($T_e \approx 1 - 2$keV). The redistribution of the current in the beginning (of the simulations with vanishing 'current hole') from the maximum current density peak (q_{min} position) towards the center leads to a drop of q_0 in all these simulations in the first 70ms. For the same reason, the minimum q_{min} value shows a different time evolution compared with the CLISTE time evolution, shown in Fig. 4.26. In all these ASTRA simulations, q_{min} stays higher than the values of CLISTE (CLISTE $q_{min,CLISTE}$ agree with the existence of a (2,1)-DTM at t$\approx 0.72 - 1.0$s, $q_{min,CLISTE} < 2$ during the mode). Only the simulation with the artificial off-axis current shows a similar time evolution of q_{min} as the CLISTE q_{min}.
The NBI driven current density in the ASTRA simulations ($Z_{eff} = 2.5$) is high in the central region similar to the NBI power deposition profile shown in Fig. 4.22. This could fill up an existing 'current hole' region. However, comparing the different ASTRA simulations ($Z_{eff} = 2.5$) with and without driven current from NBI, the NBI driven current has little influence on the evolution of a 'current hole' in this discharge with the model used. For the independent calculation of the NBI deposition, the FAFNER code [46], a fully 3D neutral beam injection using Monte Carlo method, was used. Because of a very small to zero poloidal magnetic field in the central region, the ions of the NBI could have different orbits than in conventional scenarios. However, the assumption of a redistribution of the NBI particles is not proven by the orbit following Monte Carlo calculation of FAFNER using the approximately 'current hole' equilibrium of CLISTE. The FAFNER calculations results in a power deposition profile which is very similar to the ASTRA calculated power deposition.
Another uncertainty is the large fast particle content which develops in this discharge in

the ASTRA simulations. The fast particle content is very high in the ASTRA simulations. Adding the additional artificial off-axis current density in an ASTRA simulation ($Z_{eff} = 2.5$), has shown that the initial 'current hole' equilibrium can be maintained. This gives a estimation of the necessary off-axis current of a possible fast particle current.

Recapitulating, the evolution of the 'current hole' in all these ASTRA simulations is different from the time evolution of the 'current hole' deduced from γ_m. Further simulations are planned to clarify the reason for the discrepancies.

4.3 New 'Current Hole' Scenario with ECCD

In the experimental campaign 2003, a new 'current hole' scenario in ASDEX Upgrade comparable to the JET 'current hole' scenarios was developed. It uses counter [6] ECCD (Electron Cyclotron Current Drive) on-axis [7] or co ECCD off-axis in a lower single null discharge in ASDEX Upgrade as more effective and reliable way to produce 'current holes' similar to the effect of LHCD at JET. Fig. 4.27 shows this scenario of discharge #17542 with the time traces of some plasma parameters like the plasma current I_p, the power from the heating systems, the electron and ion temperatures at the central positions, the confinement enhancement factor H_{98}, the ELM activity [8] and the electron density n_e. In Fig. 4.28 the time traces of the electron and ion temperatures of #17542 are shown. In this discharge (#17542), the counter ECCD with two gyrotrons counter on-axis and one gyrotron co off-axis starts already at $t = 0.2s$, before the delayed current ramp up phase. The NBI begins later in the discharge at $t = 0.85s$ (compared to the NBI heated 'current hole' scenario).

After the beginning of NBI an electron ITB ($T_{e,max} \approx 9$keV) and an ion ITB ($T_{i,max} \approx 10$keV) develop for about 300ms and decay (at about $t = 1.15$s) well after the start of the regular ELM activity at $t = 0.99$s. The simultaneous electron and ion ITB reach about the same central temperature ($T_e \approx T_i$), Fig. 4.29. However, the electron ITB is narrower than the ion ITB which indicate a reversed q profile (reversed shear). In the present day knowledge, electron ITBs can only persist when the shear is negative. The reason for the decay of the simultaneous ion and electron ITBs is a mixture of the rising electron density n_e, MHD activity and maybe the stronger ELM activity after $t = 1.15$s. In Fig. 4.28, sawtooth-like crashes in T_e between $t = 0.55 - 0.85$s (collapsing electron ITBs) like in the JET 'current hole' discharges [39] are shown. Preliminary analysis shows sawtooth-like behavior without any (1,1)-MHD activity and low frequency (2,1)-MHD activity in the Soft X-ray and Mirnov measurements. The sawtooth-like behavior can be an indication to a mechanism to avoid negative central current density, like the reconnection events

[6] counter ECCD means current drive in the opposite direction of the plasma current, co current drive in the direction of the plasma current

[7] on-axis: at the position of the magnetic axis

[8] ELM (Edge Localized Mode) shown as spikes in the H_α signal during a H-mode.

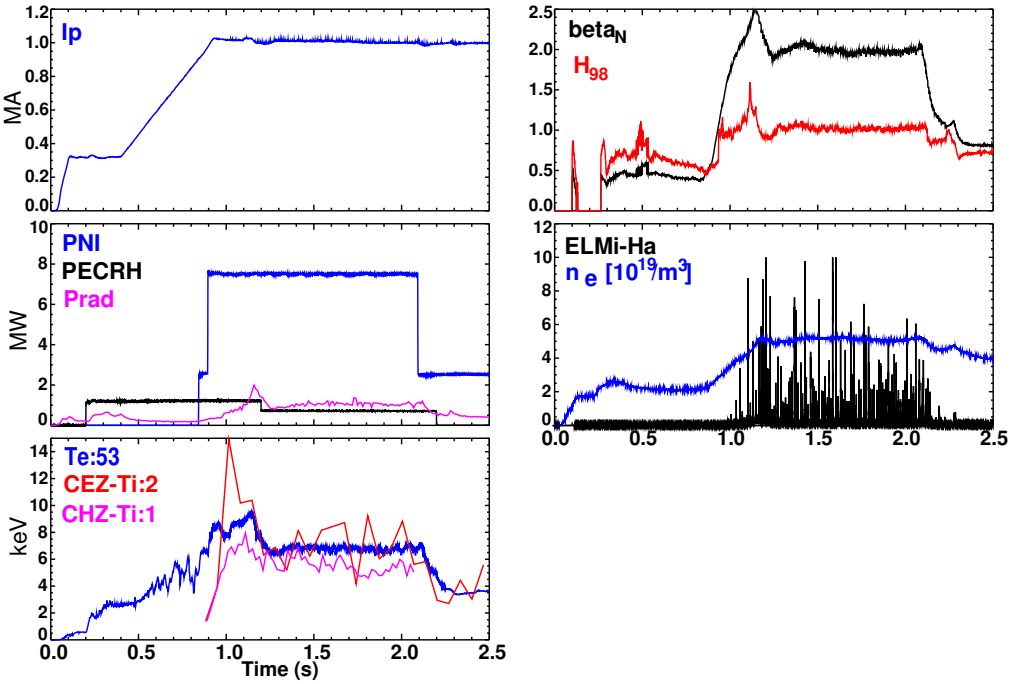

Figure 4.27: Overview of some plasma parameters of #17542.

described in [43]. According to the TORBEAM ECCD deposition calculation as seen in Fig. 4.30 and the ASTRA simulation, the on-axis counter driven current density from ECCD exceeds the total central current density by far. This leads to a negative central current density which cannot be handled by the equilibrium solver of ASTRA. For this ASTRA simulation, the reconnection procedure, as described before, was used again to reduce the central q_0 value to 20. One crash in the electron temperature is also shown in Fig. 4.29 which shows the T_e profile before and after the crash. Owing to the shift of the plasma during the discharge, the counter ECCD hits the center of the plasma only during $t = 0.55 - 0.85$s, the same time period as the sawtooth-like crashes in T_e.

The time development of the current density fractions of the ASTRA simulation, using the TORBEAM calculation for ECCD, is shown in Fig. 4.31. The ASTRA simulation shows a very narrow 'current hole' region according to the deposition width of the ECCD, calculated by TORBEAM. Also the temperature profiles show no flattening in the center consistent with a narrow 'current hole'. As shown in 4.30, the calculations with TORBEAM show a very narrow deposition width of only 2-3cm. Unfortunately the MSE measurements are not calibrated yet for this discharge #17542, so that an equilibrium reconstruction with CLISTE is not possible.

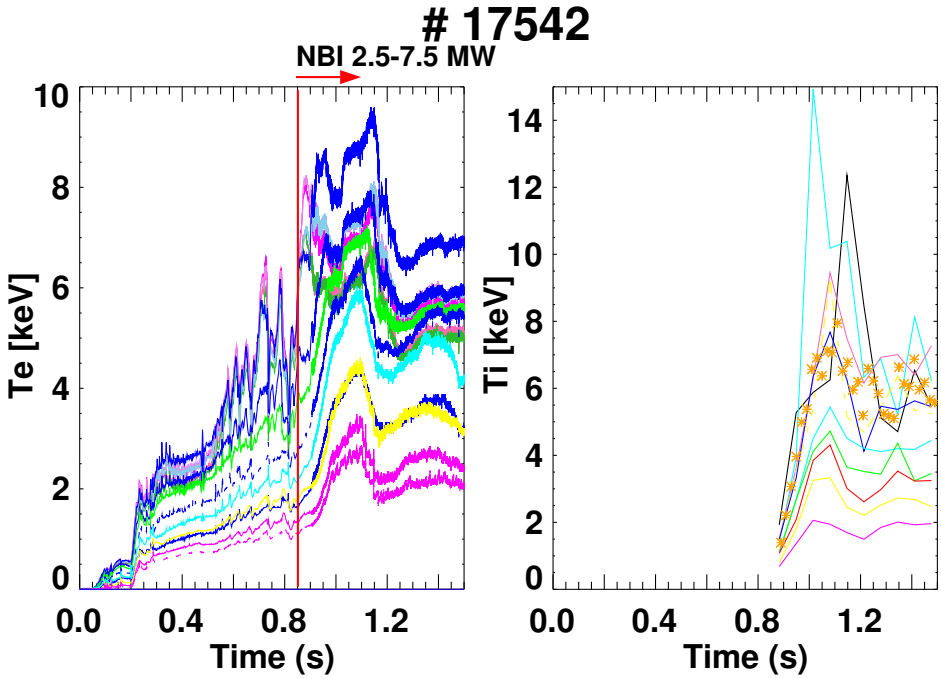

Figure 4.28: Time traces of T_e and T_i.

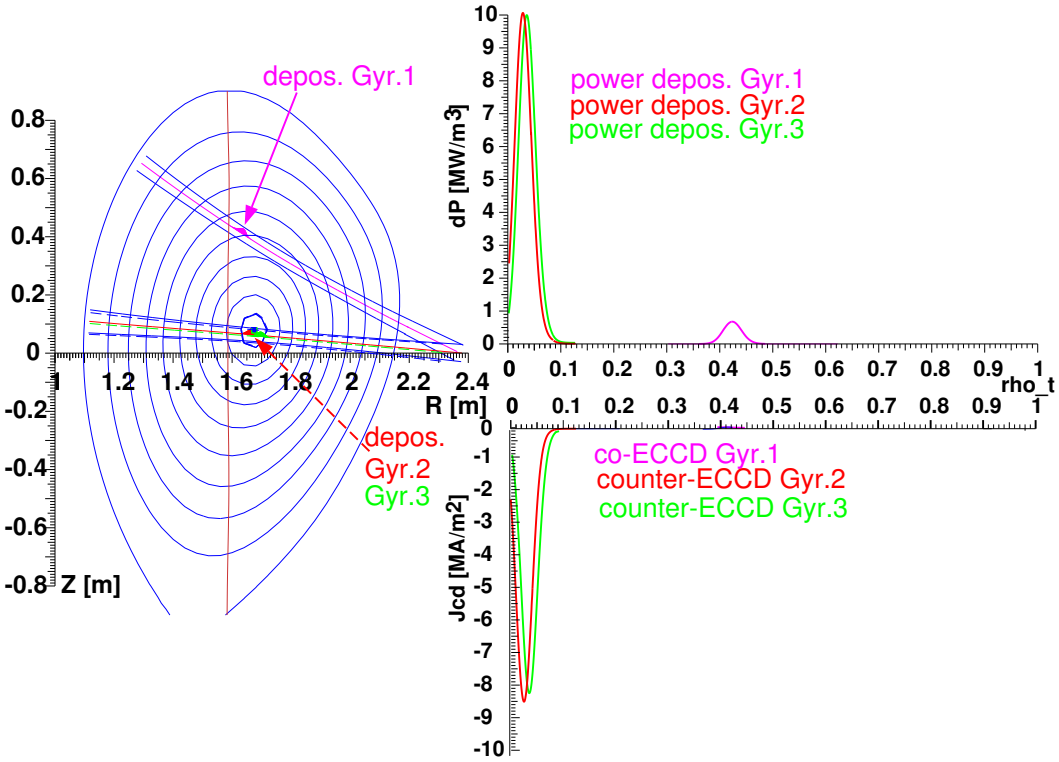

Figure 4.30: Power deposition and current drive profiles of 3 gyrotrons in discharge #17542 at t=0.65s computed with TORBEAM.

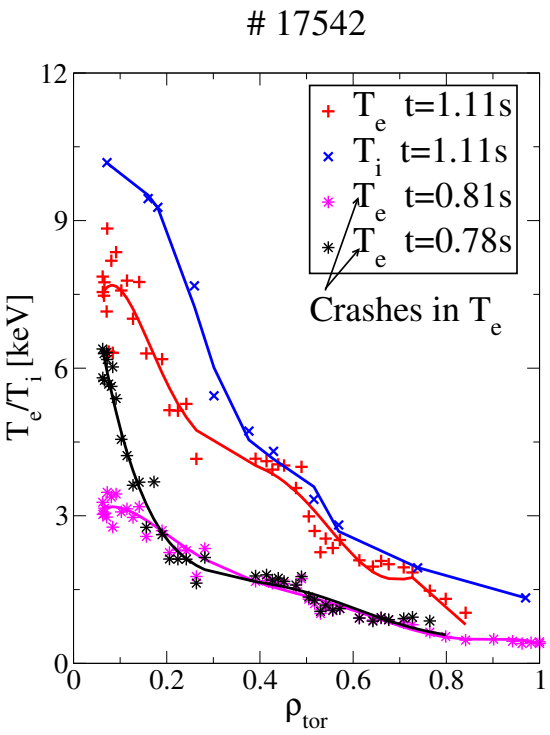

Figure 4.29: Profiles of T_e before and after a crash, profiles of T_e and T_i during an electron and ion ITB with $T_e \approx T_i$ at a later time.

However, if the radial extent of the 'current hole' region is only the counter ECCD deposition region as calculated by TORBEAM (2-3cm), then the 'current hole' region may not be seen by the MSE measurements with a radial resolution of only $\approx$ 3cm. But the 'current hole' region is maybe as large as the region of the sawtooth-like crash in T_e, which has a radial extension of about 0.15 in ρ_{tor} and about 10cm in major radius.

4.4 Summary

According to the MSE measurements in one of the studied 'current hole' discharges #13149, the 'current hole' already exists at $t \approx 0.33$s and decays after $t \approx 1.3$s. The measured polarization angle γ_m of the 3-4 inner MSE channel stay approximately at a constant value for B_p. Owing to the plasma shift during the discharge, the inner 3-4 MSE channel lie in a region with constant poloidal magnetic field B_p, which can be only $B_p = 0$. Calibration errors as reason for the behavior of the measured γ_m of the inner MSE channels are excluded. The 'current hole' diameter is about 15% of the minor radius (about 10cm) according to the equilibrium reconstruction and the MSE measurements. For the equilibrium reconstruction, the improved CLISTE code and the modified NEMEC code were used. The q profiles calculated with both codes show

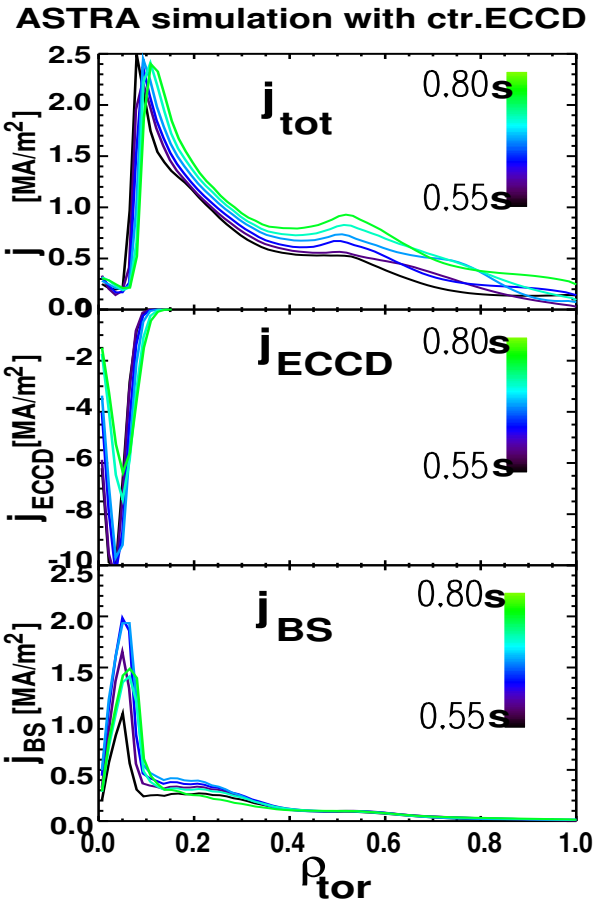

Figure 4.31: ASTRA simulation of the current density, with the total driven ECCD and the bootstrap current density of #17542. The scale of the ECCD current density is four times larger than in the other plots.

good agreement with the experimental determined position of the two $q = 2$ surfaces of a (2,1)-DTM at a certain time point. The significant difference of these equilibrium reconstructions of CLISTE and NEMEC is the sharp 'current hole' edge in the NEMEC q profile and the high q_0 values ($q_0 > 1000$) reachable with NEMEC.

The ASTRA current diffusion simulations with $Z_{eff} = 2.5$ show no maintenance of the initial 'current hole' equilibrium (except a simulation with artificial off-axis current). Contrary to the experimental results, in these ASTRA simulations ($Z_{eff} = 2.5$) only with artificially increased bootstrap current (by factor 2), the current density is decreased to zero in a very narrow central region late in the discharge (t> 0.76s). Only in an ASTRA simulation with $Z_{eff} = 1.0$ (which is not realistic), the 'current hole' could be maintained with the calculated bootstrap due to a longer current diffusion time and a larger bootstrap current (caused by $Z_{eff} = 1.0$). In the simulations with a development of a 'current hole' region, this region is much smaller than indicated by the MSE measurements. The equilibrium solver of ASTRA has severe problems to solve this extremely

reversed shear equilibria. The disagreement of the experimental results from MSE and the ASTRA simulations is a mixture of different effects. One possible explanation for the disagreement is a different resistivity in the experiment. Maybe the assumption of $Z_{eff} = 2.5$ is wrong or the evolution of the bootstrap current is much stronger and earlier. The probable inaccuracies in the profiles of temperatures and density and the only approximate 'current hole' equilibrium of CLISTE have also a strong influence on the calculation of the bootstrap current ($j_{BS} \propto \nabla p/B_p$) in the ASTRA simulations. Another uncertainty is the large fast particle content which develops in this discharge. Up to one third of the thermal pressure is added by the fast particles. In the model used in the ASTRA simulations, the fast particles are not yet included in the calculation of the bootstrap current. Adding an additional artifical off-axis current density in an ASTRA simulation ($Z_{eff} = 2.5$) has shown that the initial 'current hole' equilibrium can be maintained. This could be a estimation how much off-axis fast particle bootstrap current would be necessary to maintain the 'current hole'. Another possible explanation could be the difference in the NBI driven current. Because of a very small to zero poloidal magnetic field in the central region, the ions of the NBI should have different orbits than in conventional scenarios. This could cause a more off-axis peaked beam driven current density. This assumption has not been verified by the Monte Carlo calculation of FAFNER. The orbit following calculation of FAFNER, using the CLISTE equilibrium reconstruction, results in a power deposition profile which is very similar to the ASTRA calculated power deposition.
A new developed 'current hole' scenario with on-axis counter ECCD, similar to the 'current hole' scenario at JET with LHCD, shows sawtooth-like crashes in the electron temperature. These crashes could be a mechanism to prevent the central current density from becoming negative, similar to a reconnection process. The ASTRA current diffusion simulations show the existence of a 'current hole' in the deposition region (calculated with TORBEAM) of the central counter ECCD. However, the region of the sawtooth-like crashes is larger as the TORBEAM predicted 'current hole' region. Further investigations of the counter ECCD scenario are planned. Improved tools like ASTRA with the new equilibrium solver, other transport simulation codes and an automated NEMEC code are needed for further investigations of 'current hole' discharges at ASDEX Upgrade.

Chapter 5

Summary

The Motional Stark Effect (MSE) diagnostic is the main diagnostic used in this thesis. It is the main tool in ASDEX Upgrade to determine the internal magnetic configuration and the current density of the plasma with equilibrium reconstruction. The MSE diagnostic measures the geometry dependent polarization angle γ_m which is, in ideal geometry, proportional to the magnetic field pitch angle $\gamma_p = \tan^{-1}(B_p/B_t)$. A new MSE data acquisition system has been designed with the aim of providing on-line measurement for the real-time control of the current density $j(r)$. Without using analog lock-in amplifiers in this system, a software solution was necessary to replace the analog lock-in process. The software method, developed within the scope of the thesis, uses a Fast Fourier Transformation (FFT) and identifies the ratio of the absolute amplitudes at the second harmonic of the PEM (Photo Elastic Modulator, the main component of the MSE diagnostic for analyzing the polarization) frequency in the frequency spectrum as the ratio of the components of the linear polarized light of the beam emission.
Owing to the discovery of certain structures in the MSE measurements time-correlated with MagnetoHydroDynamic (MHD) activity, the sensitivity of the MSE diagnostic to magnetic perturbations (caused by MHD activity) was tested. The study of the variation of the calculated γ_m with a change of the local poloidal magnetic field (in a realistic dimension of a magnetic perturbation) has shown that this change could hardly be seen in the MSE measurements. The new data acquisition system with the FFT software program was used to test if a magnetic perturbation caused by an MHD mode could be seen directly in the frequency spectrum (from FFT program) of the MSE data. The frequency of the MHD mode in the test discharge was only seen marginally above the noise level in the FFT spectrum of the MSE.
On the other hand, a clear structure, time correlated with an MHD mode, in the MSE angles during an internal transport barrier (ITB) was observed. A strong radial electric field during the ITB in this discharge was excluded as a possible reason for the MSE structure. Therefore, this structure in the MSE measurements (time correlated with MHD mode, Double Tearing Mode (DTM) in this special case) can only be an effect of a change in the equilibrium caused by the mode. The structure in the MSE measurement reflects the region with constant q in the profile between the two $q = 2$ surfaces coupled

by the (2,1)-DTM.

Another feature found in the MSE data of this studied discharge is a so-called 'current hole'. The study of 'current holes' is important for predicting current profile evolution in next step facilities with high current diffusion time in scenarios with strong non-inductive current (such as bootstrap current). The 'current hole' plasmas are characterized by a core region with a very small or zero current density (zero poloidal field B_p within the error bars of the MSE diagnostic corresponding to very high central q, $q_0 \rightarrow \infty$). The 'current hole' can develop if an off-axis peaked non-inductive current density exceeds the total current density (i.e. the off-axis non-inductive current drive is strong enough relative to the ohmic current). The toroidal electric field E_{tor} (or loop voltage) becomes negative there. The decrease of the loop voltage diffuses towards the center and reduces the central current density. This diffusion can cause zero or even a negative toroidal current density in the center. The off-axis non-inductive current in the 'current hole' discharges with only NBI is thought to be the bootstrap current.
According to the MSE measurements in one of the studied 'current hole' discharges at ASDEX Upgrade , the 'current hole' already exists at the start of MSE measurements with the application of the first neutral beam source and decays slowly at the end of the discharge. The durability of the 'current hole' is much longer than predicted from the current diffusion simulations using the experimental profiles of temperature and density. The measured polarization angle γ_m of a few central MSE channels stay approximately at a constant value for B_p, which can be only $B_p = 0$. This is also true during a plasma shift, which excludes systematic calibration errors as reason for this behavior and supports a region with $B_p = 0$. The 'current hole' diameter is about 15% of the minor radius according to the equilibrium reconstruction. For the equilibrium reconstruction, the improved CLISTE code and the modified NEMEC code were used. The equilibrium reconstructions of both codes show good agreement with the experimental determined position of the two $q = 2$ surfaces of the (2,1)-DTM in this discharge at a certain time point. The significant difference of these equilibrium reconstructions of CLISTE and NEMEC is the sharp 'current hole' edge in the NEMEC q profile and the high q_0 values ($q_0 > 1000$) reachable with NEMEC.
Using ASTRA for the current diffusion simulations of the 'current hole' discharge, only in those simulations ($Z_{eff} = 2.5$ from line-averaged measurement, using the experimental profiles of temperature and density) with artificially increased bootstrap current, the central current density was decreased to zero in a very narrow region late in the discharge. The 'current hole' equilibrium in the beginning of the simulation was not maintained. The later developed 'current hole' region is much smaller than indicated by the MSE measurements. The disagreement of the experimental results from MSE and the ASTRA simulations can be explained by a mixture of different effects. A possible explanation for the disagreement is a different resistivity as used in the ASTRA model. The assumption of $Z_{eff} = 2.5$ could be wrong or the evolution of the bootstrap current could be much stronger and earlier. The probable inaccuracies in the profiles of temperatures and density and the only approximately 'current hole' equilibrium of CLISTE used as initial

equilibrium in the ASTRA simulation also have a strong influence on the calculation of the bootstrap current ($j_{BS} \propto \nabla p / B_p$) in the ASTRA simulations. A further uncertainty is the large fast particle content which develops in this discharge. Up to one third of the plasma pressure comes from the fast particles. In the model used in the ASTRA simulations, the fast particles are not yet included in the calculation of the bootstrap current. Adding an additional artificial off-axis current density in an ASTRA simulation ($Z_{eff} = 2.5$) has shown, that the initial 'current hole' equilibrium can be maintained. This could be a rough estimation how much off-axis fast particle bootstrap (or any other) current would be necessary to maintain the 'current hole'. Another possible explanation could be a different NBI driven current. This is not verified by the Monte Carlo calculation of the FAFNER code. The orbit following calculation of FAFNER, using the CLISTE equilibrium reconstruction, results in a power deposition profile which is very similar to the ASTRA calculated power deposition. Improved ASTRA simulations and simulations with other transport codes could give more insight.
A new developed 'current hole' scenario with on-axis counter ECCD, similar to the 'current hole' scenario at JET with LHCD, shows sawtooth-like crashes in the electron temperature. These crashes could be a mechanism to prevent the central current density from becoming negative, similar to a reconnection process. The ASTRA current diffusion simulations show the existence of a 'current hole' in the deposition region of the central counter ECCD. These discharges are an excellent target for further investigations.
Improved tools like ASTRA with the new equilibrium solver, other transport simulation codes and an automated NEMEC code can be used for further investigations of 'current hole' discharges.

Appendix A

The Tokamak ASDEX Upgrade

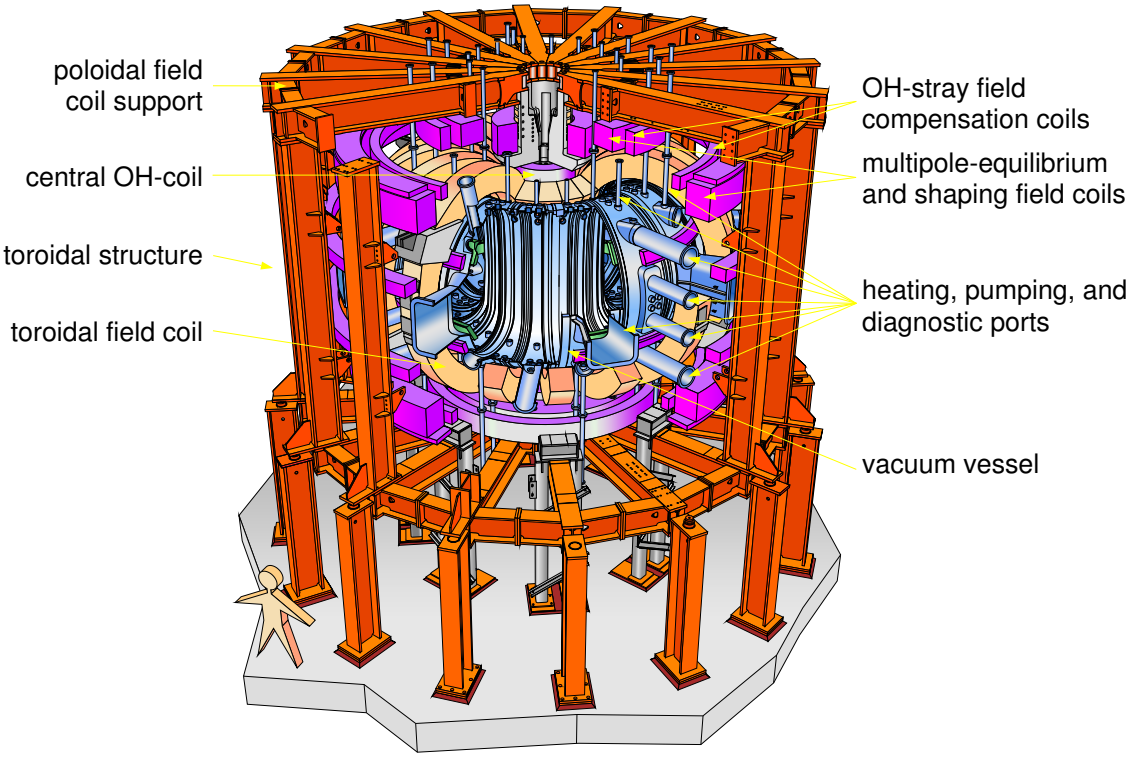

Figure A.1: Outline of the ASDEX Upgrade Tokamak

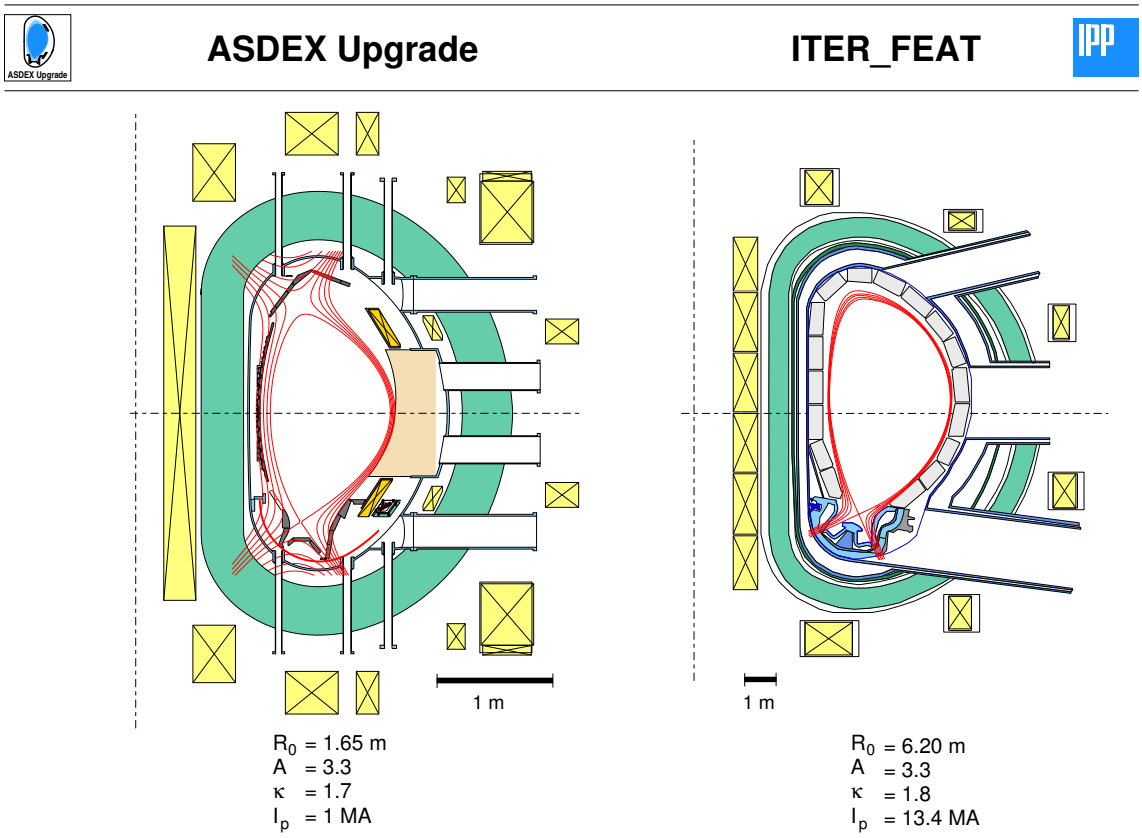

Figure A.2: Comparison of ASDEX Upgrade and the next step fusion device ITER.

Technical data:

Total height of the experiment	9 m
Total radius over all	5 m
Weight of the experiment	800 t
Material of the first wall	carbon
Number of toroidal field coils	16
Number of poloidal field coils	12
Maximum magnetic field	3.1 T
Plasma current	0.4 MA - 1.6 MA
Pulse duration	< 10 s
Time between pulses	15 - 20 min
Amount of data / pulse	approx. 0.5 GByte
Plasma heating:	up to 27 MW
Ohmical heating	1 MW
Neutral beam injection heating	20 MW
Injection energy	60 keV and 100 keV
Ion-Cyclotron heating	8 MW (30 MHz - 120 MHz)
Electron-Cyclotron heating	4 x 0.5 MW (140 GHz)

Table A.1: Technical data of ASDEX Upgrade

Typical plasma parameters:

Major plasma radius R_0	1.65 m
Minor horizontal plasma radius a	0.5 m
Minor vertical plasma radius b	0.8 m
Ellipticity b/a	1.8
Triangularity (top/bottom)	0.1 / 0.3, since 2000: 0.5 / 0.6
Plasma types	deuterium, hydrogen, helium
Plasma volume	14 m^3
Plasma mass	3 mg
Electrondensity	1 x 10^{20} m^{-3}
Plasma temperature	60 to 300 million degree

Table A.2: Typical plasma parameters of ASDEX Upgrade

Appendix B

Abbreviations

ASDEX	Axial Symmetric Divertor EXperiment
ASTRA	Automated System for TRansport Analysis in a Tokamak
AUG	ASDEX Upgrade
CXRS	Charge EXchange Recombination Spectroscopy
DTM	Double Tearing Mode
ECE	Electron Cyclotron Emission
ECRH	Electron Cyclotron Resonance Heating
ECCD	Electron Cyclotron Current Drive
ELM	Edge Localized Mode
FFT	Fast Fourier Transformation
ITB	Internal Transport Barrier
ITER	Internation Thermonuclear Experimental Reactor
JAERI	Japan Atomic Energy Research Institute
JET	Joint European Torus
JT-60U	JAERI Tokamak 60 Upgrade
LHCD	Lower Hybrid Current Drive
MHD	Magneto Hydro Dynamics
MSE	Motional Stark Effect
NBI	Neutral Beam Injection
NTM	Neoclassical Tearing Mode
PEM	Photo Elastic Modulator
SXR	Soft X-Ray

Bibliography

[1] Innovationsbeirat der Landesregierung von Baden-Württemberg und wissenschaftlich-technischer Beirat der bayerischen Staatsregierung. *Zukunft der Energieversorgung*. Springer, 2003.

[2] John Wesson. *Tokamaks, 2. edition*. Clarendon Press, Oxford, 1997.

[3] J. D. Lawson. Some criteria for a power producing thermonuclear reactor. *Proceedings of the Physical Society B*, pages 6–10, November 1956.

[4] F. Wagner, G. Becker, K. Behringer, D. Campbell, A. Eberhagen, W. Engelhardt, G. Fussmann, O. Gehre, G. Gernhardt, G. v. Gierke, G. Haas, F. Huang, M. Karger, M. Keihacker, O. Klüber, M. Kornherr, K. Lackner, G. Lissitano, G. G. Lister, H. M. Mayer, D. Meisel, E. R. Müller, H. Murmann, H. Niedermeyer, W. Poschenrieder, H. Rapp, H. Röhr, F. Schneider, G. Siller, E. Speth, A. Stäbler, K. H. Steuer, G. Venus, O. Vollmer, and Z. Yü. Regime of improved confinment and high beta in neutral-beam-heated divertor discharges of the ASDEX tokamak. *Phys. Rev. Lett.*, 49(19):1408, Nov. 1982.

[5] K. H. Burrel. Effects of ExB velocity shear and magnetic shear on turbulence and transport in magnetic confinement devices. *Phys. Plasmas*, 4(5):1499, May 1997.

[6] F. M. Levinton, M. C. Zarnstoff, S. H. Batha, M. Bell, R. E. Bell, R. V. Budny, C. Bush, Z. Chang, E. Fredrickson, A. Janos, J. Manickam, A. Ramsey, S. A. Sabbagh, G. L. Schmidt, E. J. Synakowski, and G. Taylor. Improved confinement with reversed magnetic shear in TFTR. *Phys. Rev. Lett.*, 75(24):4417–4420, December 1995.

[7] E. J. Strait, L. L. Lao, M. E. Mauel, B. W. Rice, T. S. Taylor, K. H. Burell, M. S. Chu, E. A. Lazarus, T. H. Osborne, S. J. Thompson, and A. D. Turnbull. enhanced confinement and stability in DIII-D discharges with reversed magnetic shear. *Phys. Rev. Lett.*, 75(24):4421–4424, December 1995.

[8] R. C. Wolf. Internal transport barriers in tokamak plasmas. *Plasma Phys. Contr. Fusion*, 45:R1–R91, Nov. 2002.

[9] H. Tamai and *et al.* Steady-state operation scenarios with a central current hole for JT-60SC. pages Vol.26B, P–1.050. 29th EPS Conference on Plasma Phys. and Contr. Fusion, Montreux, June 2002.

[10] G. Pereverzev, S. Günter, A. G. Peeters, and R. C. Wolf. Transport modelling of ASDEX Upgrade plasmas with internal transport barrier. *Europhysics Conference Abstracts (Proc. 27th Eur. Conf. Budapest 2000)*, 24B:1020–1023, 6 2000.

[11] D. R. Mikkelsen and C. E. Singer. Optimization of steady-state beam-driven tokamak reactors. *Nucl. Technol./Fusion*, 4:237–252, Sept. 1983.

[12] N. J. Fisch and A. H. Boozer. Creating a asymmetric plasma resistivity with waves. *Phys. Rev. Lett.*, 45(9):720, 1980.

[13] E. Poli, A. G. Peeters, and G. V. Pereverzev. Torbeam, a beam tracing code for electron-cyclotron waves in tokamak plasmas. *Comut. Phys. Commun.*, 136(1-2):90–104, 05 2001.

[14] R. P. Seraydarian, K. H. Burrell, and R. J. Groebner. Multichordal visible/near-uv spectroscopy on the DIII-D tokamak. *Rev. Sci. Instr.*, 59,(1530), 1988.

[15] A. Boileau, M. von Hellermann, W. Mandl, H. P. Summers, H. Weisen, and A. Zinoviev. Observations of motional stark features in the balmer spectrum of deuterium in the JET plasma. *J.Phys. B: At. Mol. Opt. Phys.*, 22(L145), 1989.

[16] F. M. Levinton, R. J. Fonck, G. M. Gammel, R. Kaita, H. W. Kugel, E. T. Powell, and D. W. Roberts. Magnetic field pitch-angle measurements in the PBX-M tokamak using the motional stark effect. *Phys. Rev. Lett.*, 63(19):2060–2063, November 1989.

[17] D. Wróblewski, K. H. Burell, L. L. Lao, P. Polizer, and W. P. West. Motional Stark effect polarimetry for a current profile diagnostic in DIII-D. *Rev. Sci. Instrum.*, 61(11):3552–3556, November 1990.

[18] R.C. Wolf, C. Challis, M. von Hellermann, R. König, W. Mandl, J. O'Rourke, and W. Zwingmann. pages Part IV, 229. Proc. 18th Eur. Conf. on Controlled Fusion and Plasma Physics, Berlin, 1991.

[19] D. Wróblewski and L. L. Lao. Determination of the safety factor in sawtoothing discharges in DIII-D. *Phys. Fluids B*, 3(10):2877–2881, October 1991.

[20] F. M. Levinton. The multichannel motional Stark effect diagnostic on TFTR. *Rev. Sci. Instrum.*, 63(10):5157–5160, October 1992.

[21] W. Mandl, R. C. Wolf, M. G. von Hellermann, and H. P. Summers. Beam emission spectroscopy as a comprehensive plasma diagnostic tool. *Plasma Phys. Contr. Fusion*, 35:1373–1394, 1993.

[22] R. C. Wolf, J. O'Rourke, A. W. Edwards, and M. von Hellermann. Comparison of poloidal field measurements on JET. *Nuclear Fusion*, 33(663), 1993.

[23] D. Wróblewski and L. L. Lao. Polarimetry of motional Stark effect and determination of current profiles in DIII-D. *Rev. Sci. Instrum.*, 63(10):5140–5147, October 1992.

[24] H. A. Bethe and E. E. Salpeter. *Quantum Mechanics of One- and Two-Electron Atoms*. Springer-Verlag, Berlin, 1957.

[25] J. P. Freidberg. *Ideal Magnetohydrodynamics*. Plenum Press, 1987.

[26] H. Grad. In *Proceedings of the Second United Nations Conference on the Peaceful uses of Atomic Energy*, page 190. United Nations, Geneva, 1958, Vol.21.

[27] V. D. Shafranov. *Sov. Phys. JETP*, 6(545), 1958.

[28] P. J. McCarthy, P. Martin, and W. Schneider. The CLISTE interpretive equilibrium code. IPP Report Nr. 5/85, Max-Planck-Institut für Plasmaphysik, May 1999.

[29] S. P. Hirshman, W. I. van Rij, and P. Merkel. Three-dimensional free boundary calculations using a spectral green's function method. *Comput. Phys. Commun.*, 43(1):143–155, December 1986.

[30] E. Strumberger, S. Günter, J. Hobirk, V. Igochine, D. Merkl, E. Schwarz, C. Tichmann, and the ASDEX Upgrade Team. Numerical investigations of axisymmetric equilibria with current hole. *Nuclear Fusion*, 44(3):464–472, 2004.

[31] G. Pereverzev and P. N. Yushmanov. Astra automated system for transport analysis in a tokamak. IPP Report Nr. 5/98, Max-Planck-Institut für Plasmaphysik, February 2002.

[32] A. Polevoi, H. Shirai, and T. Takizuka. Benchmarking of the NBI block in ASTRA code versus the OMFC calculations. *JAERI-Data/Code*, 97-014:1–14, March 1997.

[33] F. L. Hinton and R. D. Hazeltine. Theory of plasma transport in toroidal confinement systems. *Review of Modern Physics*, 48(2):239–308, April 1976.

[34] S. P. Hirshman, R. J. Hawryluk, and B. Birge. Neoclassic conductivity of a tokamak plasma. *Nuclear Fusion*, 17(3):611, March 1977.

[35] G. R. Harris. Comparisons of different bootstrap current expressions. Association EURATOM-C.E.A., Nov. 1991. DRFC/CAD EUR-CEA-FC-1436.

[36] O. Sauter, C. Angioni, and Y. R. Lin-Liu. Neoclassical conductivity and bootstrap current formulas for general axisymmetric equilibbria and arbitary collisionality regime. *Physics of Plasmas*, 6(7):2834–2839, July 1999.

[37] W. A. Houlberg, K. C. Shaing, S. P. Hirshman, and M. C. Zarnstorff. Bootstrap current and neoclassical transport in tokamacs of arbitary collisionality and aspect ratio. *Physics of Plasmas*, 4(9):3230–3242, September 1997.

[38] R. C. Wolf, P. J. Mc Carthy, F. Mast, and H. P. Zehrfeld. Motional stark effect polarimetry for the determination of the ASDEX Upgrade current density profile. *Europhysics Conference Abstracts (Proc. 24th Eur. Conf. Berchtesgaden 1997)*, 21A(IV):1509–1512, June 1997.

[39] N.C. Hawkes and *et al.* Observation of zero current density in the core of JET discharges with lower hybrid heating and current drive. *Phys. Rev. Lett.*, 87(11):115001, September 2001.

[40] J. A. Breslau, S. C. Jardin, and W. Park. Simulation studies of the role of reconnection in the "current hole" experiments in the joint european torus. *Physics of Plasmas*, 10(5):1665–1669, May 2003.

[41] T. Fujita and *et al.* Plasma equilibrium and confinement in a tokamak with nearly zero central current density in JT-60U. *Phys. Rev. Lett.*, 87(11):245001, December 2001.

[42] G. T. A. Huysmans, T. C. Hender, N. C. Hawkes, and X. Litaudon. MHD stability of advanced tokamak scenario with reversed central current: An explanation of the "current hole". *Phys. Rev. Lett.*, 87(24):245002–1, Dec. 2001.

[43] B. C. Stratton and *et al.* The role of axisymmetric reconnection events in JET discharges with extreme shear reversal. *Plasma Phys. Control. Fusion*, 44:1127–1141, 2002.

[44] ITER Physics Basis. Chapter 2: Plasma confinement and transport. *Nuclear Fusion*, 39:2175, 1999.

[45] V. Igochine, S. Günter, M. Maraschek, and ASDEX Upgrade Team. Investigation of complex MHD activity by a combined use of various diagnostics. *Nuclear Fusion*, 43:1801–1812, Dec. 2003.

[46] G. G. Lister. Fafner a fully 3-d neutral beam injection code using mote carlo methods. IPP Report Nr. 4/222, Max-Planck-Institut für Plasmaphysik, January 1985.

Danksagung

Ich möchte allen Kollegen und Freunden danken, die mich in der Zeit meiner Doktorarbeit unterstützt haben.
Insbesondere bedanke ich mich bei Dr. Hobirk für die gute Zusammenarbeit und die wissenschaftliche Betreuung während der letzten Jahre. Er hat sich immer Zeit genommen für Fragen. Dr. Sips möchte ich danken für die Unterstützung und Hilfe bei der Organisation der Doktorarbeit und der Vorbereitung der Entladungen.
Ich bedanke mich bei Prof. Wilhelm und Prof. Kaufmann, die diese Arbeit möglich gemacht haben, für die wissenschaftliche Betreuung und Unterstützung.
Bei Prof. Zohm, Prof. Lackner, Prof. Günter und Dr. Gruber möchte ich mich für die wertvollen Diskussionen und Anregungen bedanken.
Dr. Maraschek hat meine Fragen über MHD und weiterer Physik mit sehr viel Geduld beantwortet, dafür möchte ich ihm danken.
Dr. Patrick McCarthy danke ich für seine Erweiterung von CLISTE zur Berechnung von 'current holes', seinen Bemühungen dies stets noch zu verbessern und die wissenschaftlichen Diskussionen.
Dr. Grigory Pereverzev hat mir eine Einweisung in ASTRA geben und mich bei aufkommenen Fragen unterstützt.
Dr. Erika Strumberger und Dr. Valentin Igochine danke ich für ihre Rechnungen und die interessanten Gespräche.
Meinen Kollegen Anja Mück, Jasmine Schirmer, Eilis Quigley, Jörg Hobirk, Alex Geier, Hans Meister, Thomas Pütterich, Matthias Reich, Roberto Pugno, Marc Maraschek, Marcus Foley, Emanuelle Poli und Isabel Nunes möchte ich danken für alle Unterhaltungen und Unternehmungen innerhalb und außerhalb der Fusion und für alle fruchtbaren Diskussionen.
Jörg Hobirk und Alex Geier danke ich außerdem für die geduldige Hilfe bei Linux.
Dr. Luis Giannone hat sich viel Zeit genommen und die gesamte Arbeit korrekturgelesen.
Außerdem möchte ich noch den Computerspezialisten Reinhard Drube, Karl Behler, Roland Merkel und Annedore Buhler danken, die die Computer am laufen gehalten haben.
Ein große Hilfe war das gesamten ASDEX Upgrade Teams durch die gute Zusammenarbeit und die Bereitschaft, alle Fragen zu beantworten.

Meinen Eltern danke ich ganz besonders, die mir immer hilfreich zur Seite stehen.